ULTRAFAST DYNAMICS OF FOLDED ACOUSTIC PHONONS FROM SEMICONDUCTOR SUPERLATTICES

by

Mariano Trigo

A dissertation submitted in partial fulfillment
of the requirements for the degree of
Doctor of Philosophy
(Applied Physics)
in The University of Michigan
2008

Doctoral Committee:

Roberto D. Merlin, Chairperson
Professor Paul R. Berman
Professor Roy Clarke
Professor David A. Reis
Professor Duncan G. Steel

TABLE OF CONTENTS

LIST OF FIGURES

LIST OF TABLES

CHAPTER I

INTRODUCTION

The interest in the acoustic properties of heterostructures is driven by the pursue of a fundamental understanding of the physical properties of nanostructures, as well as applications in semiconductor devices, where energy transport plays a key role [8]. In particular, in a periodic superlattice, the artificial translational symmetry results in the folding of the bulk acoustic dispersion relation into a smaller Brillouin-zone defined by the superlattice periodicity. This folding of the acoustic branches gives rise to additional optical-phonon-like modes of the superlattice with non-zero frequencies at the center of the Brillouin zone, which can therefore couple to light [9]. The folding of the acoustic branches in periodic media was predicted more than fifty years ago [10]. Periodic superlattices have been extensively studied using spontaneous Raman scattering techniques during the early 1980s [9, 11]. Later, following the development of the mode-locked laser, ultrashort light pulses were exploited extensively to study coherent acoustic phonons in the time domain, leading to the well established technique of picosecond ultrasonics [12, 13]. Time resolved spectroscopy has advantages over frequency-domain spectroscopy; in contrast to spontaneous Raman scattering, pump-probe experiments involve the creation of a *coherent* excitation. This allows for the study of propagation effects, which are important in the understanding of the physics of nanostructures, and also due to the prospect of using coherent phonons for imaging [14]. The coherence of the excitation also opens the possibility of using acoustic phonons as a mean to manipulate

other physical processes. For example, it has been proposed that coherent acoustic phonons can be used to induce the decay of the longitudinal optic phonon in InP [15]. Recently, coherent control of acoustic phonons in bulk materials has been observed using ultrafast X-ray diffraction [16], a technique that is directly sensitive to the atomic arrangement of the crystal.

It is of particular interest to understand the propagation of folded acoustic phonons in superlattices. Moreover, the prospect of using short-wavelength folded phonons for imaging requires understanding the generation process of such high-frequency vibrations. In the case of bulk crystals, there is a well established model of the ultrafast generation of acoustic vibrations developed by Thomsen and coworkers [12]. However, a model that describes the generation of high-frequency folded phonons in heterostructures is still needed. The propagation and generation of folded phonons has been studied optically using conveniently designed samples such as in Ref. [17] where the pump and the probe are absorbed in different regions, or with superconducting bolometers to detect the propagating acoustic phonons after they escape from a superlattice [18]. In addition, independent advancements in laser and synchrotron technology have recently provided us with short X-ray pulses with durations between 100 fs and 100 ps. Since X rays couple strongly to core electrons in the lattice ions, X-ray diffraction is an ideal tool to study lattice dynamics in the time domain, and has been used to probe ultrafast processes in bulk materials [19, 20, 21, 22, 23].

This thesis presents time-resolved studies of folded acoustic phonons in superlattices that intend to provide information on the ultrafast generation and detection processes. The work presented here is based on two pump-probe experiments on semiconductor superlattices. The two experiments are conceptually similar: a strong laser pulse excites acoustic phonons and a delayed probe measures some property of the sample as a function of time. The first experiment uses optical

pulses to measure the reflectivity of the sample, while in the second experiment, a short burst of X rays is used to probe the sample through X-ray diffraction. Because of the coupling of X rays with tightly bound electrons, X-ray diffraction is directly sensitive to the atomic arrangement of the ions in the crystal and renders this technique ideal to study lattice dynamics in condensed matter. Although both experiments are conceptually similar, the field of ultrafast X-ray diffraction is still in a very early stage of development and the experimental challenges abound. We complement the experimental observations with a continuum model of the acoustic vibrations that provides insight on the generation and detection mechanisms of folded acoustic phonons.

This thesis is organized as follows. Chapter II is an introduction to the relevant solid-state physics concepts. I begin with the derivation of the vibrational modes of a linear atomic chain with nearest-neighbors interactions followed by the continuum approximation for long wavelength phonons. Next, I show the folding of the acoustic branches due to the acoustic modulation in a periodic, infinite, one-dimensional superlattice.

Chapter III deals with the mechanism for the generation of the acoustic phonons in a finite superlattice. The strain is assumed to be generated thermo-elastically following the model in Ref. [12]. After excitation, the propagation is governed by a piece-wise constant wave equation for the atomic displacement. I develop a solution of this wave equation in terms of the acoustic normal modes of vibration of the finite structure. The coherent vibration modifies the refractive index in time and, hence, the optical reflectivity of the sample. Using the normal mode expansion, I derive a semi-analytical expression for the spectrum of the change in reflectivity induced by the coherent acoustic phonon. With the aid of the eigenmode expansion of the solution, I show at the end of this chapter, that some of the eigenmodes that are excited by the laser pulse have the peculiar behavior of avoiding the surfaces of

the superlattice. This behavior is shown to be general to any wave in a periodic perturbation.

The technological challenges to produce short pulses of light are discussed in Chapter IV. The first part introduces the basic laser concepts required for the generation of femtosecond laser pulses, and a quick overview of chirped-pulse amplification followed by the nonlinear process of optical parametric amplification. At the end of this section I review briefly the equipment available in our laboratory for low temperature experiments. The time-resolved X-ray diffraction studies in this thesis require a high-brightness source of X-ray radiation only accessible in synchrotron laboratories. In the second part of Chapter IV, I describe the generation of hard X rays from relativistic charged particles and I show typical parameters for the Advanced Photon Source (APS) where the X-ray experiments were performed. The chapter ends with a description of the particular beamline of the APS dedicated to time-resolved studies.

In Chapter V, I present the results of the optical pump-probe experiments on folded acoustic phonons in GaAs/AlAs superlattices. I begin with a discussion of a two-superlattice scheme to study propagating folded phonons. Vibrations of up to 1 THz can be detected after traversing 1 μm of GaAs at 80 K. The experimental observations are compared with the predicted spectrum from the continuum model developed in Chapter III, which helps to identify the features due to the detection and the generation processes. Also in this chapter, I show evidence of the observation of surface avoiding waves that are confined to the superlattice. This evidence is supported by a numerical solution of the wave equation.

Chapter VI begins with an introduction to the X-ray concepts of Bragg's law and the dynamical theory of diffraction by perfect and strained crystals. Next, I show a proposed scheme to measure the wavevector content of the coherent acoustic phonons that reach the substrate using X-ray diffraction, and the challenges posed

by the short lifetime of these high-frequency modes. Finally, I present experimental results that indicate that folded acoustic phonons emitted from a superlattice into a bulk substrate can be observed using time resolved X-ray diffraction. Conclusions and comments are given in Chapter VII.

CHAPTER II

CRYSTAL VIBRATIONS

In this Chapter I present an introduction to the basic solid state physics concepts treated in this thesis. I begin with a simple one-dimensional model of the vibrations of a solid. Next I show the folding of the acoustic dispersion relation due to an artificial periodicity. Finally I mention briefly the quantum-mechanical description of the crystal vibrations.

2.1 Normal modes and lattice vibrations

One of the simplest models of a solid consists of a one-dimensional linear chain of atoms where the interaction is only between nearest neighbors, and the potential energy is given by the harmonic potential

$$V(x, x') = -\frac{K}{2}(x - x')^2. \tag{2.1}$$

This interaction is the first non-zero term in the power series expansion of the total interaction energy between two atoms. Higher order, anharmonic terms are often negligible, although they may become significant when the amplitude of the motion is large. The constant K is the curvature of the potential energy at the equilibrium position.

We consider the case where each unit cell contains two kinds of atoms, with masses M_1 and M_2, attached to springs of constant K, as shown in Fig. 2.1. The period of the crystal is d and we assume for simplicity that the masses are

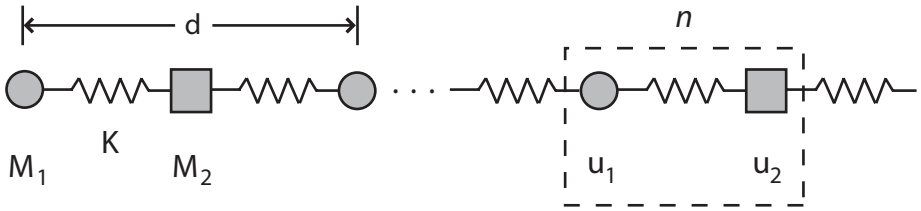

Figure 2.1: A one dimensional model of a crystal.

constrained to move in the direction of the chain (longitudinal vibrations). The equations of motion for the displacement of the two atoms in the n^{th} unit cell are

$$M_1 \ddot{u}_1^n = -K[(u_2^n - u_1^n) - (u_1^n - u_2^{n-1})] \tag{2.2}$$

$$M_2 \ddot{u}_2^n = -K[(u_1^{n+1} - u_2^n) - (u_2^n - u_1^n)] \tag{2.3}$$

where u_j^n is the displacement from equilibrium of atom $j = 1, 2$ in the n-th unit cell. Rearranging the terms, this set of equations reduces to

$$\begin{aligned} M_1 \ddot{u}_1^n &= -K[2u_1^n - u_2^n - u_2^{n-1}] \\ M_2 \ddot{u}_2^n &= -K[2u_2^n - u_1^{n+1} - u_1^n]. \end{aligned} \tag{2.4}$$

To find the eigenmodes we assume a Bloch solution of the form $u_{1,2} = Q_{1,2}(q) \exp[i(\Omega t - qd)]$, where q and Ω are the wavevector and frequency of the corresponding eigenmode. Here, $Q_{1,2}(q)$ is, respectively, the displacement of atom 1 and 2 within the unit cell for the eigenmode of wavevector q. Expressing Eq. (2.4) in matrix form we obtain

$$-\Omega^2 \begin{pmatrix} Q_1 \\ Q_2 \end{pmatrix} = \begin{pmatrix} \frac{2K}{M_1} & -\frac{K}{M_1}(1 + e^{iqd}) \\ -\frac{K}{M_2}(1 + e^{-iqd}) & \frac{2K}{M_2} \end{pmatrix} \begin{pmatrix} Q_1 \\ Q_2 \end{pmatrix}. \tag{2.5}$$

The non-trivial solution of Eq. (2.5) is obtained by requiring the determinant of the eigenvalue matrix to vanish,

$$M_1 M_2 \Omega^4 - 2K(M_1 + M_2)\Omega^2 + 4K^2 \sin(qd/2) = 0. \tag{2.6}$$

The solutions are:

$$\Omega_{\pm}^2(q) = K\frac{M_1+M_2}{M_1M_2} \pm K\left[\left(\frac{M_1+M_2}{M_1M_2}\right)^2 - \frac{4}{M_1M_2}\sin^2\left(\frac{qd}{2}\right)\right]^{1/2}. \qquad (2.7)$$

This is the dispersion relation of the waves in the one-dimensional crystal. The two solutions represent two different branches of the vibrational modes of the chain. A plot of Eq. (2.7) is shown in Fig. 2.2 (a). The upper curve is the Ω_+ solution and is called the *optical* branch because in an ionic material, modes close to $q = 0$ can couple to infrared radiation through the induced oscillating electric dipole [11]. The lower curve is the Ω_- solution and, since the dispersion relation is linear around $q \approx 0$, it is called the *acoustic* branch. Assuming $M_2 > M_1$, the frequencies at $q = \pm\pi/d$ are given by $\Omega_1 = (2K/M_1)^{1/2}$ and $\Omega_2 = (2K/M_2)^{1/2}$. Modes with frequencies between Ω_1 and Ω_2 have a purely imaginary wavevector and therefore do not propagate.

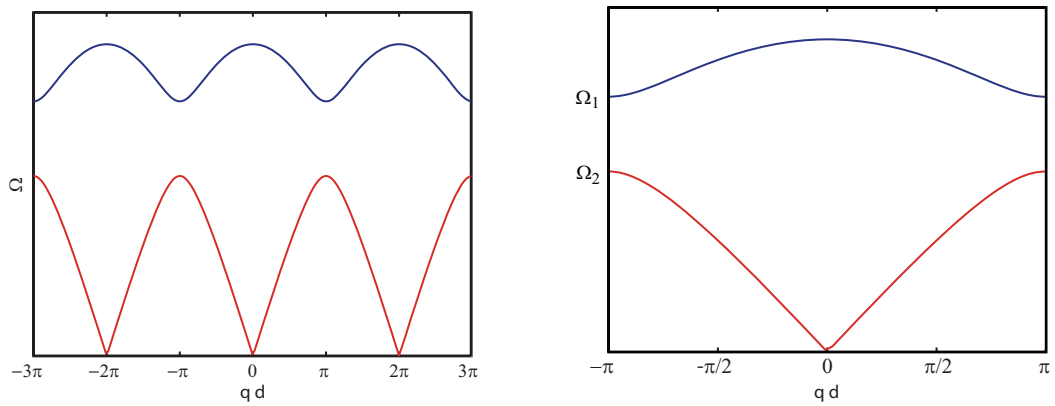

Figure 2.2: Dispersion relation for the linear chain. (a) extended-zone scheme; (b) reduced-zone scheme in which all wavevectors are translated to $-\pi/d < q < \pi/d$, i.e. the first Brillouin zone of the one-dimensional crystal.

A consequence of the translational symmetry of the crystal is that the function $\Omega(q)$ is periodic in q with period $2\pi/d$. This means that all the information of the vibrational modes of the lattice is contained in $-\pi/d < q < \pi/d$, as illustrated in Fig. 2.2 (b). This is the one-dimensional, first Brillouin zone of the linear chain; any

wavevector outside is equivalent to a wavevector inside by a translation of $2\pi/d$. Fig. 2.2 (a) is an extended-scheme representation of the dispersion relation, while Fig. 2.2 (b) is called the reduced-zone scheme. We note that in a finite crystal with N unit cells, the allowed wavevectors are quantized by requiring additional boundary conditions at the ends of the finite chain. There are a total of N normal modes in each branch in the first Brillouin zone.

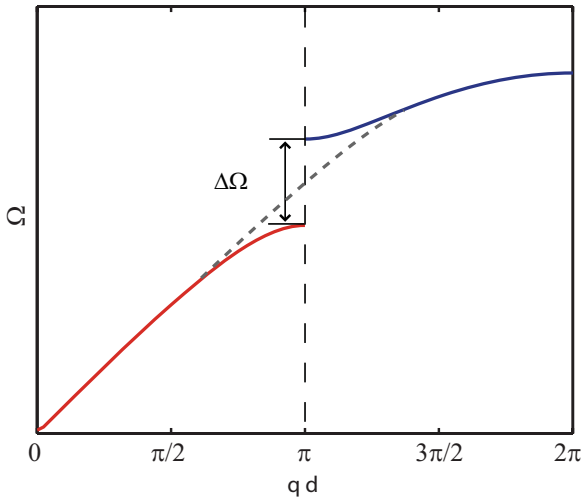

Figure 2.3: The dispersion relation in the extended-zone scheme showing the opening of the gap at the Brillouin zone edge, $q = \pi/d$. The dotted line represents the situation when $M_1 = M_2$.

Consider the limit when $M_1 = M_2$. In this case, since the crystal contains only one type of atom, the size of the unit cell is equal to the nearest-neighbor distance, a, which is half of the size of the unit cell for $M_1 \neq M_2$. Similarly, the first Brillouin zone is twice the size of the Brillouin zone for $M_1 \neq M_2$, since $a = d/2$. In this case, the dispersion relation reduces to a single acoustic branch given by

$$\Omega(q) = 2\sqrt{\frac{K}{M}}\left|\sin\left(\frac{qa}{2}\right)\right|, \tag{2.8}$$

where $M_1 = M_2 = M$ is the mass of the atom.

Figure 2.3 illustrates what happens with the dispersion relation (dotted line) when $M_1 \neq M_2$: (i) the size of the unit cell doubles to $d = 2a$, and the edge of the

first Brillouin zone moves from $2\pi/d$ to π/d (indicated by the vertical dashed line); (*ii*) a gap opens at $q = \pi/d$ that splits the acoustic branch from the optical branch; (*iii*) the optical branch can be folded back inside the range $q < \pi/d$ as we showed in Fig. 2.2 (b).

2.2 Continuum approximation

When considering excitations of wavelengths much longer than the interatomic spacing, i.e., in the limit $q \ll \pi/a$, the crystal can be regarded as a continuous medium with known density, ρ. In such a medium, the long wavelength limit of the atomic displacement at position $\mathbf{r}$ is described by a continuous vector field $\mathbf{u}(\mathbf{r})$. We define the strain tensor in terms of $\mathbf{u}$ as

$$\eta_{ij} = \frac{1}{2}\left(\frac{\partial u_i}{\partial x_j} + \frac{\partial u_j}{\partial x_i}\right) \tag{2.9}$$

where u_i is the i-th Cartesian component of the displacement field. If the interatomic forces are harmonic, the stress (force) is linear with the strain, η_{ij}, i.e.,

$$\sigma_{ij} = \sum_{k\,l} C_{ijkl}\,\eta_{kl}, \tag{2.10}$$

which is the continuum equivalent of Hooke's law that yields the linear forces in Eq. (2.2). The coefficients C_{ijkl} define a 4^{th} rank tensor called the stiffness tensor, which plays the role of the spring constant in the discussion above. In the most general case the tensor C_{ijkl} has only 21 independent non-zero components. In a highly symmetric case, such as a cubic crystal, the number of non-zero elements reduces to only three independent parameters.

The equation that governs the evolution of the atomic displacement given the stress σ_{kl} is [24],

$$\rho\frac{\partial^2 u_i}{\partial t^2} = \frac{\partial \sigma_{ij}}{\partial x_j} + \frac{\partial \sigma_{ik}}{\partial x_k} + \frac{\partial \sigma_{il}}{\partial x_l}. \tag{2.11}$$

Using Eq. (2.10), and assuming a crystal with cubic symmetry, we obtain

$$\rho\frac{\partial^2 u_i}{\partial t^2} = C_{11}\frac{\partial^2 u_i}{\partial x_i^2} + C_{44}\left(\frac{\partial^2 u_i}{\partial x_j^2} + \frac{\partial^2 u_i}{\partial x_k^2}\right) + (C_{12}+C_{44})\left(\frac{\partial^2 u_j}{\partial x_i \partial x_j} + \frac{\partial^2 u_k}{\partial x_i \partial x_k}\right), \quad (2.12)$$

where we have used the contracted notation for the three non-zero elements of the stiffness tensor $C_{11} = C_{xxxx}$, $C_{12} = C_{xxyy}$ and $C_{44} = C_{yzyz}$ [25]. Next we will consider the solution of Eq. (2.12) in a periodic structure.

2.3 Folded acoustic phonons

Here we show how the acoustic phonon branch is modified by artificially introducing an additional (longer) periodicity in the system. This leads to the term "folded acoustic phonons" because the acoustic branch is folded into a smaller first Brillouin zone determined by the artificial period.

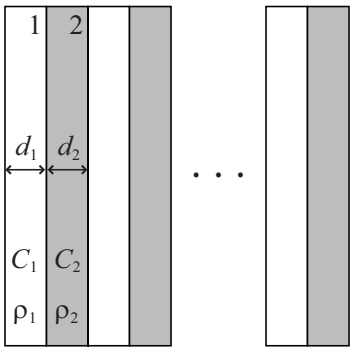

Figure 2.4: A superlattice made of a periodic stack of two materials with alternating acoustic properties.

Consider an infinite, periodic array of two materials with alternating density, ρ_1 and ρ_2, stacked along the $\hat{z}$ direction, as shown in Fig. 2.4. The relevant component of the stiffness tensor is given by $C = C_{11}$ which we labeled C_1 and C_2 for layers 1 and 2 respectively. We are interested in longitudinal waves propagating in the $\hat{z}$ direction, perpendicular to the interfaces. In this geometry, the right hand side of Eq. (2.12) contains only the first term. Moreover, since the material properties are constant in each layer, the motion is described by the piece-wise constant wave

equation,

$$\rho_j \frac{\partial^2 u_j}{\partial t^2} = C_j \frac{\partial^2 u_j}{\partial z^2}, \tag{2.13}$$

where the index $j = 1, 2$ refers to the quantities in layer 1 or 2 respectively. Equation (2.13) is a homogeneous wave equation with constant coefficients. This means that, for a given angular frequency ω, the waves in each layer are combinations of plane waves with wavevectors $\pm q_{1,2} = \pm\omega/v_{1,2}$, where $v_{1,2} = \sqrt{C_{1,2}/\rho_{1,2}}$ is the corresponding speed of sound. The solutions are matched at the boundaries by requiring the continuity of the stress and the displacement [11],

$$C_1 \left.\frac{\partial u_1}{\partial z}\right|_{z_i} = C_2 \left.\frac{\partial u_2}{\partial z}\right|_{z_i}, \tag{2.14}$$

and

$$u_1(z_i) = u_2(z_i). \tag{2.15}$$

Using these two equations together with Bloch's theorem to relates the waves in adjacent unit cells, we find the following dispersion relation

$$\cos(qD) = \cos\left(\frac{\Omega d_1}{v_1}\right)\cos\left(\frac{\Omega d_2}{v_2}\right) - \frac{1}{2}\left(\frac{\rho_2 v_2}{\rho_1 v_1} + \frac{\rho_1 v_1}{\rho_2 v_2}\right)\sin\left(\frac{\Omega d_1}{v_1}\right)\sin\left(\frac{\Omega d_2}{v_2}\right) \tag{2.16}$$

which can be rearranged as

$$\cos(qD) = \cos\left[\Omega\left(\frac{d_1}{v_1} + \frac{d_2}{v_2}\right)\right] - \frac{\epsilon^2}{2}\sin\left(\frac{\Omega d_1}{v_1}\right)\sin\left(\frac{\Omega d_2}{v_2}\right). \tag{2.17}$$

with

$$\epsilon = \frac{|\rho_1 v_1 - \rho_2 v_2|}{(\rho_1 v_1 \rho_2 v_2)^{1/2}}. \tag{2.18}$$

This expression has the same form as the dispersion relation for electrons in a periodic potential in the Kronig-Penney model [25]. A plot of Eq. (2.17) is shown in Fig. 2.5 for a typical superlattice. The red curve is the dispersion relation of the acoustic wave in an effective bulk material given by the average of the two

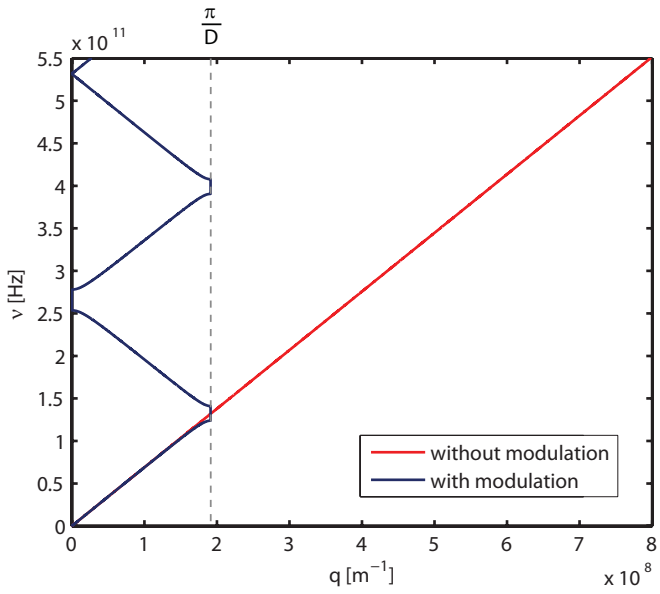

Figure 2.5: Dispersion relation for the acoustic waves showing the folding of the acoustic branches in a superlattice.

components of the superlattice unit cell. This modulation of the acoustic properties gives rise to: (i) a folding of the acoustic branch into the first Brillouin zone of the superlattice, between $-\pi/D$ and π/D and, (ii) the creation of frequency gaps at the center and the edge of the Brillouin zone, as indicated by the blue curve. In the same way as in the Kronig-Penney model for electrons, two degenerate modes exist in the unperturbed dispersion relation at wavevectors multiples of $\pm\pi/D$. The coupling between these modes due to the acoustic modulation removes the degeneracy by opening frequency gaps. This originates from the second term in Eq. (2.17) that contains the modulation parameter ϵ. Exactly at the zone-center or the zone-edge, the two eigenmodes are standing waves and can be labeled by their symmetry, one being odd (A_1) and the other one being even (B_2) with respect to inversion about the middle of each layer. From these two modes, the A_1 mode is Raman active (lowest frequency mode in Fig. 2.5), while the one with even symmetry is forbidden [11].

2.4 Quantized vibrational modes

At the microscopic level, the motion of the atoms in the linear chain considered in Section 2.1 is described by quantum mechanics. The quantization of the vibrational modes of the solid is analogous to the quantization of the electromagnetic field that gives rise to the concept of a photon [26]. In the vibrational case, the motion of the interacting atoms is decoupled by transforming to the normal mode basis, as we did in Section 2.1. From their definition, the normal modes of vibration are independent harmonic oscillators with a well defined frequency and wavevector. When quantum mechanics is taken into account, the energy of each of these harmonic oscillators is quantized in units of $\hbar\Omega$, where $\hbar$ is Plank's constant. The quantum of energy in a normal mode of vibrations is called a *phonon*. In a crystal with two atoms per unit cell, one speaks of *optical* phonons and *acoustic* phonons, corresponding to phonon modes in the optical or the acoustic branch respectively. Also, the phonon can have a combination of transverse (T) and longitudinal (L) polarization with respect to the propagation direction. In a superlattice, the folding of the acoustic branch leads to the term "folded acoustic phonons" for acoustic modes in the higher branches. These are the analog of the optical modes for the artificial structure.

In the following Chapters the term "coherent phonon" is used to refer to the coherent acoustic vibrations generated by the ultrafast laser pulse. In a single harmonic oscillator, a coherent mode, $|\alpha\rangle$, is a superposition of quantum states with different occupation number, such that the evolution of the coordinate expectation value, $\langle\alpha|\hat{x}|\alpha\rangle$, corresponds to the trajectory of the classical harmonic oscillator, $x(t)$. A coherent phonon in the acoustic branch is the quantum-mechanical description of the macroscopic strain discussed above.

CHAPTER III

ULTRAFAST GENERATION OF FOLDED PHONONS IN SUPERLATTICES

In this chapter I introduce a phenomenological model used in the interpretation of the experimental results. First I present a method to solve the wave equation for the acoustic strain based on the expansion in the eigenmode basis. Then I derive a semi-analytical expression for the spectrum of the reflectivity. Finally, I introduce the surface-avoiding eigenmodes.

3.1 Continuum elastic model

The continuum model of the generation of acoustic waves in layered media is based on that of Thomsen et al. [12]. We use a different approach to solve the wave equation in which the solution is expanded in eigenfunctions that correspond to the acoustic eigenmodes [27]. The advantage of this approach is that it gives a description in terms of the frequency components that is more natural for the interpretation of spectroscopic data.

In a layered structure with density $\rho(z)$ and elastic stiffness $C(z)$, the equation of motion for the amplitude of the longitudinal acoustic displacement, $u(z,t)$, propagating in the z direction is [12]

$$\rho(z)\frac{\partial^2 u(z,t)}{\partial t^2} = \frac{\partial \sigma(z,t)}{\partial z}, \tag{3.1}$$

where the only non-zero component of the stress tensor is $\sigma_{zz} = \sigma = C(z)\eta(z,t)$.

Here, $\eta(z,t) = \eta_{zz}(z,t) = \partial u(z,t)/\partial z$ is the relevant component of the strain tensor. Following the treatment in [13], we assume that the absorption of a laser pulse induces a sudden temperature rise, ΔT, along with a thermal stress $\sigma_T = -3B\beta\Delta T(z,t)$ [12], which drives the acoustic strain. This contribution gives the driven wave equation,

$$\rho(z)\frac{\partial^2 u(z,t)}{\partial t^2} = \frac{\partial}{\partial z}\left(C(z)\frac{\partial u(z,t)}{\partial z}\right) + \frac{\partial \sigma_T(z,t)}{\partial z}. \tag{3.2}$$

The temperature rise can be expressed in terms of the electric field of the laser pulse [13]

$$\Delta T = \frac{\alpha(z)n(z)J}{C_P}\left|\frac{E(z,t)}{E_0}\right|^2 \tag{3.3}$$

where C_P is the specific heat, $\alpha(z)$ and $n(z)$ are the position-dependent absorption coefficient and index of refraction, respectively, and J is the total pulse energy. Here, $E(z,t)$ is the electric field at time t and position z from the surface and E_0 is the electric field at the surface. We define a function $K(z)$ such that the stress induced by the laser can be written as

$$\sigma_T = K(z)\left|\frac{E(z,t)}{E_0}\right|^2. \tag{3.4}$$

This induced stress is proportional to the intensity of the laser pulse modulated by the function $K(z)$ that takes into account the absorption in the superlattice.

3.1.1 Eigenmodes

In an infinite superlattice, the solutions of Eq. (3.2) are given by Bloch waves of the form $u_q e^{iqz}$ where q is the wavevector in the reduced Brillouin zone scheme. However, in a finite structure the Bloch waves are not solutions of the equation since the system is not translation-invariant. In this case, Eq (3.2) can be solved by

expanding the solution in terms of eigenfunctions. The general solution is

$$u(z,t) = \sum_n r_n(t) U_n(z) \tag{3.5}$$

where n is the mode label and $r_n(t)$ are the coefficients of the expansion. The functions $U_n(z)$ represent the spatial profile of the eigenmodes and are the solution of the time independent eigenvalue equation

$$-\Omega_n^2 \rho(z) U_n(z) = \frac{\partial}{\partial z}\left(C(z)\frac{\partial U_n(z)}{\partial z}\right). \tag{3.6}$$

where Ω_n is the frequency of the mode. Assuming that all the quantities are constant within each layer and that they only differ between adjacent layers, this equation can be solved using a transfer matrix method to match the boundary conditions (continuity of u and σ) at each interface [28]. The equation for a single layer can be written as

$$-\Omega_n^2 \rho_j U_n(z) = C_j \frac{d^2 U_n(z)}{dz^2} \tag{3.7}$$

where ρ_j and C_j are the density and the elastic stiffness of the material in layer j. The solution of (3.7) is given by the linear combination $A_j \exp(iq_j z) + B_j \exp(-iq_j z)$ with the wavevector defined by $q_j^n = \Omega_n / v_j$, where $v_j = (C_j/\rho_j)^{1/2}$ is the speed of sound in layer j. The variable z is a local coordinate that runs within layer j, i. e. $0 < z < a_j$, where a_j is the thickness of layer j. Figure 3.1 shows a diagram describing all these quantities.

The coefficients A_j and B_j can be related to the ones corresponding to adjacent layers by a transfer matrix such that

$$\begin{bmatrix} A_{j+1} \\ B_{j+1} \end{bmatrix} = \mathbf{M} \begin{bmatrix} A_j \\ B_j \end{bmatrix}, \tag{3.8}$$

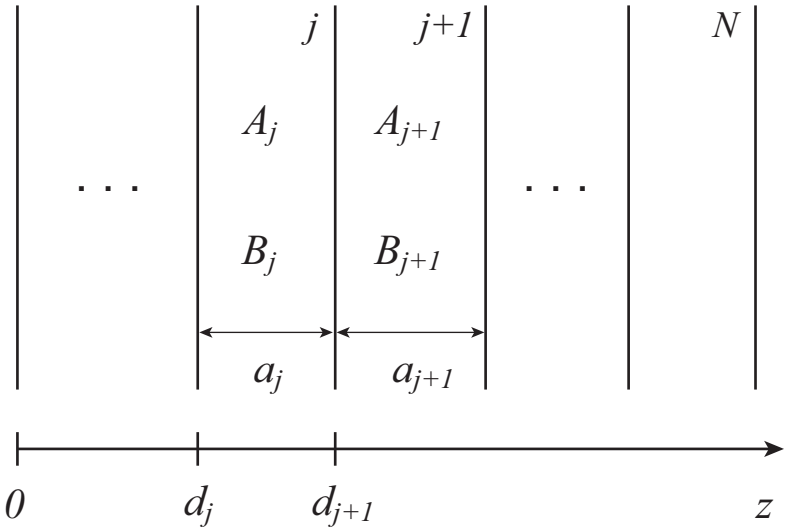

Figure 3.1: Diagram of the one dimensional superlattice. The quantities $A_j$and B_j are the coefficients of the plane waves in each layer, d_j and a_j are the coordinate and the thickness of layer j, respectively.

with the matrix $\mathbf{M}$ given by

$$\mathbf{M} = \begin{bmatrix} (1+Z^{-1})e^{iq_j a_j} & (1-Z^{-1})e^{-iq_j a_j} \\ (1-Z^{-1})e^{iq_j a_j} & (1+Z^{-1})e^{-iq_j a_j} \end{bmatrix}, \tag{3.9}$$

where $Z = v_{j+1}\rho_{j+1}/v_j\rho_j$ is the acoustic impedance of the $j+1 \to j$ interface.

We assume that the boundary can be represented by a free surface, that is $\sigma = C\eta_n = 0$ at $z = 0$ and $z = L$. The first boundary gives for the coefficients of the first layer, $A_1 = B_1$. With this additional condition, the displacement profile of an eigenmode in each layer can be written in the alternative form

$$U_n^j(z) = 2A_n^j \cos(q_n^j z + \phi_n^j). \tag{3.10}$$

Here the amplitudes A_n^j and phases ϕ_n^j are determined from the transfer matrix equation (3.8). After some algebra, the matrix equation relating the amplitudes of the counter-propagating plane waves, Eq (3.8), can be replaced by an algebraic

equation relating the amplitudes and phases in Eq. (3.10),

$$A_{j+1} = A_j \left[\cos^2(q_j a_j + \phi_j) + Z \sin^2(q_j a_j + \phi_j)\right]^{1/2}$$
$$\phi_{j+1} = \arctan(Z \tan(q_j a_j + \phi_j)). \tag{3.11}$$

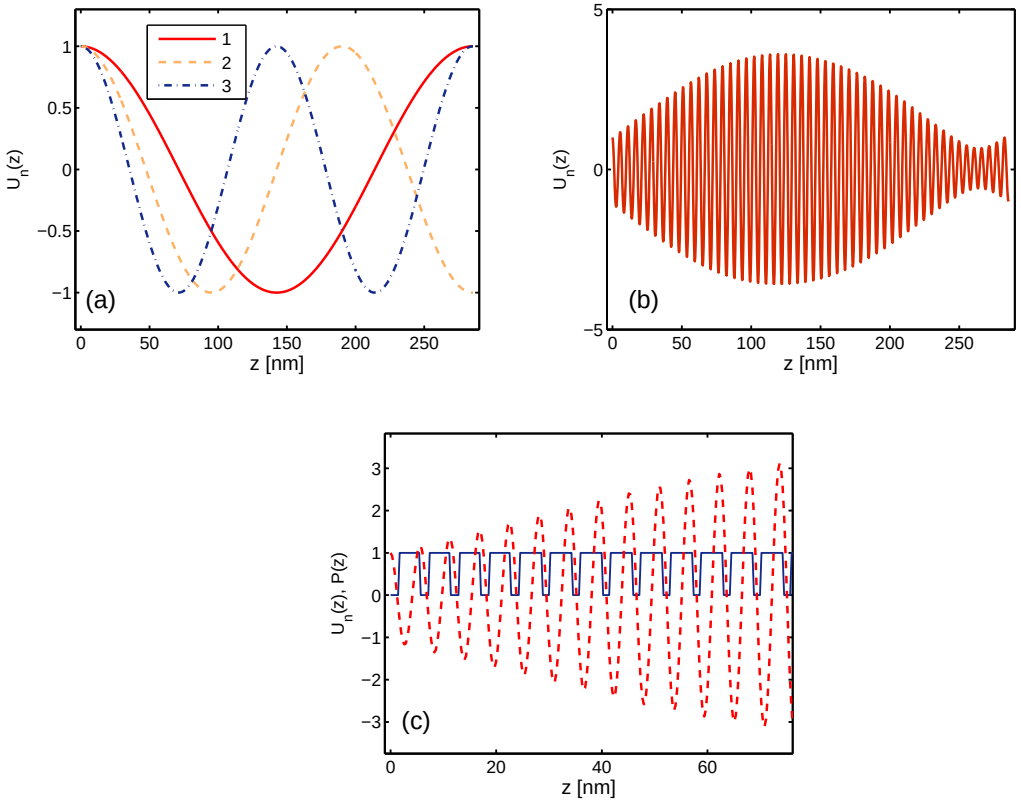

Figure 3.2: Some representative eigenmodes of the finite superlattice. (a) first three modes showing $du/dz = 0$ at the boundaries. (b) a mode near zone center which exhibits a richer behavior, and (c) an expanded view of the same mode (dashed curve) showing that waves near zone center have nearly the same periodicity as the superlattice (represented by the solid square wave).

The discrete eigenfrequencies are obtained from the additional condition $\partial U_n(L,t)/\partial z = 0$. This second boundary condition yields a recursive relation involving all phases ϕ_j for the different layers. In terms of the phase of the last layer ($j = N$), using Eq. (3.10) for $U_n(z)$,

$$\sin\left(\frac{\Omega_n}{v_N} a_N + \phi_N(\Omega_n)\right) = 0. \tag{3.12}$$

Note that ϕ_N depends on the phases of all the previous layers through Eq. (3.11). This condition can be solved numerically, and from Eq. (3.10) and Eq. (3.11), the functions $U_n(z)$ can be determined.

A few representative eigenmodes are shown in Fig. 3.2 for a finite structure with 50 periods of 1.49 nm-thick GaAs, 4.22 nm-thick AlAs layers. In (a), the first three eigenmodes are shown. For low frequency waves, the superlattice behaves as an effective bulk medium with the average speed of sound v, obtained from the relation $D/v = d_{\mathrm{GaAs}}/v_{\mathrm{GaAs}} + d_{\mathrm{AlAs}}/v_{\mathrm{AlAs}}$ [11], where $D = d_{\mathrm{GaAs}} + d_{\mathrm{AlAs}}$ is the period of the superlattice. Near the Brillouin zone center and zone edge, the effect of the periodicity modifies drastically the shape of the mode profile. Figure 3.2 (b) shows an eigenmode near the first zone center acoustic gap. The mode has nearly the same periodicity as the superlattice, as shown in Fig. 3.2 (c). As we will see later, modes with wavelengths comparable to the period of the superlattice have unusual properties in that they avoid the boundaries of the periodic structure.

In the following section, we calculate how the different modes are excited by a short laser pulse.

3.1.2 Generation mechanism

We extend the treatment in Ref. [29] for the generation mechanism. Here we obtain an analytical expression in the limit of short pulses. The time dependent amplitudes satisfy the driven harmonic oscillator equation [29]

$$\frac{d^2 r_n(t)}{dt^2} + \Omega_n^2 r_n(t) = G_n(t), \tag{3.13}$$

where

$$G_n(t) = \int \frac{\partial \sigma_T(z,t)}{\partial z} U_n(z) dz = -\int \frac{\partial U_n(z)}{\partial z} \sigma_T(z,t) dz, \tag{3.14}$$

after integration by parts. Written in this form, the function $G_n(t)$, which drives the equation for the time dependent amplitude $r_n(t)$ (Eq. (3.13)), is given by an overlap

integral between the laser-generated stress $\sigma_T(z,t)$ and the time-independent strain associated with the eigenmode n, i. e. $\eta_n(z) = \partial U_n(z)/\partial z$. The excitation of mode n depends on the temporal behavior of the source term $\sigma_T(z,t)$, as well as its spatial profile.

Consider a gaussian laser pulse $E(z,t) \sim \exp(-t^2/2\tau^2)E(z)$ where $E(z)$ is the spatial profile of the electric field. Under this assumption, the source term σ_T (or equivalently ΔT) can be separated into its spatial and temporal part $\Delta T(z,t) = g(z)h(t)$. Using the definition of the function $K(z)$ we can write

$$g(z) = \frac{-3B\beta}{C}\alpha(z)n(z)J\left|\frac{E(z)}{E_0}\right|^2 = K(z)\left|\frac{E(z)}{E_0}\right|^2 \tag{3.15}$$

for the spatial dependence and

$$h(t) = \frac{1}{2}\left[1 + \mathrm{erf}\left(\frac{t}{\tau}\right)\right]. \tag{3.16}$$

for the temporal part. Since the laser pulse is much shorter than the phonon period, we take $\tau \to 0$ and the function $h(t)$ simplifies to a Heaviside step function. In this limit, the excitation is turned on suddenly at $t = 0$ and remains on indefinitely because we assumed that there is no thermal diffusion. We therefore assume that G_n is time independent.

We now discuss the dependence of G_n on the shape of the electric field of the laser pulse. Using the definition of $g(z)$, Eq. (3.14) becomes

$$G_n = \int g(z)\frac{\partial U_n(z)}{\partial z}dz$$

or

$$G_n = \int K(z)\left|\frac{E(z)}{E_0}\right|^2 \frac{\partial U_n(z)}{\partial z}dz. \tag{3.17}$$

Equation (3.17) is an overlap integral between the strain associated with mode n and the intensity of the laser pulse $|E(z)|^2$, weighted by the function $K(z)$. Recall that the function $K(z)$ is a square wave that accounts for the different absorption

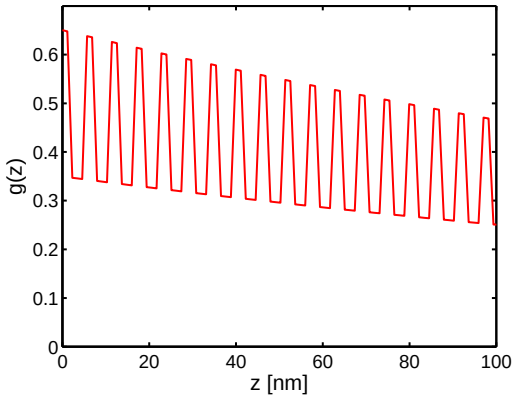

Figure 3.3: The function $g(z)$ that enters Eq. (3.17). The shape of $g(z)$ determines which modes of the superlattice are excited by the laser pulse.

of the laser in the layers of the superlattice. It is a periodic function of z with the periodicity of the superlattice. Consequently, the modes that contribute the most to this integral are those with the same periodicity as the superlattice. In the frequency domain, the solution of Eq. (3.13) is given by

$$\tilde{r}_n(\omega) = \frac{G_n}{\Omega_n^2 - \omega^2} \simeq \frac{G_n}{2\Omega_n}\delta(\omega - \Omega_n) \tag{3.18}$$

which can be approximated by

$$\tilde{r}_n(\omega) \simeq \tilde{r}_n(\Omega_n) = \frac{G_n}{2\Omega_n} \tag{3.19}$$

At this point it is necessary to assume a particular shape for $E(z)$. Consider a laser pulse incident from $z = -\infty$ with the electric field given by $E(z) = E_0 \exp(ikz)$. If we take absorption into account by allowing an imaginary part to the wavevector k, the intensity of the laser decays into the superlattice and the integral in Eq. (3.17) becomes

$$G_n = \int e^{-\alpha z} K(z) \frac{\partial U_n(z)}{\partial z} dz. \tag{3.20}$$

where $\alpha/2 = \mathrm{Im}\{k\}$ is the absorption coefficient of the light in the superlattice at the given laser wavelength. The integrand of Eq. (3.20) is shown in Fig. 3.3. It

consists of a square wave with the periodicity of the structure, which reflects the fact that the laser pulse is absorbed differently in different layers, modulated by a slowly decaying exponential due to the depletion of the laser. The absorption length of the laser in the superlattice, $\xi = \alpha^{-1}$, determines the spatial extension of the generated strain and as we will see in the optical results, the spatial extension of the detection region. From these considerations, we can adjust the exponential decay to obtain the best estimate for α.

Figure 3.4 shows $G_n = \Omega_n r_n(\Omega_n)$, plotted against the mode frequency $\Omega_n/2\pi$, calculated for a superlattice with 200 periods (solid line, top panel). The dashed line is a plot of the function f_n which corresponds to the sensitivity in the detection as will be discussed below. We also show the dispersion relation for an infinite structure (bottom panel) calculated using the model for infinite structures introduced in the previous chapter [10]. The laser absorption length was fixed at $\alpha^{-1} = 300$ nm. A few points are worth noticing: (i), the minigaps are clearly visible at ~ 0.5 THz for the first zone-edge and at ~ 1 THz for the first zone-center; (ii) the intensity of G_n is somewhat constant outside of the minigaps, meaning that $r_n(\Omega_n)$ has an overall decay of the form $1/\Omega_n$; and (iii) the zone-center acoustic gap has a strong peak on the higher side of the gap which corresponds to the Raman active mode at the zone center.

The layer thicknesses of this particular structure are very small. It is unlikely that the different constituents behave as the corresponding bulk materials. In particular, the amount of absorption in each layer is unknown. For this reason, in what follows, we adjust $K_{\mathrm{GaAs}}/K_{\mathrm{AlAs}}$ to get the best match with the experimental spectrum.

3.1.3 Detection mechanism

As the acoustic strain propagates inside the sample, it modifies the dielectric function due to the acousto-optic effect. The perturbation produces a time dependent index

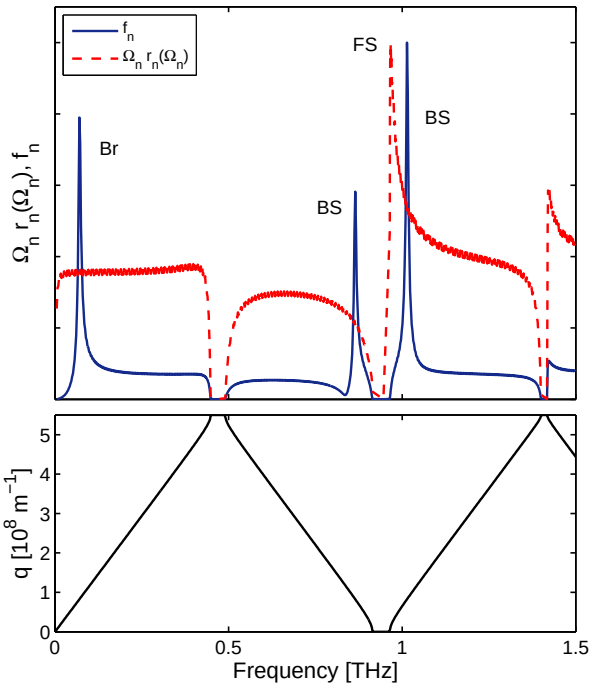

Figure 3.4: (top panel) The dashed curve is a plot of G_n as a function of the mode frequency $\Omega_n/2\pi$ for an infinite superlattice for a laser absorption length of 300 nm and a ratio $K_{\mathrm{GaAs}}/K_{\mathrm{AlAs}} = 1.2$. The dashed line is the coefficient f_n defined in the detection. (bottom panel) dispersion relation for an infinite structure with the same layer thicknesses.

of refraction that affects the complex reflection coefficient, r. The effect of the acoustic phonon in the reflection coefficient Δr can be probed by measuring the differential reflectivity of the sample $\Delta R/R = 2\mathrm{Re}\{\Delta r/r\}$. We calculate next the change in the reflectivity due to the presence of the strain wave. We will derive an analytical expression for the reflectivity spectrum in terms of the quantities defined above such as G_n and the eigenfrequencies, Ω_n.

Consider a probe pulse with spatial profile $E(z) \sim \exp(ik_p z)$ that is sufficiently short to be regarded as a delta function of time. The strain modulates the dielectric function $\Delta\epsilon(z,t)$ causing a change in the reflectivity [12],

$$\Delta R \propto \int_0^\infty \eta(z,t) P(z) \exp(2ik_p z) dz. \tag{3.21}$$

where $P(z)$ is the photoelastic coefficient. The sensitivity function $f(z) =$

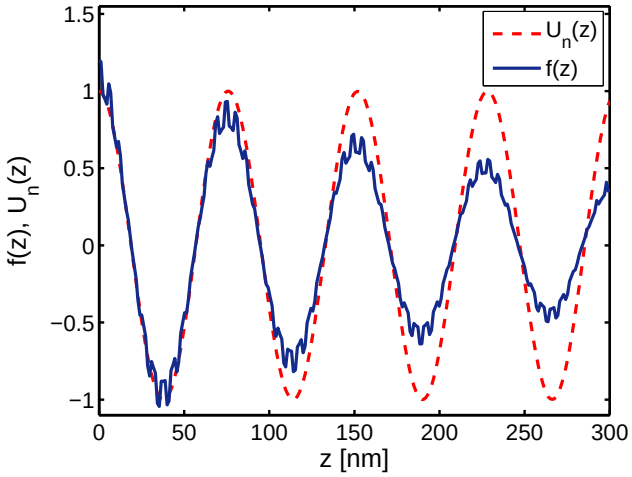

Figure 3.5: (solid line) The sensitivity function for a typical superlattice at a wavelength of $\lambda = 530$ nm with an absorption coefficient of 300 nm. (dashed line) eigenmode with the same wavelength as the sensitivity function.

$P(z)\exp(2ikz)$ determines the coupling between the strain $\eta(z,t)$ and the probe pulse. Fig. 3.5 shows a plot of $f(z)$ for the same structure as in Fig 3.4 and a probe with $\lambda = 530$ nm assuming an absorption length of 300 nm. The function $f(z)$ is the product of a periodic function, $P(z)$, modulated by a complex exponential $e^{2ik_p z}$ that represents the probe reflecting from a distance z from the surface. For a given laser wavelength, $f(z)$ phase-matches with certain eigenmodes, giving a strong contribution to $\Delta R/R$. This situation is illustrated by the dashed curve in Fig. 3.5.

A final note about Eq. (3.21) is worth mentioning. Expressing the change in the reflection coefficient, $r = \rho e^{i\phi}$, as $\Delta r = (\rho + \delta\rho)e^{i(\phi+\delta\phi)}$, where $\delta\rho$ and $\delta\phi$ are the (real-valued) change in the modulus and the phase due to the phonon, the expression for $\Delta r/r$ becomes

$$\frac{\Delta r}{r} = \frac{\delta\rho}{\rho} + i\delta\phi, \tag{3.22}$$

and, since $\Delta R/R = 2\delta\rho/\rho$, Eq. (3.21) only refers to the change in the modulus of the reflection coefficient. In order to measure the imaginary part of $\Delta r/r$, an interferometric scheme that is sensitive to the change in the phase $\delta\phi$ is needed, such as in Ref. [30].

Using expression (3.5) for the expansion of $u(z,t)$ (or, equivalently, $\eta(z,t)$) in the eigenmodes basis, the change in reflectivity from Eq. (3.21) can be recast into the simpler form

$$\Delta R(t) = \sum_n f_n r_n(t) \tag{3.23}$$

where $r_n(t)$ was defined above and

$$f_n = \int_0^\infty \eta_n(z) f(z) dz, \tag{3.24}$$

where $f(z)$ is the sensitivity function. In the frequency domain this expression takes the simple form [29]

$$\Delta\tilde{R}(\omega) \simeq \Delta\tilde{R}(\Omega_n) = \frac{f_n G_n}{2\Omega_n} \tag{3.25}$$

In order to gain some insight, we consider the simplified situation of a semi-infinite superlattice. Equations (3.20) and (3.24) have the same overlap form. Both integrands contain a periodic (square wave) function modulated by a slowly varying envelope. In the first case, the envelope is a decaying exponential due to the absorption of the laser pulse while, for the sensitivity function $f(z)$, the slowly varying envelope is an exponentially decaying sinusoidal. In a semi-infinite superlattice the eigenmode $U_n(z)$ can be expressed in terms of Bloch-waves, by a suitable combination of $u_q e^{iqz}$ and $u_{-q} e^{-iqz}$ that satisfies the boundary condition, where $u_q(z)$ is a periodic function of z. In addition, we can decompose the square wave $P(z)$ in Eq. (3.21) using its Fourier series $P(z) = \sum_m S_m e^{iK_m z}$ where $K_m = 2\pi m/D$ are the reciprocal lattice vectors of the one-dimensional structure with period D. In terms of these Bloch waves, the integral (3.24) is

$$f_q = \int_0^{+\infty} \sum_{m=-\infty}^{+\infty} S_m e^{iK_m z} e^{2ik_p z} \left[A_+ u_{+q} e^{iqz} + A_- u_{-q} e^{-iqz} \right] \tag{3.26}$$

where the eigenmode label n in Eq. (3.24) has been replaced by the (continuous) wavevector in the reduced-zone scheme, q. The factor $e^{2ik_p z}$ in this expression

originates from the electric field of the probe in Eq. (3.24). Alternatively, by making $k_p = i\alpha/2$ we obtain the corresponding result for (3.20). After some algebra, we obtain

$$f_q = \sum_{m=-\infty}^{+\infty} S_m \int_0^{+\infty} \left[e^{i(2k+K_m+q)z} A_+ u_{+q} + e^{i(2k+K_m-q)z} A_- u_{-q} \right]. \tag{3.27}$$

Equation (3.27) has strong components at $q = \pm(2k + K_m)$ which reflect the wavevector conservation for the semi-infinite structure. This conservation rule has been observed nearly twenty years ago in Raman scattering experiments [9]. The strongest contribution to Eq. (3.27) comes from modes near the zone-center with reduced wavevector in the first Brillouin zone given by $q = 2k_p$.

In the finite case, instead of Bloch-like solutions we need to use the eigenmodes obtained in the previous section. We rewrite Eq. (3.24) as a sum over the layer index j. Using Eq. (3.10), which gives the displacement for mode n in each layer, in terms of the amplitudes A_j and phases ϕ_j,

$$f(\Omega_n) = \sum_j \int_{d_j}^{d_{j+1}} P_j e^{2ikz} A_j q_n^{(j)} \sin[q_n^{(j)}(z - d_j) + \phi_n^{(j)}] dz. \tag{3.28}$$

where d_j is the coordinate of the $(j-1) \rightarrow j$ interface. After a simple integration the sum becomes

$$f_n = \sum_j \frac{P_j q_n^{(j)} A_j}{2} \Big[\frac{e^{i(\phi_j - q_n^{(j)})d_{j-1}}}{2k + q_n^j} \left(e^{i(2k+q_n^{(j)})d_j} - e^{i(2k+q_n^{(j)})d_{j-1}} \right) \tag{3.29}$$

$$- \frac{e^{-i(\phi_j - q_n^{(j)})d_{j-1}}}{2k - q_n^j} \left(e^{i(2k-q_n^{(j)})d_j} - e^{i(2k-q_n^{(j)})d_{j-1}} \right) \Big]. \tag{3.30}$$

Notice the denominators with $2k \pm q_n^j$. This is again related to the conservation of the wavevector that gives rise to the Raman doublet at $q = \pm(2k + K_m)$. As we anticipated in Fig. 3.5, the phase-matching between $f(z)$ and the eigenmodes $U_n(z)$ gives rise to the strongest contribution to ΔR. In fact, as we can see from Fig. 3.4, the coefficients f_n exhibit a series of peaks that correspond to those modes of the

finite structure that satisfy $q = \pm 2k_p$.

3.2 Surface-Avoiding Modes

In this section we introduce the surface-avoiding eigenmodes. First we show that the finite size calculations predict modes near the zone-center and the zone-edge that have small amplitudes near the boundaries of the superlattice. Finally we solve the eigenmode equation near the zone-center for a semi-infinite superlattice where the surface-avoidance is exposed more clearly.

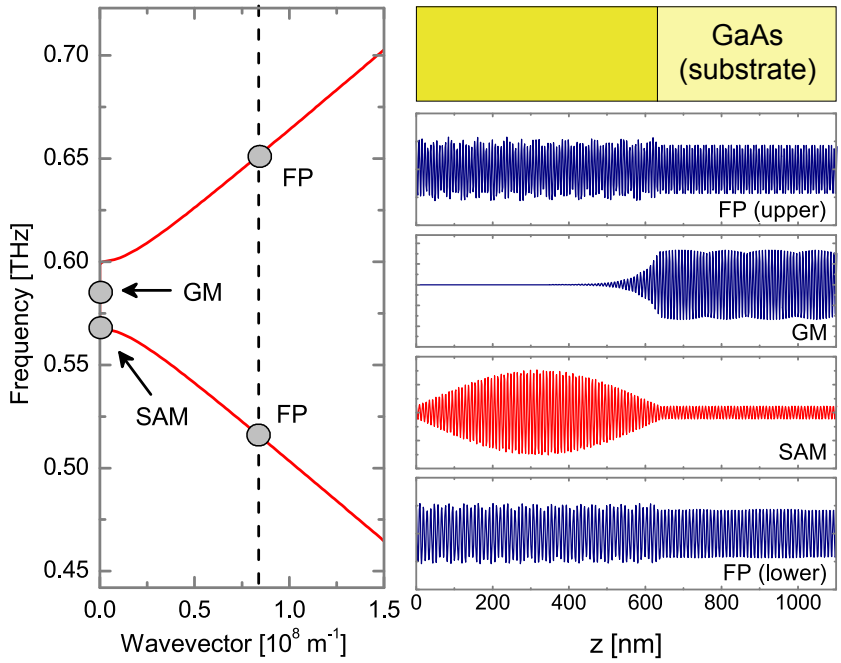

Figure 3.6: Calculated displacement for the LA eigenmodes in the superlattice. SAM is the surface-avoiding mode nearest to $q = 0$, FP are the folded phonons at $q = q_{\mathrm{BS}}$ which apart from a weak modulation in the amplitude are plane waves, and GM is a gap mode that is reflected away from the superlattice.

The displacement pattern for the eigenmodes $u(z)$ for a given finite structure is obtained by the method described in the previous section. A few representative eigenvectors for the acoustic modes of a structure composed of 75 periods of $d_{\mathrm{GaAs}} = 59$ Å and $d_{\mathrm{AlAs}} = 23.5$ Å are shown in Fig. 3.6. Three main features stand out in this figure. First, two modes at wavevector $q_{\mathrm{BS}} = 2k_p$, which correspond to the

usual folded phonons (FP) observed in Raman measurements in the back-scattering geometry [31]. The modes at q_{BS} are sufficiently far away from the gaps that the modulation of the acoustic properties in the superlattice can be neglected. In other words, the dispersion relation is approximately linear at this wavevector. For this reason, these modes are well approximated by plane waves in an effective bulk material [11]. Second, a gap mode (GM) which is a substrate mode that decays into the superlattice. This mode is only observable when the probe is incident from the substrate side or when the superlattice is short enough to allow the probe incident from the left to reach the substrate. In our case, the overlap integral (Eq (3.24)) of this eigenmode with the probe is negligible and therefore not observable. Finally, a mode near $q = 0$ whose amplitude, as expected, diminishes towards the superlattice-vacuum and superlattice-substrate interfaces.

It is instructive to solve the eigenmodes for a semi-infinite superlattice. We start by solving Eq. (3.2) on an infinite periodic structure. The modulation of the acoustic properties originates mainly in the modulation of the density $\rho(z)$. Since the elastic stiffness components C_{GaAs} and C_{AlAs} of the constituents are very similar, we can use an average coefficient $C(z) = \tilde{C} = (d_{\mathrm{GaAs}}C_{\mathrm{GaAs}} + d_{\mathrm{AlAs}}C_{\mathrm{AlAs}})/D$, where D is the period of the structure. In a periodic structure, Bloch theorem dictates that the solutions can be written in the form $u = U_{q,s}(z)e^{i(qz-\Omega t)}$. In this case Eq. (3.2) becomes [32]

$$\frac{\partial^2 U_{q,s}}{\partial z^2} + 2iq\frac{U_{\partial q,s}}{\partial z} + \left[\frac{\rho(z)\Omega_s^2}{\tilde{C}_{11}} - q^2\right] U_{q,s} = 0 \tag{3.31}$$

where the functions $U_{q,s}$ are periodic. Near the zone center, where $q << \pi/D$, we can approximate $U_{q,s} \approx U_s^{(0)} + qDU_s^{(1)}$ and $\Omega_s(q) \approx \Omega_s(0)$. Assuming the normalization $\int \rho U_{0,s}^* U_{0,r} dz = \delta_{s,r}$, we can get the functions $U^{(1)}$ using perturbation theory,

$$U_s^{(0)} = U_{0,s}, \tag{3.32}$$

and

$$U_s^{(1)} = \frac{2i\tilde{C}_{11}}{D} \sum_r \frac{\int U_{0,r}^* (\partial U_{0,s}/\partial z) dz}{\Omega_{0,s}^2 - \Omega_{0,r}^2} U_{0,r}. \tag{3.33}$$

Since the presence of a surface breaks the translational symmetry, we expect this solution to be modified by the boundary condition. In what follows we assume that the solution satisfies a general condition $u + \beta \partial u/\partial z = 0$ at the surface. It is instructive to discuss first the physical situations represented by this expression. Consider a single interface between two materials at $z = 0$. We write the solution of the scattering problem as $u \sim e^{ikz} + re^{-ikz}$, which holds in the half-plane $z > 0$. Assuming the boundary condition $u + \beta \partial u/\partial z = 0$ at $z = 0$, we find

$$\beta = \frac{i}{q} \frac{1+r}{1-r} = i \left[\frac{1 + R + 2\mathrm{Re}(r)}{q(1-R)} \right]$$

where $R = |r|^2$ is the acoustic reflectivity of the interface and q is the phonon wavevector inside the material. Furthermore, we can relate β with the wavevector of the acoustic wave *outside*, $\beta = i/q_{\mathrm{out}}$. This expression shows clearly that the boundary condition covers all the situations from free ($\beta \to \infty$) to clamped ($\beta = 0$) displacement when $\mathrm{Im}(\beta) = 0$, which correspond to non-propagating waves in the half plane $z < 0$. In addition, also the scattering problem corresponding to $\mathrm{Re}(\beta) = 0$ when the wave is incident from the *right* side. Next, we find solutions for the surface-avoiding waves of a semi-infinite superlattice.

The air-superlattice boundary has the effect of mixing the two Bloch waves at $+q$ and $-q$, with solutions given by $u = A_+ U_{+q} e^{iqz} + A_- U_{-q} e^{-iqz}$. To lowest order in ql, the solution is

$$u(z) \approx -iU^{(z)} \left[U^{(0)}(0) + \beta \dot{U}^{(0)}(0) \right] \sin qz + \tag{3.34}$$
$$qD \left\{ \begin{array}{c} U^{(0)}(z) \left[i\frac{\beta}{D} U^{(0)}(0) + U^{(1)}(0) + \beta \dot{U}^{(1)}(0) \right] \\ -U^{(1)}(z) \left[U^{(0)}(0) + \beta \dot{U}^{(0)}(0) \right] \end{array} \right\} \cos qz.$$

where $U^{(0)}$ and $U^{(1)}$ are the perturbative solutions found above. This expression

describes a *surface-avoiding* mode. It involves the product of rapidly $(U^{(0)}, U^{(1)})$ and slowly $(\sin qz, \cos qz)$ varying functions giving rise to beats which originate in the interference between waves with wavevectors $+q$ and $-q$. Comparing the amplitudes at the surface $z = 0$ and $z = \pi/2q$ we see that $u(0)/u(\pi/2q) \propto qD \ll 1$ which clearly states the surface-avoiding character of the solution. As we approach $q = 0$ the avoidance of the surface increases. The solution at exactly $q = 0$ shows the surface avoidance more evidently. As discussed earlier, one of the two solutions for $q = 0$ is $u = U^{(0)}$, now the linearly independent solution of Eq. (3.31) is given by $u = U^{(1)} + iz/DU^{(0)}$ which is physically unacceptable in a semi-infinite structure. One might be tempted to ascribe the surface avoidance to the fact that the modes at $q = 0$ are standing waves. However, in a finite structure, all the eigenmodes are standing waves, but only those with frequencies near the gap avoid the surface.

CHAPTER IV

EXPERIMENTAL TECHNIQUES

Time resolved spectroscopy is a widely used technique in condensed matter physics, which consists of the study of the time evolution of a system after it is perturbed out of equilibrium. The availability of ultra-short laser pulses of the order of a few femtoseconds (10^{-15} s) played a key role in the development of time-resolved techniques. A common time-resolved method in solid state physics is optical pump-probe. Here, short optical pulses from a laser are used to excite the sample and the excited state is monitored by measuring some parameter as, for example, the reflectivity of a delayed probe pulse. The probing part of these experiments is analogous to high speed strobe photography: a very fast stroboscopic light illuminates the object and in this way, very fast events are "frozen" in time in each successive frame. For this reason, the probe pulses must be shorter than the fastest event to be recorded.

In this Chapter, I present some of the techniques available for the study of excitations in solids. In the first section, I introduce the experiments in which ultrafast laser pulses are used to excite and detect acoustic excitations in semiconductor heterostructures. First, I review the equipment and laser systems available in our laboratory, followed by a description of the experimental geometry. In the second part, I describe the synchrotron-based X-ray diffraction experiments where the crystal lattice is probed by a short burst of X rays. I first describe briefly the generation of synchrotron radiation from relativistic charged particles and then I

present the technical aspects of the experiments.

4.1 Optical experiments

All the optical experiments presented in this thesis were performed with pulsed lasers based on titanium-doped sapphire (ti:sapphire). In the pump-probe measurements, we used pulses from an oscillator or amplified pulses from a regenerative amplifier (Coherent Rega). The infra-red amplified pulses can be used directly or can be converted to the visible part of the spectrum by using an Optical Parametric Amplifier (OPA). I will describe each piece of equipment in detail in the following subsections.

4.1.1 Ti:Sapphire oscillator

We used a passively mode-locked Kerr-lens Ti:Sapphire oscillator shown schematically in Fig. 4.1. The laser consists of a Ti:Sapphire crystal, the active medium, embedded in a Fabry-Pérot cavity that supports many electromagnetic modes. Population inversion is achieved by pumping the crystal with a continuous wave (c.w.) laser at 532 nm, which is near the peak of the absorption of Ti:Sapphire. The broadband emission from the Ti:Sapphire, of the order of 130 THz centered at 375 THz (800 nm), excites many ($\sim 10^5$) electromagnetic modes inside the cavity, which oscillate with random relative phases. However, if all the phases are fixed, the superposition of all the modes gives destructive interference except when all the modes are in phase. This leads to a train of short pulses that repeats every $\tau = \Delta\nu^{-1} = 2L/c$, the round trip inside the cavity, here L is the cavity length and c is the speed of light. The repetition frequency of the laser is also equal to the separation between longitudinal modes in the laser cavity, $\Delta\nu$ [33]. A laser with a cavity $L = 1.5$ m has a repetition rate of 100 MHz.

There are different ways to achieve phase-locking of the modes in the cavity.

The most common approach is the Kerr-lens mode-locking (KLM). Self-focusing induced by the non-linear Kerr effect in the Ti:Sapphire crystal makes the pulsed (high-intensity) regime have smaller beam waists than the c.w. regime. In this way, by placing a slit in the laser cavity that cuts the lower intensity parts of the gaussian beam, pulsed operation is favored over continuous-wave. This alone does not guarantee mode-locking. It is also necessary to compensate properly the group velocity dispersion of the different modes inside the cavity. A pair of prisms inside the cavity is the most common solution to obtain a total zero group dispersion [1].

The Ti:Sapphire oscillator outputs $\sim$ 120 fs pulses with an energy of 5 nJ at a rate of 76 MHz. The wavelength can be tuned between 740 and 1070 nm by adjusting a birefringent plate inside the laser cavity. When seeding the amplifier, the wavelength is fixed at 800 nm which is at the peak of the emission from the Ti:Sapphire crystal and the optimum wavelength for amplification. The pulse duration output of the Rega amplifier is strongly dependent on the characteristics of the seed pulses. It is necessary to maximize the bandwidth by adjusting the compensating prisms inside the oscillator. A minimum bandwidth of 10 nm is required for optimum operation of the Rega.

4.1.2 Regenerative amplifier

Pulses from the oscillator are amplified using the Chirped Pulse Amplification (CPA) scheme [34]. The high peak intensity of the pulses from the oscillator can result in crystal damage in the amplifier. Thus, the oscillator pulses have to be stretched by a factor of 10^4 before entering the amplification stage. A pair of gratings arranged for positive dispersion provides the necessary dispersion to achieve $\sim$ 40 ps pulses [35]. Following the stretcher, the pulses are sent into the amplifier cavity where, after many round trips, will emerge amplified by a factor of a thousand.

A diagram of the regenerative amplifier showing the main elements is presented

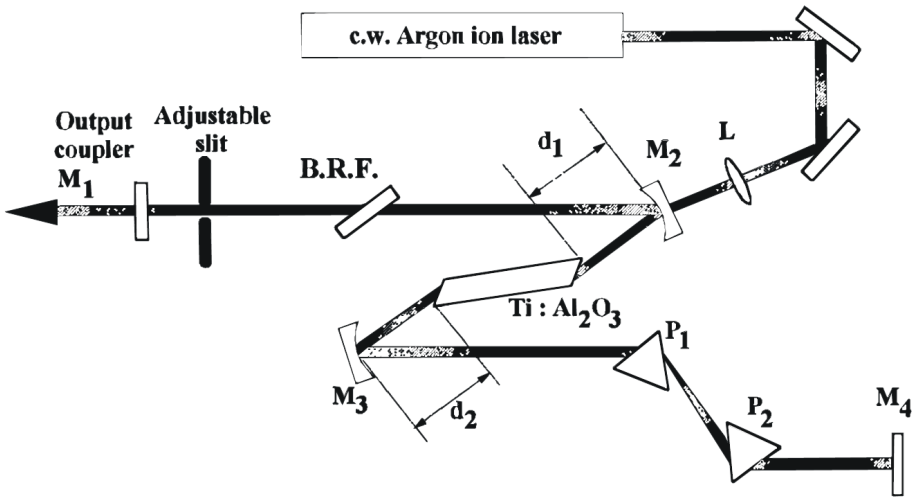

Figure 4.1: Diagram of a Kerr-lens mode-locked Ti:Sapphire oscillator. L is the pump focusing lens, $M_1 - M_2$: curved mirrors, M_4: high-reflector, B.R.F.: birefringent plate, $P_1 - P_2$ intra-cavity prisms. From [1].

in Fig. 4.2. The seed pulses from the Mira oscillator go through a Faraday isolator which exploits the Faraday rotation of the polarization inside an optically active material to rotate the polarization of the back-reflected beam which are blocked by the polarizing cube, CP. The input beam from the oscillator is focused by two curved mirrors on the cavity dumper. From the 76 MHz pulse train, individual pulses are injected into the amplifier cavity, ensuring that only one pulse from the seed beam circulates inside the cavity. The cavity dumper consists of a TeO_2 acousto-optic modulator (AOM) located at the beam waist of the two curved mirrors, oriented at the Brewster angle with respect to the input beam to minimize reflection losses. The AOM can rapidly switch the laser pulses in and out of the cavity by diffracting the light due to the acousto-optic or photoelastic effect [2]. A high frequency acoustic wave is emitted by an RF source into the TeO_2 crystal which modulates the refractive index of the material causing the light to be diffracted at a specific angle. The AOM is driven by two short RF pulses which generate the traveling acoustic waves inside the TeO_2 crystal for the injection and the ejection of the laser pulses To

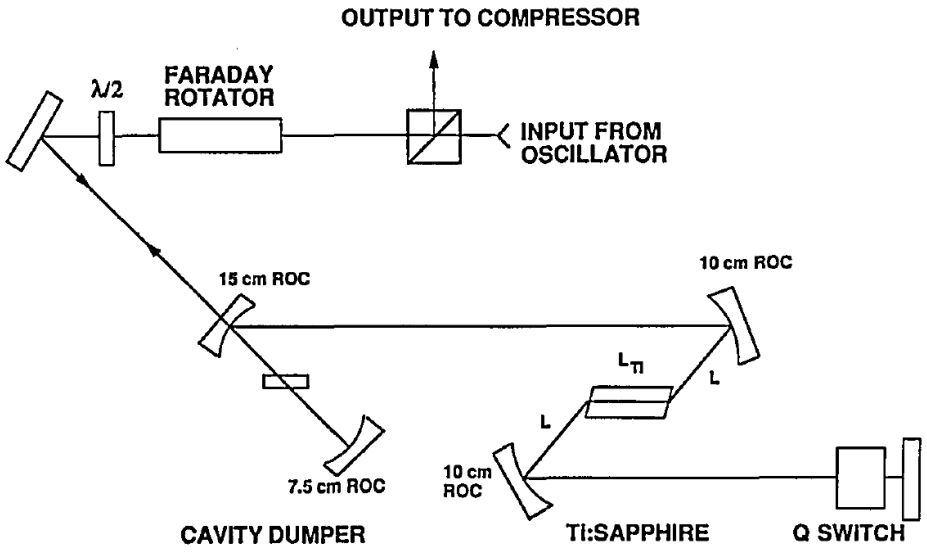

Figure 4.2: Schematic diagram of the regenerative amplifier (From [2]).

maximize the energy extraction from the population inversion in the Ti:Sapphire, the spontaneous emission from the crystal is reduced by a second AOM, the Q-switch, which introduces losses in the cavity until a seed pulse is injected.

The pulses are ejected by the cavity dumper after $20 - 30$ round trips. At the output we get an average power of 1.5 W, with pulses centered at 800 nm with an energy of ~ 6 μJ per pulse.

Finally, the output pulses are recompressed to a duration of 50 fs with a grating compressor [34] (Fig. 4.3). By tuning the separation between the gratings, a positively chirped pulse with longer (redder) wavelengths in the front edge of the pulse, λ_1, and shorter (bluer) wavelengths in the trailing edge, λ_2, is compressed after passing through the double grating compressor.

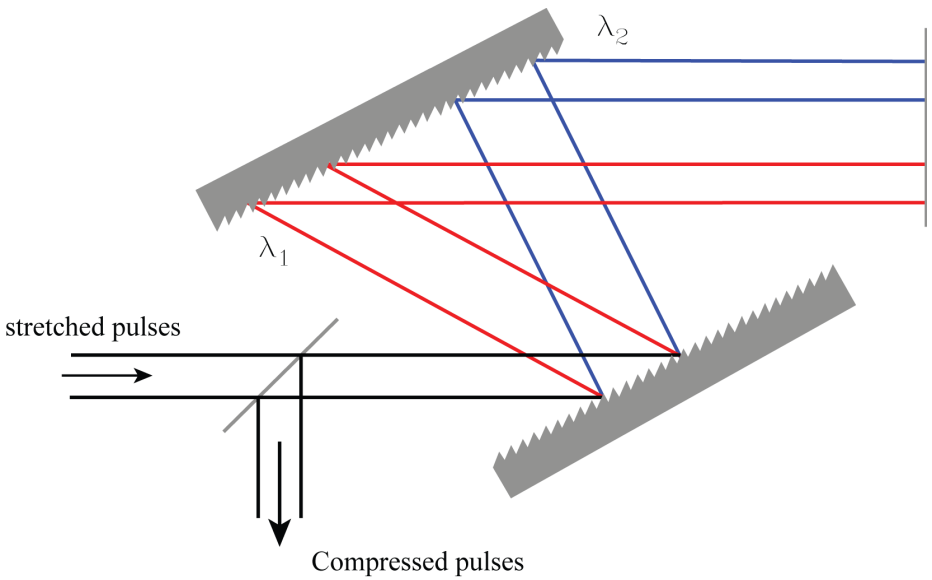

Figure 4.3: Grating compressor for the amplifier. Longer wavelengths λ_1 travel a longer path than shorter wavelengths λ_2, thus compressing the chirped pulse. Adapted from [3]

4.1.3 Optical Parametric Amplifier

Infrared pulses from the amplifier are converted into visible pulses by the nonlinear process of Optical Parametric Amplification (OPA) [36]. Photons from an intense beam at a wavelength λ_1 are converted parametrically into photons of a different wavelength, λ_2, by overlapping with a seed beam into a material with a strong second order nonlinearity ($\chi^{(2)}$). This parametric down-conversion process is depicted in Fig. 4.4 (b) and (c). In practice, the ~ 4 μJ pulses from the 250 kHz Rega amplifier are doubled to 400 nm on a BBO crystal, this beam is mixed with the white light continuum generated by the infrared pulses focused on a sapphire disc. The white light and the pump beams are overlapped in the second BBO crystal, where the parametric down-conversion process converts pump photons into certain components of the white beam. The wavelength at the output is that of the component of the white light that phase-matches with the 400 nm pump. The phase matching conditions can be expressed in the form

$$\omega_{\text{pump}} = \omega_{\text{signal}} + \omega_{\text{idler}} \tag{4.1}$$

$$\mathbf{k}_{\text{pump}} = \mathbf{k}_{\text{signal}} + \mathbf{k}_{\text{idler}}. \tag{4.2}$$

These conditions determine which wavelengths of the white light continuum the pump photons are converted into. Tunability in the wavelength is achieved by rotating the non-linear crystal, the range covers most of the visible spectrum, $480 - 700$ nm. From the phase matching equations we can obtain an equation that relates the wavelengths of the three outputs,

$$\frac{n_1}{\lambda_{\text{pump}}} = \frac{n_2}{\lambda_{\text{signal}}} + \frac{n_3}{\lambda_{\text{idler}}}. \tag{4.3}$$

Here, n_1, n_2 and n_3 are the indices of refraction for the pump, signal and idler beams, respectively. This states that the phase matching wavelength that satisfies Eq. (4.3) can be tuned by changing the angle between the optical axis of the BBO

and the propagating direction [37].

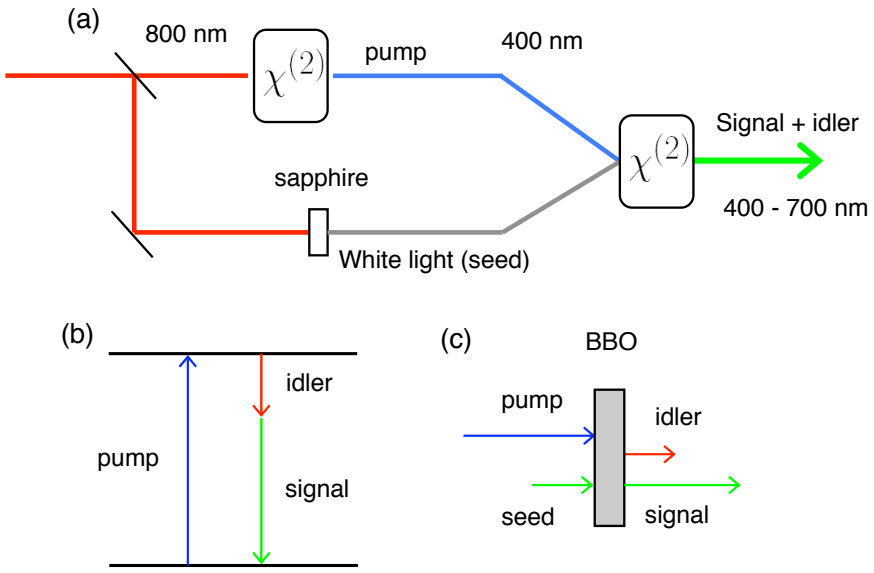

Figure 4.4: Optical Parametric Amplification process. (a) Photons from the 800 nm are frequency doubled to 400 nm and then converted into visible light by mixing with the white light spectrum. (b) Diagram of the resulting frequencies.

Figure 4.5 shows a diagram of the double pass OPA system. The infrared pulses from the amplifier are split at the first beam splitter. The weak arm generates a white light continuum by focusing 25 % of the infrared light onto a sapphire disc. The optical process of self phase modulation is responsible for the generation of the extra frequencies in the sapphire; an intense laser pulse propagating in a medium experiences third order non-linear effects, (χ^3), that cause an intensity dependent refractive index in the material given by $n[I(t)] = n_0 + n_2 I(t)$, where $I(t)$ is the intensity envelope of the pulse. This time-varying refractive index gives a time dependent phase of the optical pulse, $\phi(t) = \omega_0 t - k_0 n(t) L$, where ω_0 and k_0 are the center frequency and wavevector of the pulse and L is the propagation distance in the sapphire. In the frequency domain, the time-varying phase translates into an instantaneous time-dependent frequency $\omega(t)$. As a consequence, the frequency spectrum of the laser pulse broadens as it travels through the material resulting in a (highly-chirped) broad white-light continuum. Part of this broad spectrum is used

as the seed in the parametric amplification.

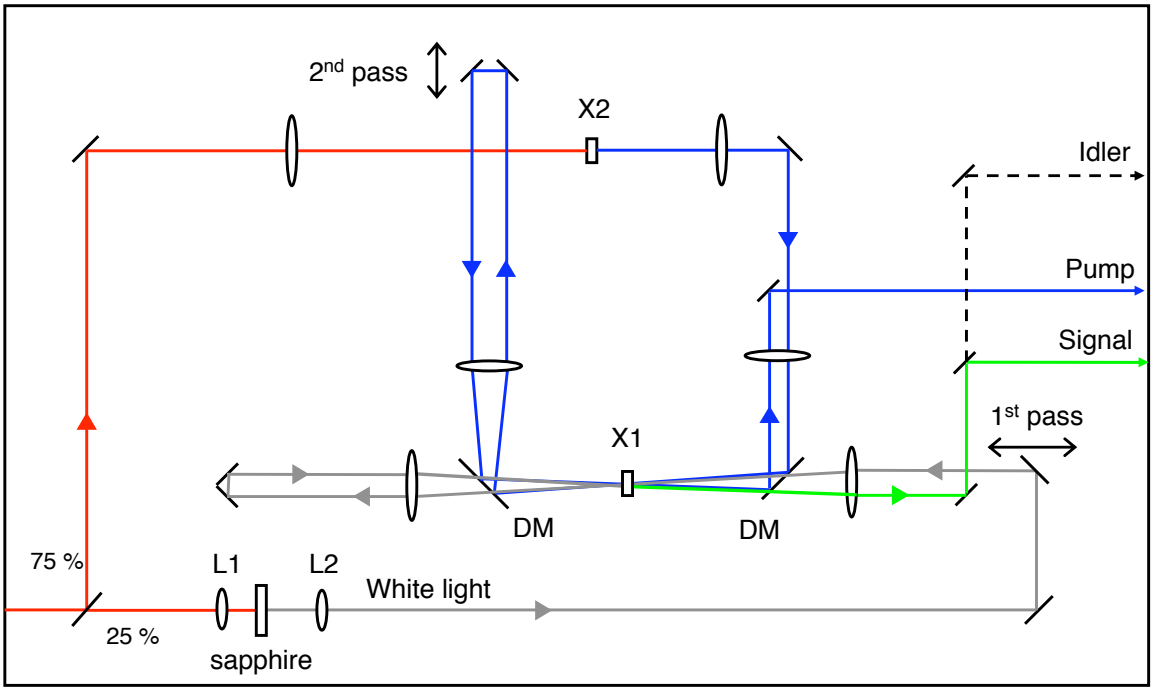

Figure 4.5: Schematic of the Coherent OPA system used in our experiments. 800 nm pulses are doubled on a BBO (X2) and overlapped with white-light on a second BBO (X1) where the visible pulses are generated by down-conversion. Two passes are required to obtain ~ 100 nJ of energy in the output pulse. L1-L2: lenses, DM: dichroic mirror.

The remaining 75 % of the Rega beam is frequency-doubled on a Type I BBO crystal and both beams are focused and overlapped on the second BBO crystal (X1). The time delay between the pump and the white-light arm is controlled by two manual delay-stages. To obtain ~ 100 nJ of energy, the pulses are overlapped twice on the X1 crystal. Since the white light is highly chirped, after tuning the phase matching angle of the X1 crystal the timing has to be slightly readjusted to recover the same output power. The output of the system in the signal is in the range $480 - 700$ nm and the idler is $940 - 2400$ nm.

In order to compensate for dispersion in the BBO crystals and the lenses inside the OPA, the resulting pulses have to be recompressed to achieve a minimum pulse duration of ~ 70 fs at visible wavelengths. Figure 4.6 shows the arrangement of

prisms to impart negative chirp to the laser pulses (from [4]). Since most materials at visible wavelengths have positive group velocity dispersion, i.e. $D = -\frac{\lambda}{c}\frac{d^2n}{d\lambda^2} > 0$, a negative chirp compensates for the dispersion introduced in the OPA. The prism arrangement can be folded by placing a mirror, $M - M'$. A thorough description of the prism compressor can be found in [35]. When compensating small amounts of dispersion, the double prism compressor is the preferred approach over the grating compressor discussed earlier. The pair of gratings can compensate the extremely chirped pulses used in chirped pulse amplification, but usually have losses that are larger than that of prisms and are more expensive.

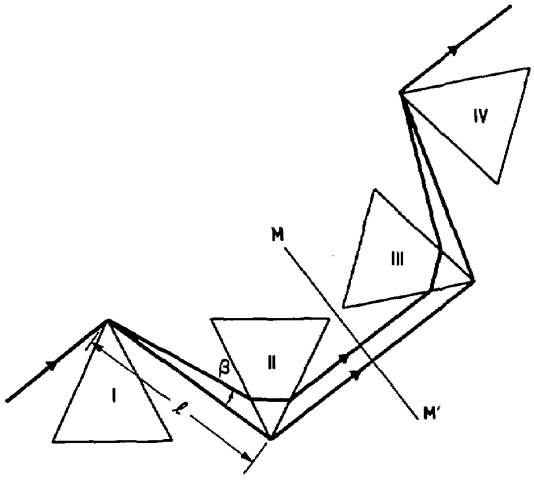

Figure 4.6: Prism compressor for the visible OPA. This arrangement gives negative chirp to the pulses. In practice the setup is folded by placing a mirror $M - M'$ and slightly tilting the returning beam in the vertical plane. From [4].

4.1.4 Pump-Probe setup

The pump-probe setup is shown in Fig. 4.7. Any of the laser sources described above can be used in this setup. The steering optics consist of metallic mirrors that provide a broadband of wavelengths of operation from the visible to the near-infrared. The beam is split into, typically, 90% and 10% for the pump and the probe respectively. The pump beam is chopped at a frequency of 2 kHz with a mechanical chopper. The chopper controller outputs the operating frequency as a sine-wave signal that is later used as the reference in the lock-in detection. The probe reflects from a retro reflector mounted on a mechanical delay stage that allows precise control of the time delay between the pump and the probe pulses. Typical time delays of up to 2 ns can be achieved with this stage. The minimum step size of 1 μm corresponds to a time delay of 6.66 fs which is much smaller than the pulse duration of any of our lasers.

We used lenses of $f = 15$ cm and $f = 10$ cm to focus the pump and the probe, respectively, onto the sample surface. This gives a probe waist at the focus that is smaller than that of the pump, ensuring that the excitation generated by the pump is homogeneous in the region sampled by the probe. The typical spot diameter for the probe at a wavelength of 800 nm is ~ 30 μm with an initial beam 3 mm in diameter. Typical laser power at the sample was ~ 2 mW for the pump beam which, with a beam diameter of 50 μm, corresponds to a fluence $F = P/(r \times A) \approx 1$ mJ/cm^2, where P is the average optical power, r is the repetition rate and A is the area of the illuminated spot. The optical reference is taken by splitting the probe before the sample. The reflected light was collected with a lens of focal length $f = 200$ mm and focused onto the detector. In order to reduce the scattered light from the pump reaching the detector, the polarization of the pump was set orthogonal to that of the probe. In this way, a polarizer before the detector blocks the unwanted scattered light from the pump.

We used a balanced photodetector (New Focus, Nirvana 2007). It consists of

a pair of photodiodes with individual amplifiers and sophisticated auto-balance electronics. In balanced mode, the output is proportional to the difference between the optical power in the signal diode and the optical power in the reference diode. The auto-balanced feature automatically adjusts the gain in the reference amplifier to keep the DC output (below certain cut-off frequency) at zero voltage. The cutoff frequency is selected by a dial on the detector box. In this operation mode, the optimum condition is to use a reference beam of twice the power in the signal and the auto-balance circuit will adjust the gain correctly. However, the bandwidth of the detector is 125 kHz, near the repetition rate of the Rega amplifier. This means that the detector can "see" individual pulses from the laser, rendering the auto-balance unusable at this repetition rate. But since the signal of interest from the chopper is at much lower frequency, 2 kHz, we can safely low-pass the output of the Nirvana with a 10 kHz cut-off filter and manually balance the output with a linear-graded neutral density filter. The low-pass filtered signal is used as the input channel of a lock-in amplifier (Stanford Research Systems, SRS-830) and the chopper signal at 2 kHz is used as the reference of the lock-in. The lock-in amplifier detects in the signal channel any signature at the frequency of the reference. Its output is essentially the DC component of the product of the two inputs [38]. The SRS-830 has a minimum sensitivity of 2 nV with nominal noise of 6 nV/$\sqrt{\text{Hz}}$. We used a time constant of 30 ms in all the experiments, which translates into a band around the frequency of the reference of $\sim$ 33 Hz.

From the cryogenic equipment available in the group, we used two helium optical cryostats. For the early experiments we used an Oxford Research helium-reservoir cryostat that has a liquid helium reservoir, a liquid nitrogen reservoir and a vacuum outer shield. The later experiments were performed with a helium-flow cryostat (Janis Research, STVP-400). Although a flow cryostat cannot reach temperatures below $\sim$ 10 K, it is more stable and, since it does not have a nitrogen reservoir it is

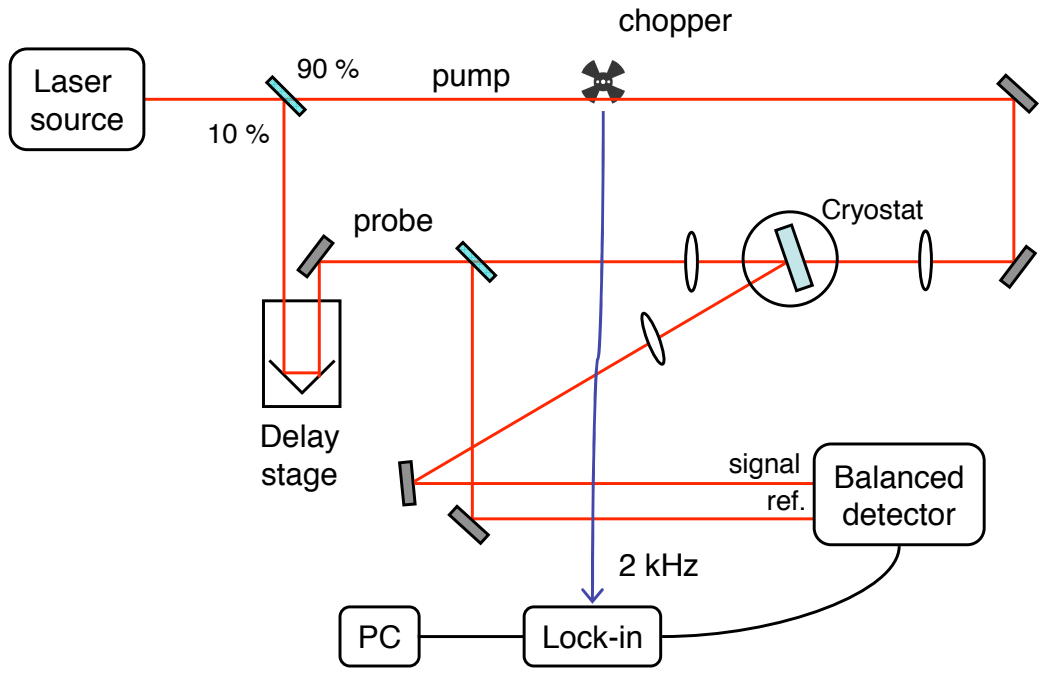

Figure 4.7: Schematic of the setup for the optical pump-probe experiments. The laser beam is split into 90% and 10% for the pump and the probe respectively. The pump is chopped 2 kHz and the probe goes through a translational stage which controls the time delay. Both beams are then focused on the sample and the probe is collected and focused on a balanced photodetector.

much more straight-forward to work with. The disadvantage is that the cryostat has to be connected to the Helium dewar during the experiment which could result in vibrations introduced from the helium flow into the cryostat.

4.1.5 Etching procedures

Some of the samples studied in this work are semiconductor superlattices of gallium arsenide (GaAs) and aluminium arsenide (AlAs), grown by molecular beam epitaxy (MBE) on GaAs substrates. One of the experiments described in Chapter V required that we remove the substrate completely. There are well known methods and chemical agents to selectively remove the GaAs substrate. The procedure requires to first polish mechanically the 0.5 mm-thick substrate to a thickness of less than ~ 10 μm. We used a transparent unoriented sapphire disc of 1" diameter to hold the sample during the polishing and etching. The sample is attached to the disc with

a wax that does not react with the etching solution. We used a mixture of 500 ml of Hydrogen Peroxide (H_2O_2) and 6 ml of Ammonium Hydroxide (NH_4OH). The solution is placed in a plastic container and a small pump circulates the fluid over the sample. To minimize evaporation of the toxic vapors from the mixture we cooled the solution to ≤ 10 °C.

4.2 Ultrafast X-ray diffraction techniques

In contrast to the laser technology presented above, the generation of ultrashort X-ray pulses is still under development. There are currently two approaches to generate short X-ray pulses. One makes use of very intense laser pulses to create a plasma where high energy electrons undergo bremsstrahlung and produce characteristic X-ray radiation [39]. In this case, the X-ray pulse duration is comparable to that of the laser source but is emitted isotropically and requires collection and focusing optics [40, 41]. On the other hand, radiation produced in a third generation synchrotron is orders of magnitude brighter and collimated; however, the pulse duration is limited by the electron bunch in the storage ring [42], typically of the order of a hundred ps.

In this section I discuss the concepts and equipment relevant to ultrafast X-ray diffraction experiments using synchrotron-based X rays. I begin with a derivation of the radiation produced by an undulator and later I review the equipment for the time-resolved X-ray diffraction experiments.

4.2.1 Synchrotron radiation from an undulator

There are different approaches to generate synchrotron radiation from relativistic electrons [43]. A bending magnet is the simplest example where electrons are bent into a circular orbit by a strong magnetic field, causing them to radiate. The spectrum of the bending magnet radiation is very broad and the radiation is not collimated. Alternatively the electrons can be sent through an undulator, which consists of a series of alternating magnets of opposite polarity. Such configuration produces an alternating force on the charge making the particles orbit quasi-sinusoidal trajectories. This approach has the advantage of producing a highly collimated, bright beam of X rays with a very narrow energy distribution.

Consider a charged particle with speed $v = c\beta$, where c is the speed of light, as it

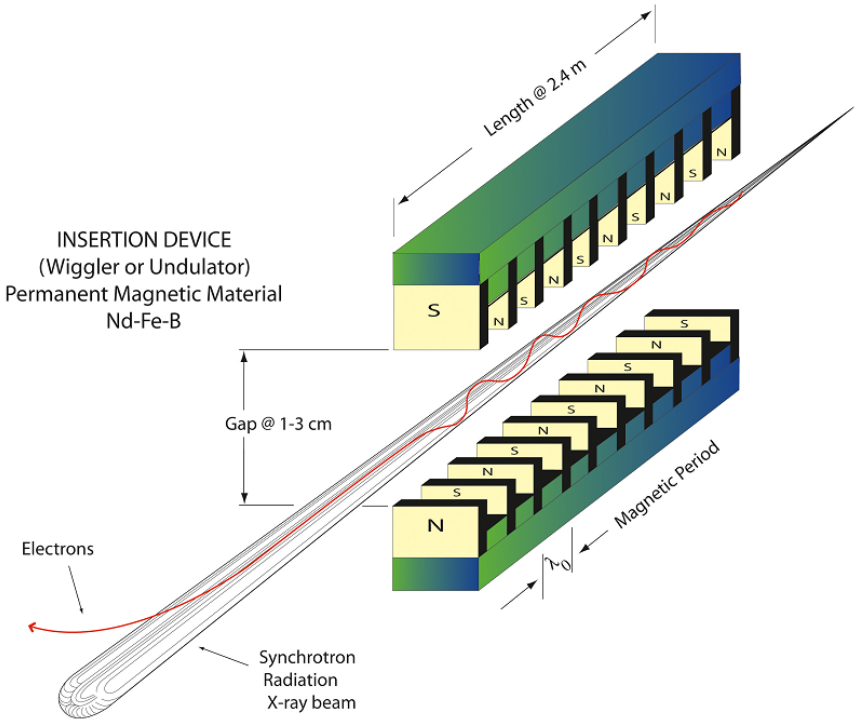

Figure 4.8: A charged particle traveling through an alternating series of magnets emits a sharp collimated beam of monochromatic radiation in the forward direction, from [5].

passes through an undulator with period λ_u. The magnetic field strength is B and there are a total of N periods. Since the charge is moving at relativistic speed, the undulator appears contracted in the reference frame of the electrons. The undulator period seen by the electrons is

$$\lambda'_u = \frac{\lambda_u}{\gamma}.$$

As the electrons wiggle through the magnets, they emit radiation of wavelength λ'_u. In the laboratory reference frame, this radiation is Doppler-shifted and appears with a wavelength

$$\lambda = \lambda'_u \gamma(1 - \beta\cos\theta) = \lambda_u(1 - \beta\cos\theta).$$

Since $\beta \sim 1$, the radiation is confined to a narrow cone near the forward direction ($\theta \approx 0$). The factor between parenthesis is very small and we can take $\cos\theta \simeq 1 - \theta^2/2$

to get the emission wavelength

$$\lambda = \frac{\lambda_u}{2\gamma^2}\left(1 + \beta\gamma^2\theta^2\right) \simeq \frac{\lambda_u}{2\gamma^2}\left(1 + \gamma^2\theta^2\right). \tag{4.4}$$

This is called the *simplified undulator equation*. A more elaborate treatment accounting for the transverse motion of the electrons gives an additional term that depends on the magnetic field, B [42],

$$\lambda \simeq \frac{\lambda_u}{2\gamma^2}\left(1 + \frac{1}{2}K^2 + \gamma^2\theta^2\right), \tag{4.5}$$

where $K = eB\lambda_u/2\pi mc$, and e and m are the charge and the mass of the electron. By adjusting the magnetic field strength we have some tunability of the energy of the emitted X rays. In practice, this is done by changing the gap between the magnets in the undulator.

In addition to the X rays radiated in the forward direction, there is a continuum of radiation coming from the motion in each individual period like in a bending magnet. This background contribution is not confined to $\theta \approx 0$ and can be blocked by appropriately placed slits along the beamline. It is also important to note that, since the motion is not exactly sinusoidal, and because of the symmetry of the orbit, all the odd harmonics of the wavelength in Eq. (4.5) are present. This is called the "white" beam in the synchrotron terminology and is usually filtered to a single harmonic before being used for diffraction.

4.2.2 Synchrotron source

The X-ray experiments in this thesis were done at the Advanced Photon Source (APS), a 3rd generation synchrotron X-ray source that is part of the Argonne National Laboratory (ANL) located outside Chicago, IL. An aerial view of the experimental facility is shown in Fig. 4.9. Electrons are produced by a cathode heated to 1100 °C and accelerated to 450 MeV by alternating electric fields in a

Figure 4.9: Aerial view of the Advanced Photon Source.

linear accelerator. Subsequently, the race-track shaped booster synchrotron increases the energy of the electron beam to ~ 7 GeV (see diagram in Fig. 4.10). The beam is steered and collimated by a series of bending and focusing magnets. The electrons are then injected into the 1104-meters-circumference storage ring where the beam is carefully collimated and optimized for the production of synchrotron radiation. A relevant parameter to measure the quality of the electron beam is the *emittance*, which is the product of the transverse size of the beam and its divergence. In 3rd generation synchrotrons this is very low, on the order of $2 - 10$ nm rad in the horizontal direction and 0.068 nm rad in the vertical direction. Another important parameter is the *brilliance*, defined as the photon flux emitted per solid angle, per unit transverse area and per bandwidth. It is expressed in $photons/s\,mrad\,mm^2\,(0.1\%\,\delta\lambda/\lambda)$ and for typical undulators is in the range $10^{19} - 10^{21}$ $photons/s\,mrad\,mm^2\,(0.1\%\,\delta\lambda/\lambda)$.

The radio-frequency (RF) potential in the storage ring accelerates the electrons as they lose energy in the circular orbit due to synchrotron radiation. The potential

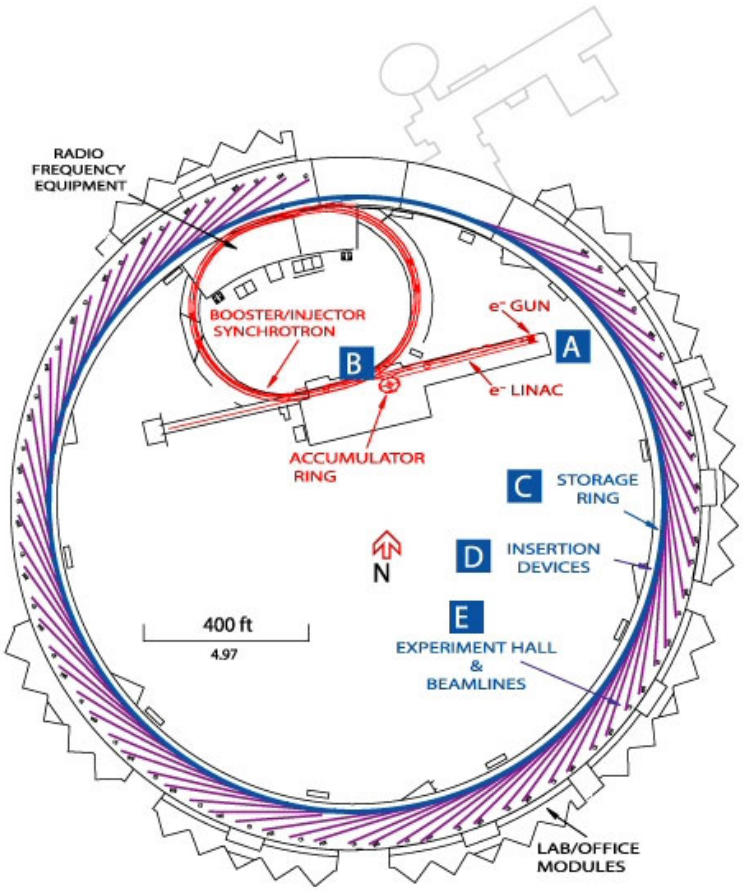

Figure 4.10: Diagram of the APS synchrotron. Electrons are accelerated to 7 GeV and stored in the storage ring where they are sent through insertion devices (IDs) to generate synchrotron radiation.

consists of a series of minima (buckets) where the electrons form bunches of charge that circulate around the ring. A total of 1296 buckets can be accommodated in a full circumference. Depending on the operation mode, different number of buckets are filled. For example, in the 1296-mode each bucket is filled with electrons, while in 24-bunch mode only one every 54 contains electrons. If N is the number of filled buckets in the circumference, the X-ray repetition rate is N times the ring fundamental frequency $P_0 = 272$ kHz. Most of our experiments run in the 24-bunch mode, in which the repetition rate is 6.528 MHz and the time between bunches is 152 ns. The reference RF from the storage ring, 1296×272 kHz $= 352$ MHz, is

obtained from the accelerating RF and is equal to the total number of buckets.

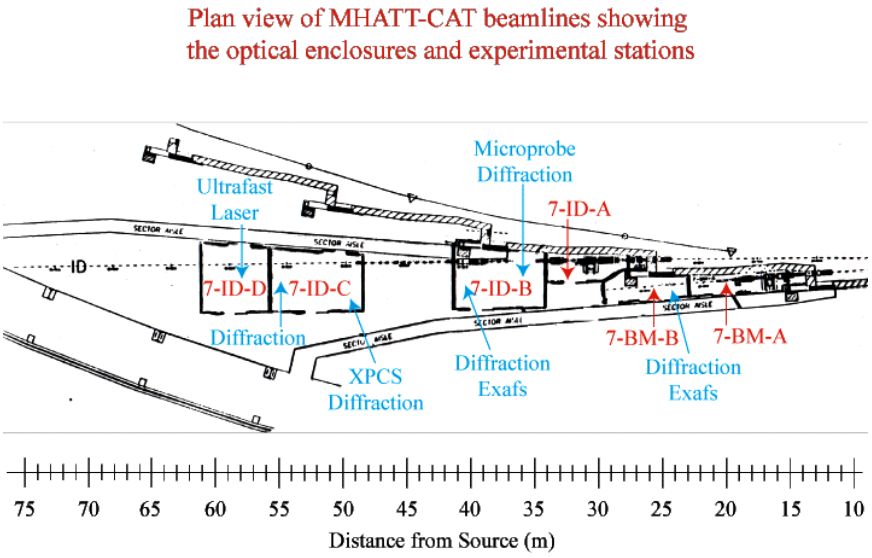

Figure 4.11: Floor plan of the sector-7 insertion device at the APS.

A layout of Sector 7, the MHATT-CAT/XOR beamline is shown in Fig. 4.11. The beamline consists of several experimental hutches, labeled A, B, C and D where different types of experiments and/or diagnostics take place. The undulator is located before the A hutch, near the electron storage ring. A diamond monochromator is located in the A hutch. Different X-ray experiments take place in hutches B, C and D. The time resolved experiments were performed in hutches C and D. The X-ray beam is transported between the hutches under vacuum to avoid attenuation due to scattering and absorption in air.

The white beam produced by the undulator is not suitable for diffraction experiments. It contains a broad continuum background of off-axis radiation, and odd harmonics of the fundamental frequency in the forward direction. In a diffraction experiment one usually wants highly monochromatic radiation. In order to obtain monochromatic, highly directional X rays, the beam is collimated with a set of slits and spectrally filtered with a double crystal monochromator in the non-dispersive setting [44]. An aperture of $\sim 500\ \mu\text{m} \times 500\ \mu\text{m}$ is enough to block the

off-axis radiation. After the slits, the harmonics are eliminated by a diamond-crystal monochromator, shown schematically in Fig. 4.12. The Bragg reflection from a single diamond crystal disperses the polychromatic beam into different angles. At the second crystal, only one wavelength satisfies the Bragg condition for the same angle of incidence. By slightly tilting the second crystal, the Bragg condition is mainly satisfied by the fundamental wavelength and the harmonics are suppressed. The final energy spread depends on the Darwin width (the angular width of the reflected X-ray radiation) of the crystals used in the monochromator; for 14.3 keV photons the energy spread of a diamond monochromator is ~ 0.8 eV. The number of photons in the monochromatized beam is of the order of 10^6 photons per pulse.

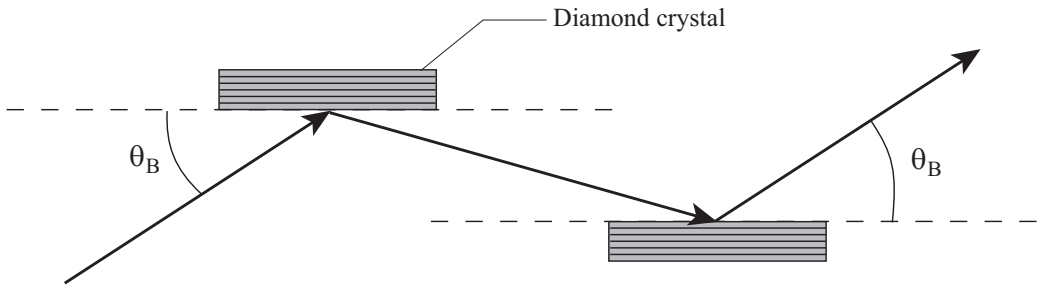

Figure 4.12: Double diamond-crystal monochromator in the parallel setting. The energy resolution depends on the Darwin width of the crystals, in this case $\Delta E/E \approx 5.6 \times 10^{-5}$.

4.2.3 Laser and timing electronics

In the time resolved X-ray diffraction experiments, the generation of acoustic strain is done with optical laser pulses, as described in the previous section. In contrast to the optical experiments where the pump and the probe were obtained from the same laser, the X rays and the laser pulses are generated from different sources. This presents an additional experimental challenge because the sources are not synchronized and therefore exhibit intrinsic time-jitter. This can be overcome by using a feedback-loop to fix the laser repetition rate to the synchrotron RF reference.

As shown in Fig. 4.13, a Ti:Sapphire oscillator produces low energy pulses of

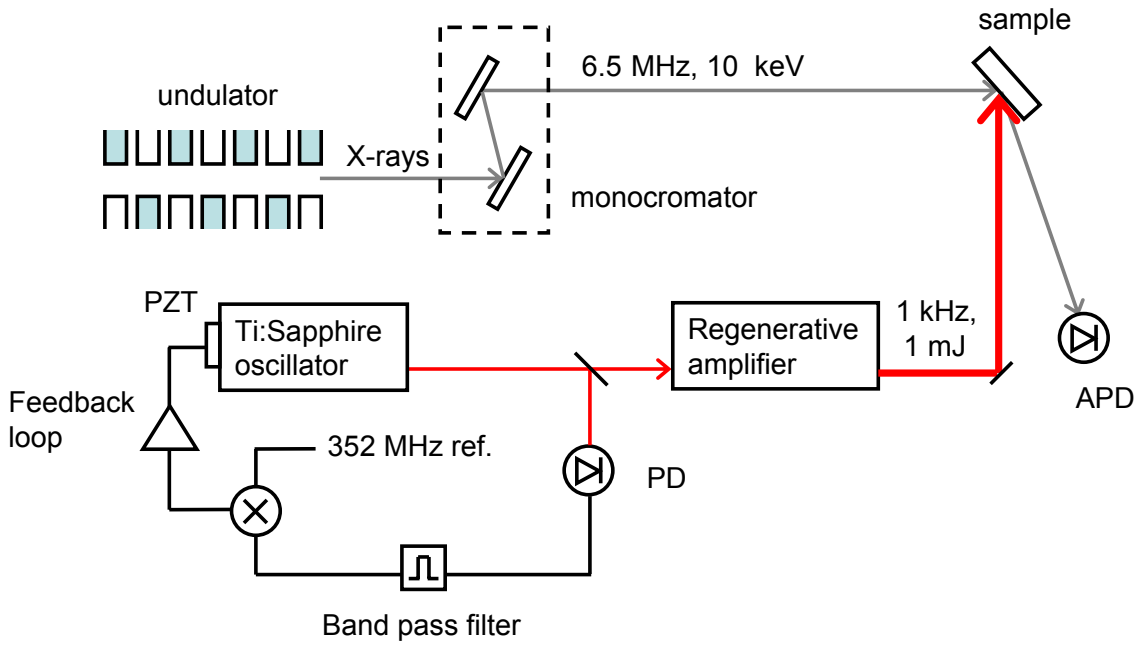

Figure 4.13: Schematics of the setup for time resolved experiments at Sector-7. Pulses from a Ti:Sapphire are amplified to 1 mJ per pulse and used to excite the sample. The repetition frequency of the oscillator is controlled by the PZT transducer that drives the end mirror of the cavity. The feedback loop locks this repetition rate to the X-ray reference.

$\sim$ 50 fs duration at 88 MHz that are amplified with a regenerative amplifier to an energy of $\sim$ 1 mJ per pulse at a rate $\sim$ 1 kHz. The end mirror of the oscillator cavity is mounted on a piezo-electric transducer (PZT). Moving the mirror with the transducer changes the total length of the cavity and therefore the round trip of the pulses inside the cavity. In this way, the laser can be locked to the X-ray repetition frequency by properly manipulating the PZT. The oscillator is locked to the 4th sub-harmonic of the ring reference $f_{\rm ref}$ in the following way. The signal from the laser is measured with a fast rise-time photodiode and filtered at its 4th harmonic near 352 MHz. This is then mixed with the X-ray reference signal at $f_{\rm ref}$. If f_l is the frequency of the measured signal, the output of the mixer gives two components at $f_l \pm f_{\rm ref}$. A low-pass filter after the mixer yields a signal at the frequency offset, $\Delta f = f_l - f_{\rm ref}$, which is used as the input of the feedback loop of the driving circuit of the PZT. The feedback circuit minimizes the error signal by adjusting the PZT

element, with the net effect of locking the repetition rate to f_{ref}. The time delay between the X-ray bunches and the laser pulses can be controlled by adding a phase to the reference signal with a digital phase shifter. The minimum resolution of the phase shifter is 19 ps, smaller than the X-ray pulse duration and the maximum phase shift yields a time delay of 4.75 ns. Delays longer than this value can be attained with a commercial digital delay generator (Stanford Research, SRS-535). We performed the data acquisition by gating the X-ray pulses synchronized with the laser as shown in Fig 4.14.

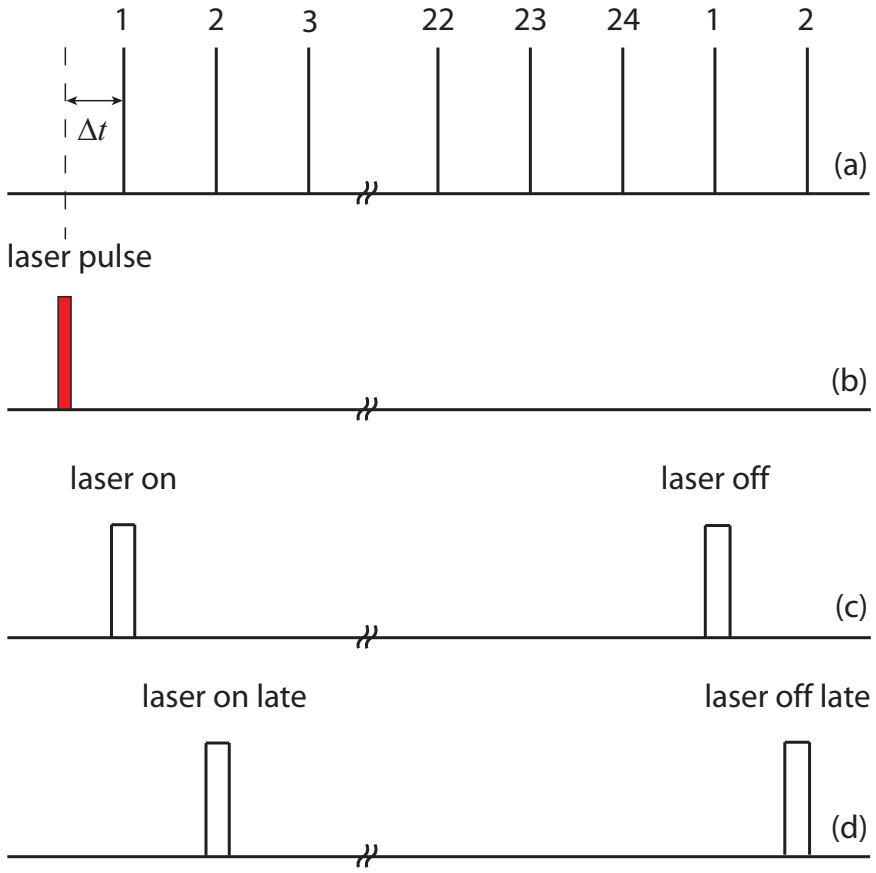

Figure 4.14: Diagram of the logic gates used to record the time-resolved diffraction from individual bunches. (a) the 24-bunch mode of the synchrotron. (b) the laser arrives at a given instant with respect to the synchrotron bunches. (c) the "laser on" gate records the intensity at a given time delay, Δt, after the laser arrives. For normalization, the "laser on late" records X-ray photons from the same bunch one revolution later without the laser. (d) "laser off" records the diffraction from the next bunch which corresponds to a delay of $\Delta t + 152$ ns.

The sample is mounted on a six circle Huber diffractometer that allows precise

control of the sample orientation and the detector position. A photograph of the apparatus can be seen in Fig. 4.15.

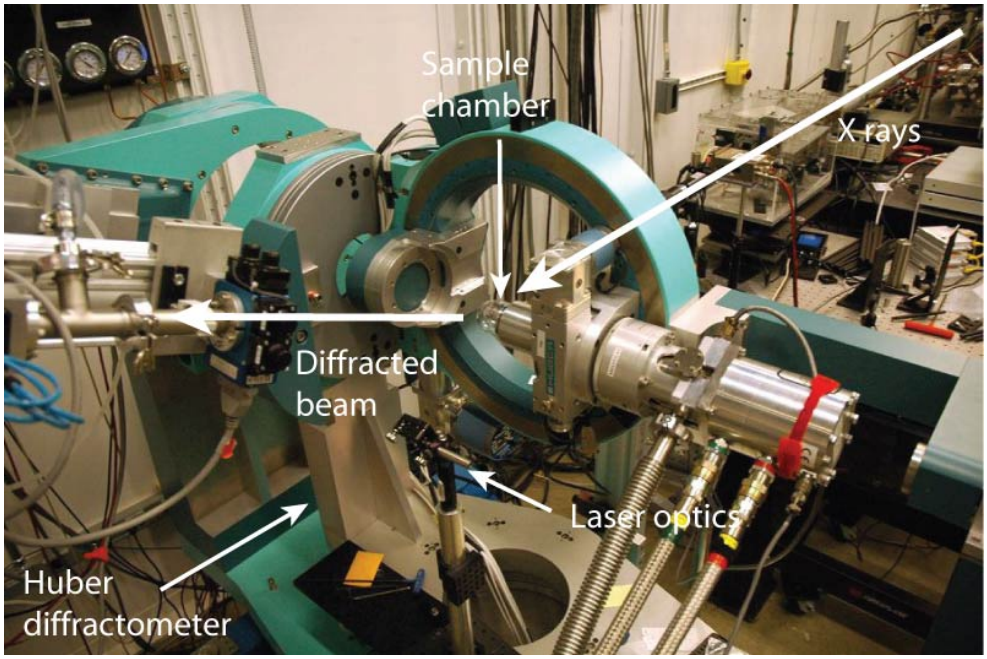

Figure 4.15: Photograph of the apparatus for X-ray diffraction.

4.2.4 Detectors and X-ray optics

An ionization chamber is a device used to measure ionizing radiation, in particular X rays. It consists of a gas enclosed by two conducting electrodes at different potentials. When X-ray photons travel through the gas (in our case, air) the high energy photons ionize the molecules in the air, producing free charges that are accelerated towards the conducting plates. The accelerated charges manifest themselves as an ionization current which is proportional to the X-ray flux. Due to the its slow time response, the ionization chamber is only sensitive to the integrated X-ray flux and cannot distinguish individual X-ray pulses, however, these chambers do not require complicated electronics and are easy to set up making them idea for monitoring the overall X-ray flux. For the time resolved experiments, we used an avalanche photodiode (APD) with a rise-time of $5 - 10$ ns. This detector is analogous to a

photomultiplier, except that the photocurrent is generated and amplified in a reverse biased semiconductor.

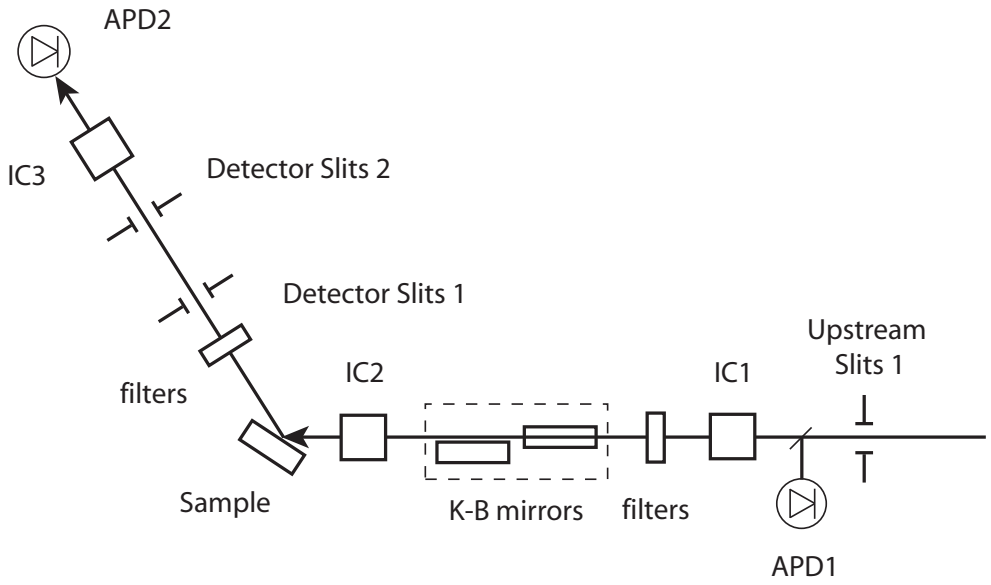

Figure 4.16: Schematic view of the beamline showing the different X-ray diagnostic and focusing elements.

We used a pair of Kirkpatrick-Baez (K-B) mirrors to focus the beam on the sample. The K-B mirrors consist of Rhodium-coated Si crystals oriented at grazing incidence which reflect the X-ray beam by total internal reflection. Focusing is achieved by slightly bending of the crystals. The position of the mirrors can be controlled for fine alignment and both mirrors are enclosed in a helium gas chamber to avoid oxidizing the surfaces.

A highly collimated beam is desirable for diffraction experiments. Usually one wants a beam with a very narrow distribution of incident wavevectors. This is a limiting factor in the angular resolution. For this reason, focusing of the X-ray beam is done only in the horizontal direction, perpendicular to the scattering plane. This increases the X-ray intensity at the sample without compromising the angular resolution.

A diagram of the different elements along the beamline inside the C hutch is

shown in Fig. 4.16. The first slit collimates the beam to 600 μm $\times$ 600 μm. The avalanche photodiode (APD1) monitors the intensity of individual bunches, while the first ionization chamber (IC1) reads the average flux. One of the K-B mirrors is used to focus the beam in the horizontal plane. A second ionization chamber, IC2, is used to read the transmitted X-ray flux after the K-B setup. On the detector arm we have two slits that are aligned with the straight X-ray beam and are set to the beam FWHM. The second slits are set to twice the size of the first, typically 240 μm $\times$ 550 μm. An ionization chamber (IC3) also records the average flux reaching the detector (APD2).

CHAPTER V

FEMTOSECOND LASER STUDIES OF ACOUSTIC WAVES FROM SUPERLATTICES

In this chapter the results from the ultrafast optical experiments on semiconductor superlattices are discussed. The first section deals with the study of propagating acoustic waves using a two-superlattice approach. The second section shows results on a single structure in which we find evidence of the existence of surface-avoiding waves.

5.1 Double-superlattice scheme for the study of acoustic phonons

The study of laser-excited acoustic waves using short laser pulses has led to the development of a technique termed picosecond ultrasonics in which the absorption of a laser pulse by a metallic layer induces a sudden temperature rise that generates a traveling acoustic strain wave [12, 13]. The wavelength of the acoustic wave is determined by the absorption length in the metallic layer [12]. Alternatively, high frequency ultrasound can be generated by light pulses using periodic structures such as superlattices [45, 46, 47, 48, 49, 27, 17]. The zone-folding of the acoustic branches into the mini-Brillouin zone creates optical modes of the superlattice with non-zero frequency at the Brillouin zone center that can couple to light [9]. Propagating folded acoustic phonons have been studied using two-color pump-probe experiments [17], where the pump and probe are absorbed in different regions inside the sample, or by

generating folded phonons with a superlattice and detecting with a superconducting bolometer [18].

Here, I present a scheme to study the propagation of folded acoustic phonons that uses superlattices as a means to couple light pulses to high frequency acoustic vibrations. The superlattices act as acoustic transducers and are spatially separated, allowing for the study of the propagation of such high frequency acoustic waves. The use of a second superlattice as a transducer, as opposed to a filter, as in Ref. [18], allows us to measure the frequency spectrum of the propagating acoustic wave, and potentially the attenuation of different frequency components.

5.1.1 Front-side excitation

We studied two samples grown by molecular beam epitaxy on a (001) GaAs substrate that consist of a thick GaAs layer of 1.2 μm or 0.6 μm between two identical superlattices of 25 periods of 12 Å-thick GaAs/34 Å-thick AlAs. In what follows, we refer to these samples as A and B, respectively. The substrate has been removed by chemical etching. The samples were characterized by spontaneous Raman measurements. Spectra obtained with the 514.5 nm line of an Argon-ion laser in the backscattering geometry show a doublet near ~ 1 THz that corresponds to the first zone-center folded acoustic modes [11], as shown in Fig. 5.1. The frequencies obtained from these experiments match the calculated ones using the continuum elastic model for the infinite structure introduced in Chapter II.

In Fig. 5.2 we show differential reflectivity results from a standard pump-probe experiment on sample B in the geometry where the pump and probe overlapped on the front side. These experiments were performed at $T = 40$ K with ~ 80 nJ laser pulses from an optical parametric amplifier (OPA) centered at the wavelength $\lambda = 530$ nm. The time-resolved data in Fig. 5.2 (a) reveals an oscillation of 13 ps together with complex structures at the beginning and at the end of the trace, as well

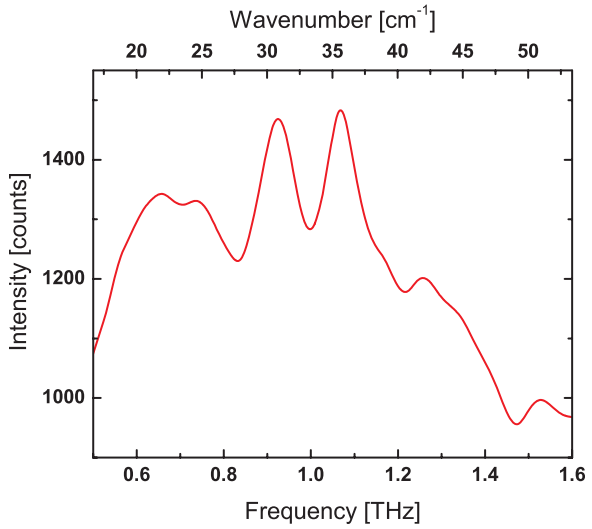

Figure 5.1: Spontaneous Raman spectrum of sample A in the back-scattering geometry taken with the 514.5 nm line of an argon laser.

as a double structure at 180 ps. Complex electronic, as well as thermal, relaxation processes give rise to the slowly-varying contribution to $\Delta R/R$ with a time scale of hundreds of ps. The structure at the beginning and at the end of the trace are the acoustic pulse generated by the laser and the acoustic echo, after it reflects from the back surface and arrives at the front superlattice. This wave-packet consists of a sound pulse with a broadband spectrum centered at $\nu_0 = v/\xi$ in the lowest acoustic branch, where ξ is the absorption length of the laser in the superlattice [13]. Note that the scan is symmetric around $t = 180$ ps, which is the time it takes for the sound wave to reach the back surface. The broad double peak appearing at ~ 150 ps is due to residual laser light exciting the second superlattice, thus generating strain from the back surface that reaches the front in half of the acoustic round trip.

Fig. 5.2 (b) shows the low frequency part of the Fourier transform of the data in Fig. 5.2 (a). The spectrum reveals a peak at $\nu = 75$ GHz, which is due to stimulated Brillouin scattering from the traveling acoustic wave [12], a structure at lower frequencies, and an overall modulation of the spectrum with spacing $\Delta\nu = 3$ GHz. This latter frequency corresponds to the inverse of the acoustic round-trip time ~ 300 ps indicating that the modulation of the spectrum has to do with the

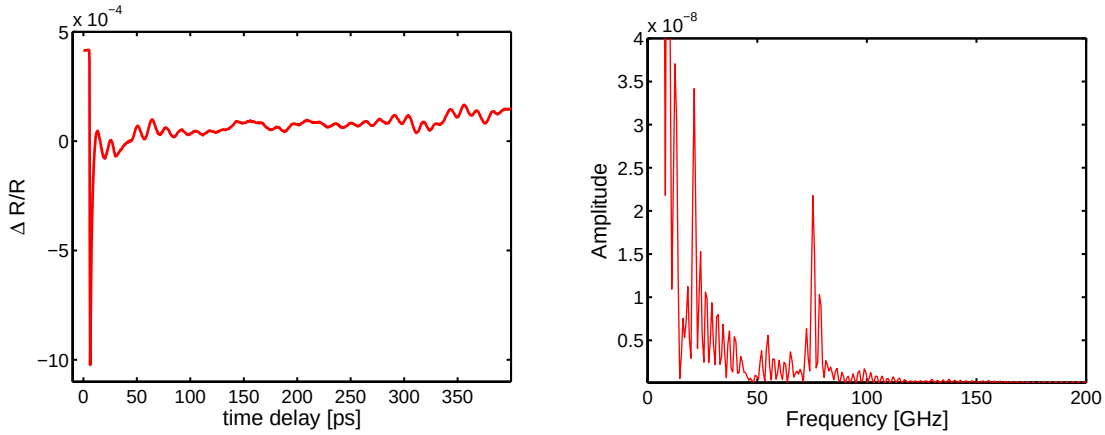

(a) (b)

Figure 5.2: (a) Pump-probe differential reflectivity for the sample with a 0.6 μm bulk layer. The scan is symmetric around $t = 180$ ps. The complex structure is due to acoustic strain traveling through the bulk layer and reflecting from the back surface. (b) FFT of the scan in (a) showing the low frequency stimulated Brillouin at ~ 75 GHz and fringes due to the acoustic echo.

interference of the contributions from the acoustic wave, and its delayed echo.

5.1.2 Back-side excitation

Here we present the results on the generation and remote detection of folded acoustic phonons. The geometry of the experiment is shown in Fig. 5.3. The absorption of the pump pulse in one of the superlattices launches a wave packet of high-frequency folded phonons that propagates towards the second superlattice where it is detected by a delayed probe pulse. This particular design makes it possible to generate and detect folded phonons in spatially-separated regions. The second superlattice is accessed by chemical etching of the GaAs substrate, as described in Chapter IV.

In Fig. 5.4 we show time-resolved differential reflectivity for the two samples at 77 K. In this experiment we used $\sim$ 80 nJ pulses centered at a wavelength $\lambda = 530$ nm. The pump and probe beams were focused on the sample with lenses of focal lengths $f = 15$ cm and $f = 10$ cm, respectively.

Figure 5.4 (a) presents a time-trace for the configuration in which the pump and the probe strike on the same superlattice (in this case on sample A). The data exhibit a high frequency oscillation superimposed on top of a large, lower frequency

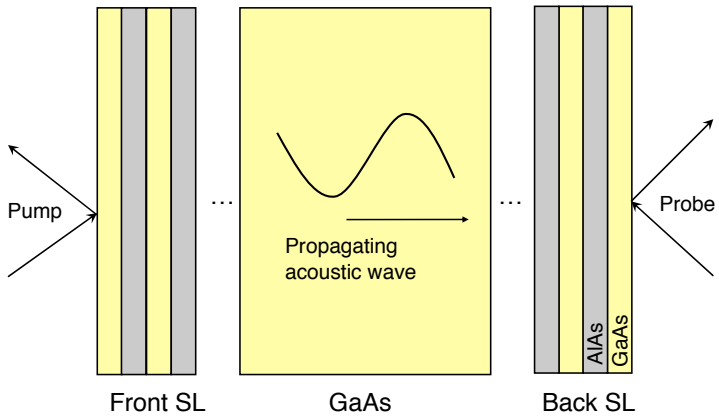

Figure 5.3: Schematic diagram of the double superlattice structure and the geometry of the pump-probe experiments. The samples consist of a thick GaAs layer of 1.2 μm or 0.6 μm between two identical superlattices.

vibration that is the stimulated Brillouin scattering already mentioned. Results for the situation in which the pump and the probe impinge on opposite sides are shown in Fig. 5.4 (b). For samples A and B we observe, respectively, an oscillating transient in the reflectivity arriving after time delays of ~ 125 ps and ~ 250 ps. These values agree well with the time-of-flight of acoustic waves traveling across the sample. We note that the high frequency folded phonons also reach the second superlattice, as can be seen in Fig. 5.5, which is an expanded view of the region near the arrival of the acoustic signal in Fig. 5.4 (b). The amplitude of the oscillation due to the folded phonons is nearly the same in the data of Fig. 5.4 (a) and Fig. 5.4 (b), indicating that the excitation propagates without a measurable attenuation through the GaAs layer. In addition, the folded phonon signal is delayed from the Brillouin oscillation, as can be seen in Fig. 5.5. The low-frequency oscillation arrives at ~ 250 ps while the folded phonons only appear after ~ 275 ps. This delay of $\Delta\tau \approx 25$ ps arises from the fact that the two excitations are generated at different depths in the sample. If the folded phonons are created near the middle of the superlattice, at $z_{\rm fp} = L_{\rm SL}/2 = 70$ nm, the time it takes for them to be detected at the same depth on the opposite side is $\tau_{\rm fp} = 279$ ps. The Brillouin oscillation, but not the folded

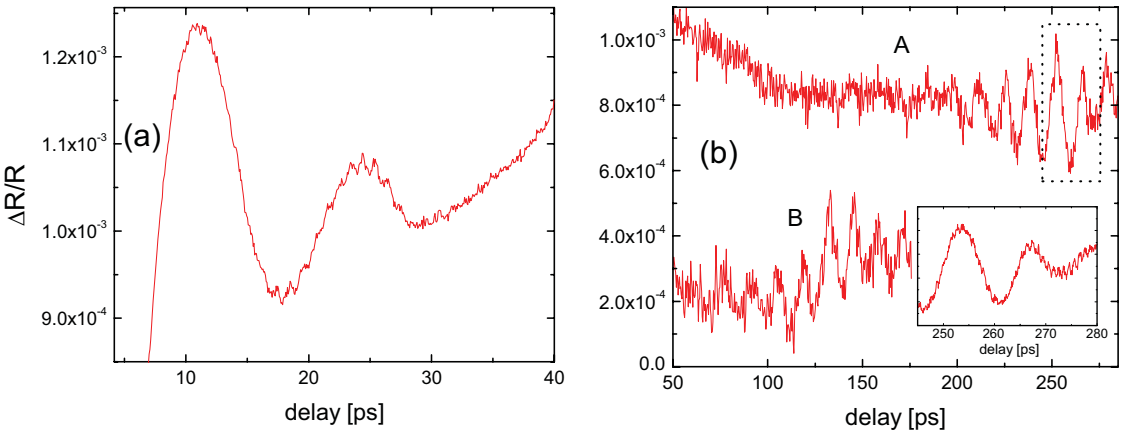

Figure 5.4: Time-domain data for samples A and B. Pump pulses generate sound waves on the front superlattice, that are later detected on the front (a) and the backside (b) of the sample. Trace (a) and the inset of (b), obtained on sample A, show folded-phonon oscillations superimposed on the larger, low-frequency oscillations associated with stimulated Brillouin scattering.

phonons, can be detected by the probe if the light reaches the bulk layer. Therefore, the lower-frequency oscillation generated in the bulk layer would be detected after the transit time through the bulk, i.e. $\tau_{\mathrm{B}} = 1.2\ \mu\mathrm{m}/v_{\mathrm{GaAs}} = 256$ ps. Under these considerations, the folded phonons and the low frequency modes are delayed by $\Delta\tau = 23$ ps, which is close to the delay we observe in Fig. 5.5. Furthermore, we will see below that the delay between the two signals can also be recognized in the Fourier transform as an overall modulation of the spectrum.

Curve (a) in Fig. 5.6 shows the Fourier transform of the trace presented in Fig. 5.5. There are four main features present, namely: The Brillouin scattering peak at 70 GHz (not shown in the figure) and a triplet due to zone-center folded phonons near 1 THz. Two modes of the triplet correspond to the back-scattering wavevector (BS) while the remaining one (FS) originates from the zone-center mode, which is Raman active [11]. As we saw in Chapter III, the frequency of the BS modes, as well as the Brillouin peak, is determined by the wavelength of the probe pulse. This dependence can be understood from the argument given in Chapter III as follows. Recall that the change in reflectivity, Eq. (3.24), is an overlap of the strain eigenmode

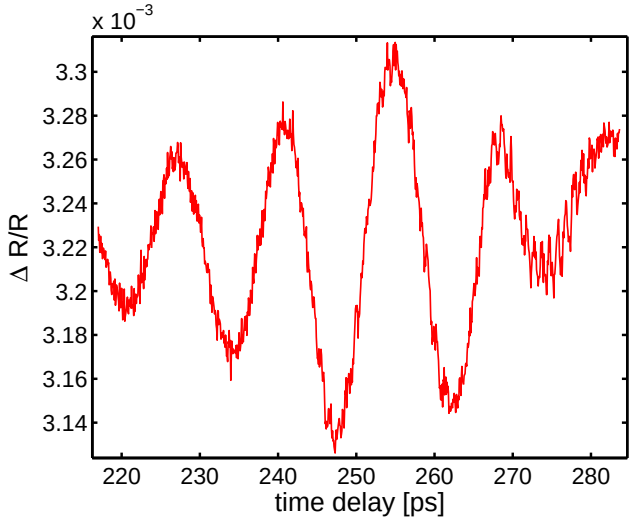

Figure 5.5: Folded phonon reflectivity signal from sample A detected on the back superlattice. Note that the high-frequency wave appears delayed from the Brillouin oscillations.

with the probe electric field. In the semi-infinite case, Eq. (3.27), the reflectivity has non-zero contributions from those components of η that satisfy the phase matching condition $q = \pm 2k_p$. This means that, regardless of the generation mechanism, the probe selects only those modes that satisfy wavevector conservation. Furthermore, the propagating strain pulse moves at the speed of sound and, therefore, the corresponding frequency for the phase matched low frequency oscillations in Fig. 5.4 is $\nu_{\rm BR} = k_p/\pi v$ where v is the speed of sound of the superlattice. For the same reasons, the folded phonon doublet at ~ 1 THz is composed of modes which, in the extended zone scheme, have wavevectors $q = 2\pi/D \pm 2k_p$, where D is the superlattice period.

We now compare the experimental data with the results of the model introduced in Chapter III. The use of a continuum model for structures with such small periods is somewhat arguable since the bulk properties of each constituent are not well defined and, hence, the local index of refraction or, equivalently, the absorbed energy in each layer is not known. With this in mind, we adjusted the ratio $K_{\rm GaAs}/K_{\rm AlAs}$ in Eq. (3.17) to reproduce the relative intensities of the observed modes. We emphasize that, regardless of the generation mechanism, the waves are detected by stimulated

light scattering through the photoelastic mechanism, as stated in Eq. (3.24).

Calculated spectra are shown in Figs. 5.6 (b) and (c), together with the experimental result (a). The best fit was obtained for $K_{\mathrm{GaAs}}/K_{\mathrm{AlAs}} = 1.2$. For reference, we have included the dispersion relation for the infinite superlattice (lower panel). In the spectrum corresponding to a single semi-infinite superlattice, Fig. 5.6 (c), the flat features with zero intensity at 0.5 THz and 1 THz correspond to the acoustic minigaps whereas the doublet at $\sim$ 1 THz corresponds to the folded phonons typically observed in back-scattering Raman spectra [9].

Figure 5.6 (b) shows the calculated spectrum for the finite superlattice in the case where the probe is incident on the second superlattice. The calculations exhibit a complex structure with an overall modulation of the intensity, which is also visible on the lower side of the measured spectrum in (a). The frequency spacing of the comb-like structure is $\Delta\nu \sim 40$ GHz. This value corresponds to the inverse of the transit time of the acoustic pulse through the superlattice. This periodic modulation manifests itself in the time domain traces as a time delayed signal. We note that as we anticipated earlier, the delay between the folded phonons and the Brillouin signal in Fig. 5.5 is consistent with our interpretation of the frequency comb in the spectrum.

The folded phonons in Fig. 5.6 (b) also show a fine structure which arises from the finite size of the superlattice. In the experimental data, this fine structure is particularly evident in the higher frequency BS-peak. In addition, the peak at the zone center (FS) is also visible. This feature appears stronger in the experiment than what is expected from the calculations. We tentatively attribute this discrepancy to the interface contribution to Δr [27], which is not taken into account in Eq. (3.24).

To understand the origin of the surface contribution we need to reconsider the argument that leads to Eq. (3.21) in Chapter III. The dielectric constant at a given

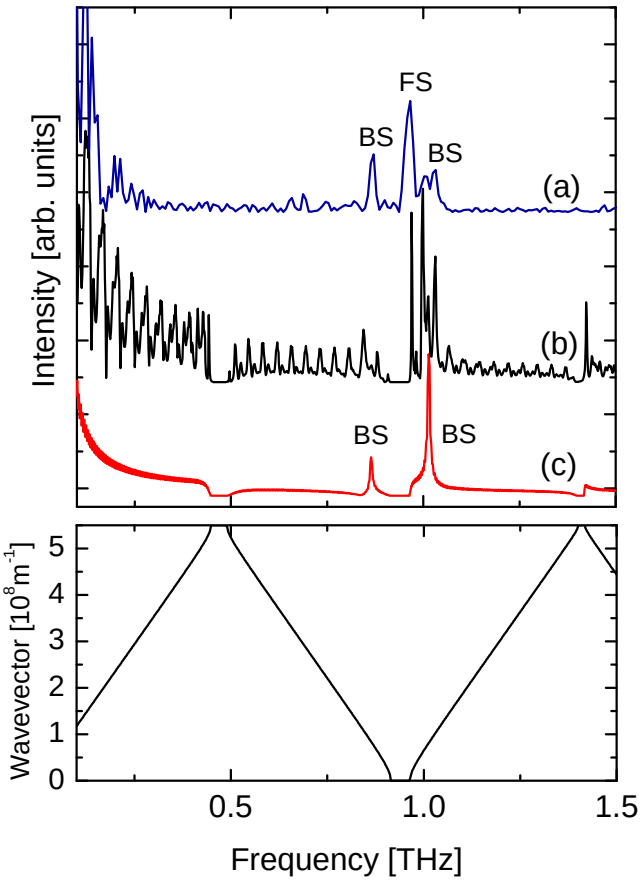

Figure 5.6: (a) Fourier transform of the time trace for sample A. We observe three peaks that correspond to the backscattering (BS) and forward scattering (FS) modes accessible in Raman experiments; (b) calculated spectrum for the double superlattice structure, where the probe is incident on the second superlattice and (c) calculated spectrum for a semi-infinite structure showing the BS doublet. The lower panel shows the dispersion relation for an infinite superlattice.

depth, z, in the perturbed material is given by [50]

$$\epsilon'(z) = \epsilon[z - u(z,t)] + \Delta\epsilon(z,t), \tag{5.1}$$

where $\Delta\epsilon(z,t) = P(z)\eta(z,t)$ is the change in the dielectric constant induced by the acoustic strain, $\eta = \partial u(z,t)/\partial z$, and $\epsilon[z - u(z,t)]$ is the unperturbed quantity at the displaced position $z - u(z,t)$. The second term in this equation is the so called "bulk", or photoelastic contribution, and has an associated change in reflectivity given by Eq. (3.21). Moreover, the motion of the interfaces gives rise to an

additional contribution from the first term in Eq. (5.1). Normally in a bulk material, where there is only one interface, this additional contribution gives a change in the reflection coefficient proportional to the surface displacement, $\Delta r = -2ik_0\delta z(t)$, which is purely imaginary and, from the arguments given in Chapter III, it does not affect the reflectivity and can be omitted in most treatments. In a multilayer, on the other hand, interference between the reflected and transmitted light from each interface leads to a complex contribution to the reflectance [29],

$$\frac{\Delta r}{r} \propto \sum_{j=1}^{N} E_j^2(z_j)(\epsilon_j - \epsilon_{j+1})u(z_j), \tag{5.2}$$

where $u(z)$ is the atomic displacement, ϵ_j is the dielectric constant in layer j, and $E(z)$ is the electric field of the probe. Clearly, since $\Delta R = 2\mathrm{Re}\{\Delta r\}$, the interference of the light scattered from the moving interfaces has an effect in the reflectivity, ΔR.

Equation (5.2) adds a contribution to Δr from acoustic modes that do not necessarily phase match with the optical probe in the sense of Eq. (3.21). The stronger modes, that is, the modes with bigger displacements, $u(z)$, contribute more to this term. Moreover, a consequence of Eq. (3.17) is that modes at the zone-center of the Brillouin zone are excited more strongly, and therefore, the contribution to ΔR from Eq. (5.2) is dominated by modes at $q \approx 0$. This explains the unexpected intensity of the FS peak in Fig. 5.6.

5.2 Long-lifetime acoustic mode

In the previous section we measured the spectrum of the propagating waves by detecting the acoustic excitations reaching the second superlattice. We show in this section that not all the acoustic modes generated by the laser pulse leak out of the superlattice. We conducted experiments on a single superlattice of 75 periods of $d_{\mathrm{GaAs}} = 59$ Å and $d_{\mathrm{AlAs}} = 23.5$ Å grown by MBE on a (001) oriented GaAs substrate. A 70 nm layer of AlAs was deposited between the superlattice and the

substrate to stop the chemical etching process. This sample has longer period than the one studied in the previous section, corresponding to a first folded minigap at a frequency of ~ 0.6 THz. Clearly, the acoustic spectrum of a longer period structure is less sensitive to interface roughness and inter-diffusion. In addition, the longer period enhances the excitation of the folded phonons for the same optical-pulse intensity [see (Eq. 3.19), which states that the amplitude of the eigenmode decays inversely proportional to its frequency].

5.2.1 Above-gap excitation

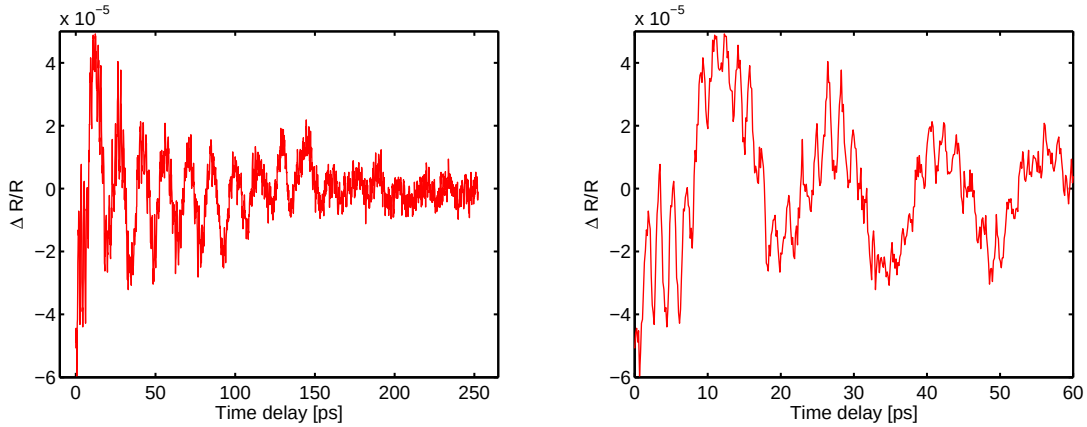

Figure 5.7: (a) Differential reflectivity data at 300 K. The slowly varying background due to the electronic response has been subtracted. The central wavelength of the laser pulses is $\lambda_L = 546$ nm. (b) Same data showing oscillations due to folded phonons.

Figure 5.7 (a) shows the differential optical reflectivity as a function of the probe delay. In this case, the central wavelength of the laser was tuned to resonate with the superlattice at $\lambda_L = 546$ nm, tentatively ascribed to the $\Gamma - X$ transition. The signal shows a slowly varying electronic background on the order of $\Delta R/R \sim 10^{-3}$, which was subtracted numerically in Fig. 5.7 (a). The phonon-induced part of the differential reflectivity is dominated by the usual Brillouin oscillation, in this case at ~ 70 GHz, together with higher frequency folded-phonon oscillations, as it can be seen in Fig. 5.7 (b).

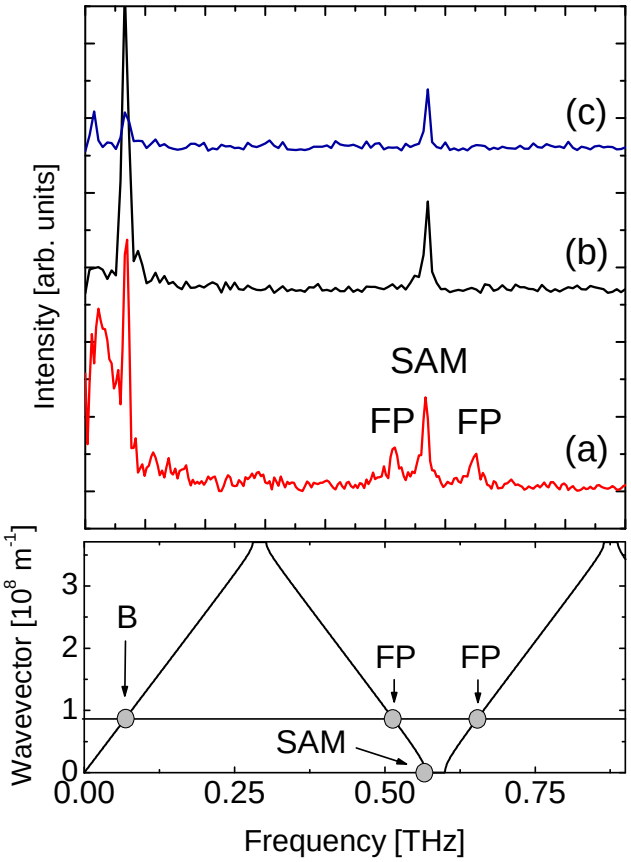

Figure 5.8: Fourier transform of time-domain data as in Fig. 5.7 for the intervals: 10-125 ps (a), 250 - 350 ps (b) and 350 - 500 ps (c). The bottom panel shows the acoustic dispersion relation calculated with Rytov's model. SAM is the surface avoiding mode, FP are the folded phonons at q_{BS} and B is the peak due to stimulated Brillouin scattering.

Figure 5.8 (a) shows the Fourier Transform (FT) of the time trace of Fig. 5.7, which exhibits similar features as the data from the double superlattice in Fig. 5.6. Four features are clear in the FT, a strong peak at lower frequency and a folded phonon triplet near 0.6 THz. The dominant peak in Fig. 5.8 (a) corresponds to the stimulated Brillouin scattering component also observed in the previous section, and is indicative of a wave traveling at the speed of sound in the material. As before, in the lower panel of Fig. 5.8 we show the calculated acoustic dispersion relation for this superlattice.

The triplet at 0.6 THz consists of the two folded phonons at the back-scattering wavevector, q_{BS}, and a peak in between, labeled SAM (Surface Avoiding Mode), that we assign to the forward-scattering component from the near-zone-center mode. The lower panel in Fig. 5.8 shows the acoustic dispersion calculated with Rytov's model [10] for the parameters of the structure. The period of the superlattice was slightly modified in the calculation to match the first folded doublet to the experimental data. The important point from Fig. 5.8 is that the SAM remains detectable even after ~ 500 ps, much longer than the other three oscillations. Since the probe can only detect folded phonons in the superlattice, this clearly shows that the $q \approx 0$ mode stays inside the superlattice while the other ones leak into the substrate. Considering that the transit time of the acoustic wave through the superlattice is 130 ps, even after 250 ps there are no BS peaks in the signal (b). The Brillouin mode is still visible in trace (b), possibly because the probe could reflect from the low frequency wave in the substrate. Since there is no folding of the acoustic branch in the substrate, the folded phonons are not visible. We attribute this unusual long lifetime of the observed SAM peak to surface-avoidance.

Figure 5.9 shows a numerical solution of the wave equation, Eq. (3.2), by the method of finite differences in time-domain (FDTD). This approach is more convenient for calculating the strain evolution than the eigenmode expansion shown in Chapter III. However, if we want to calculate the spectrum of the reflectivity, Eq. (3.29) is clearly a better way. For the purpose of illustration, we start with an initial condition given by a gaussian strain pulse modulated by a square wave, $\eta(t=0) = K(z) \times \exp[-(z-z_0)^2/\sigma^2]$, (curve (a) in the top panel). This ensures that the initial strain starts in the superlattice and, because of the factor $K(z)$, it has the periodicity of the superlattice. The initial strain splits into two counter-propagating waves as seen in (b) at $t = 500$ steps. The left-going wave is inverted upon reflection at the free surface (c) and eventually also leaves the superlattice (d). At longer

times, in (e), the wave-packet is a superposition of modes near the zone-center, which have wavelengths that match the superlattice period. At even later times, (f), the remaining wave is composed of mostly the surface-avoiding mode closest to the zone-center.

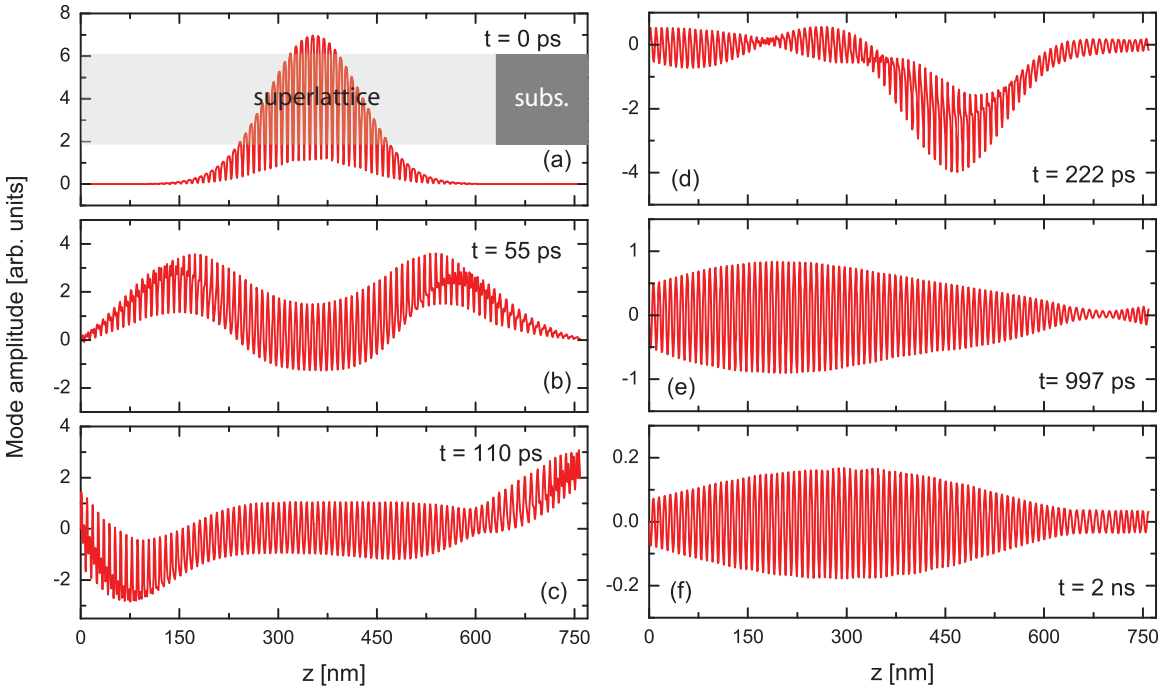

Figure 5.9: Snapshots of the strain, starting with an initial gaussian wave modulated by the function $K(z)$. The initial strain propagates from the superlattice into the substrate (a), (b) and (c). The superlattice acts as a cavity that keeps the surface-avoiding modes near $q = 0$ inside the superlattice, (d), (e) and (f).

In Chapter III we saw that the eigenmodes of a superlattice near $q = 0$ avoid the boundaries of the superlattice. Figure 3.6 (a) shows a few eigenmodes of this superlattice near the zone center as indicated schematically in Fig. 3.6 (b). This calculation was done with a substrate of 600 nm of GaAs. In 3.6 (c) we show the function G_n introduced in Chapter III near the first folded mini-gap, represented schematically in (b). This function determines the relative amplitudes of the eigenmodes after being excited by the laser pulse. As we can see in (c), modes that are surface avoiding such as 1 and 3 couple stronger with the excitation pulse than mode $2'$ which is essentially a substrate mode that goes in the superlattice. This

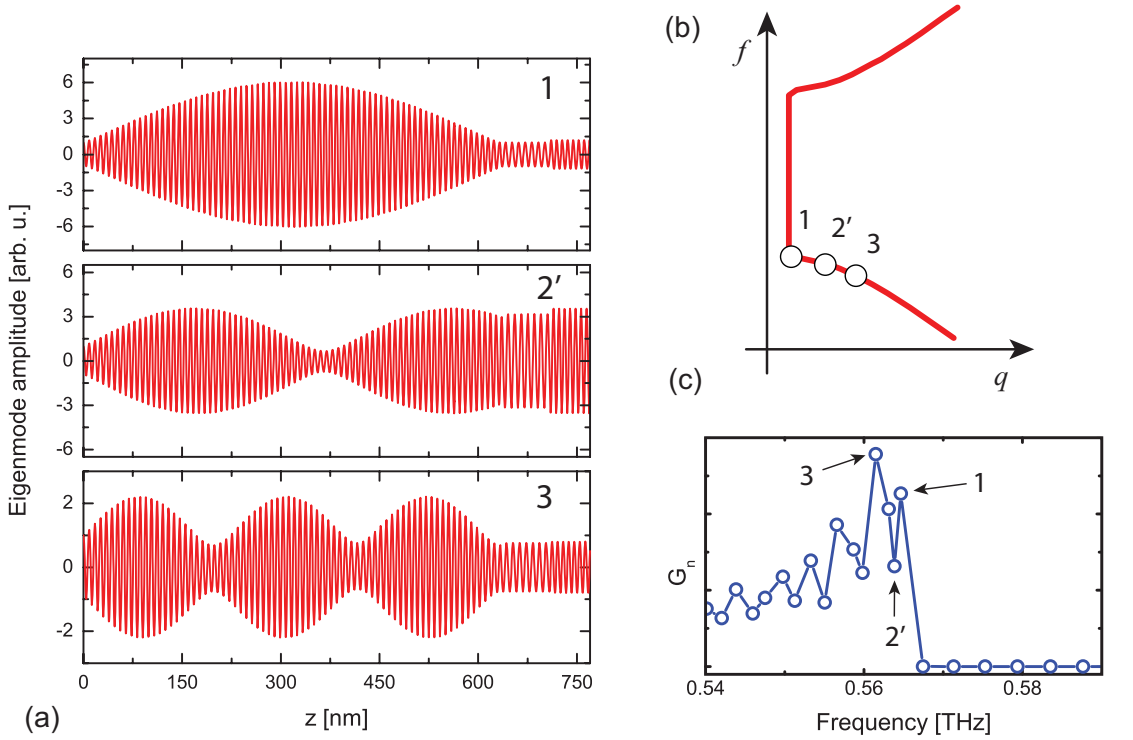

Figure 5.10: (a) A few eigenmodes near the first acoustic bad-gap at the zone center of the Brillouin zone (b). The function G_n defined in Chapter III determines the strength of the coupling of each mode with the laser pulse (c).

follows from Eq. (3.17) since modes with higher amplitude in the superlattice have a bigger overlap with the pump intensity and give a stronger contribution to the spectrum, $G_n(\omega)$. Note that mode $2'$ is the propagating counterpart of a substrate mode, as the GM in Fig. 3.6.

The number of substrate modes that occur between two surface-avoiding eigenmodes depends on the substrate thickness, since the total number of eigenmodes increases with the thickness. However, the surface-avoiding ones are superlattice modes, hence the number of peaks in the curve (c) depends on the number of periods in the superlattice, N. In a free-standing structure, the number of points in (c) is equal to N which is also the number of modes in each acoustic branch.

We can estimate an upper bound for the lifetime of the $q \approx 0$ mode based on the time of flight for the acoustic wave to cross the superlattice. If $\mathcal{R}$ is the acoustic

reflectivity of the superlattice-substrate interface and $v_g \approx 230$ m/s is the group velocity at $q = \pi/L$, where L is the thickness of the superlattice, the decay rate can be estimated as $\gamma^{-1} = v_g(1-\mathcal{R})/L = 5$ ns, which is consistent with our results. This value assumes that the only decay of the signal is due to the phonon leaving the superlattice. Other mechanisms such as anharmonicity can contribute to the phonon decay and shorten the measured lifetime.

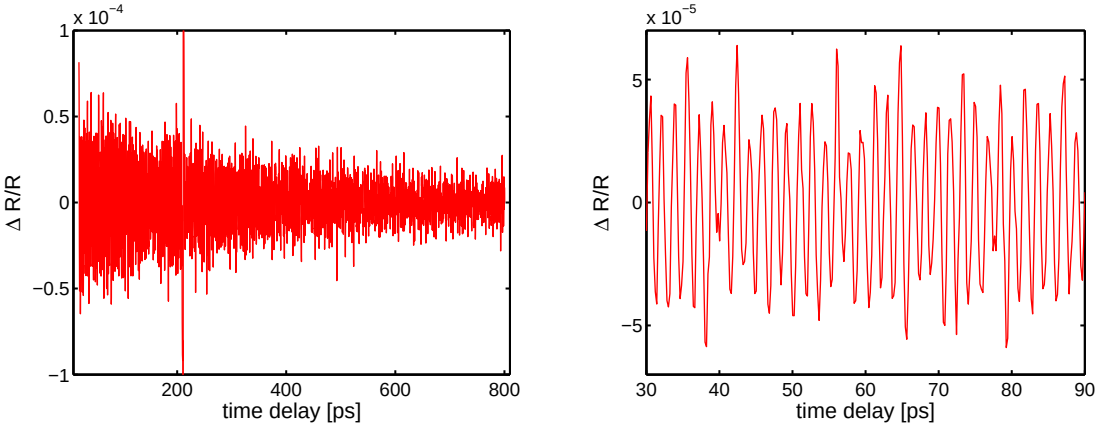

(a) (b)

Figure 5.11: Differential reflectivity with laser pulses with $\lambda = 800$ nm. (a) Long delay scan showing folded phonons up to 800 ps after initial excitation. (b) Expanded view of the same scan showing the monochromatic signal.

5.2.2 Below-gap excitation

As a final comment on the reflectivity measurements, we show in Fig. 5.11 results obtained with laser pulses centered at $\lambda = 800$ nm. In contrast with the previous data, this trace shows a much simpler behavior of a decaying oscillatory signal with a single frequency, as seen clearly in Fig. 5.11 (b). Since the laser energy is below the superlattice band-gap, neither the excitation nor the detection are mediated by real carriers; instead the acoustic folded phonons are generated through Impulsive Stimulated Raman scattering (ISRS) which, due to phase matching, leads to the excitation of only the $q = 0$ mode [27]. This explains the missing Brillouin oscillation in the time trace. The surface contribution to the differential reflectivity,

Eq. (5.2), is responsible for the detection, and since the only excited mode is the $q = 0$ surface-avoiding wave, the spectrum, Fig. 5.12, contains only one peak at the expected frequency. Note the logarithmic scale in this figure indicating that the trace from this acoustic mode is extremely long-lived. The lifetime of the $q = 0$ acoustic mode obtained from this trace is $\tau = 500$ ps.

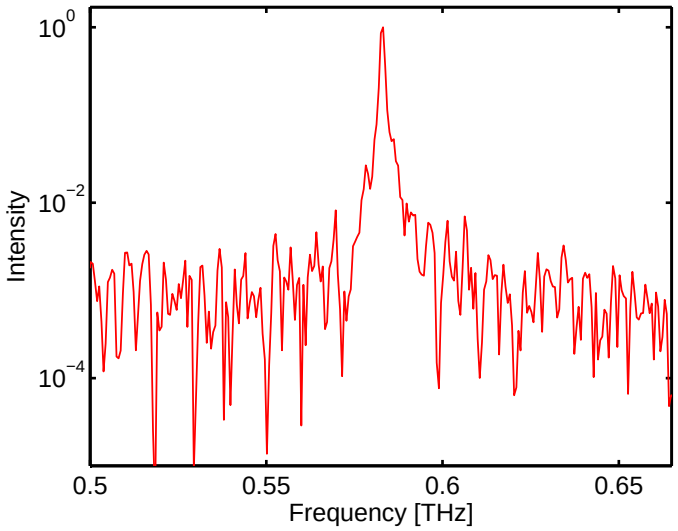

Figure 5.12: Fourier transform of the data in Fig. 5.11. The spectrum contains only one peak at the frequency of the zone-center mode.

CHAPTER VI

X-RAY STUDIES OF ACOUSTIC WAVES FROM SUPERLATTICES

We saw in Chapter III that the frequencies of the folded phonon doublet observed in an optical pump-probe experiment depend on the wavelength of the probe (see Eq. (3.21)). This shows one disadvantage of the all-optical pump-probe scheme: The excitation and the detection processes are coupled in the data, making it difficult to extract detailed information about the acoustic excitation. In addition, both the detection and the generation are mediated by electronic transitions, which determine the optical properties, and hence the data contains mixed information about the acoustic phonons and the electronic response. Our two-superlattice approach [32] provides information on the propagation of acoustic phonons by separating the detection from the generation, but it does not solve the problem of the electronic response. Alternative probes can provide complementary information. Stanton et. al. [18] used superconducting bolometers to estimate the bandwidth of the generated acoustic wave. Frequency selectivity is obtained in this approach with an additional superlattice filter in the detection.

In this Chapter, we present laser-pump X-ray probe experiments that aim to provide information on the spectrum of the folded acoustic phonons generated from semiconductor superlattices. Unlike optical excitation in solids, X-ray diffraction by acoustic modes is not mediated by valence intra- or inter-band electronic transitions. The X rays are scattered primarily by localized and tightly bound electrons in

the lattice ions. This gives X-ray diffraction great sensitivity to atomic motion and makes ultrafast X-ray scattering a great tool to study lattice dynamics. We first introduce the laws of X-ray diffraction by a periodic lattice, in particular the dynamical theory of diffraction. Next, we discuss the results of the time-resolved experiments.

6.1 Kinematic X-ray diffraction and Bragg's law

Since the wavelength of the X rays, λ, is of the order of the inter-atomic spacing in a solid, the three dimensional crystal can be regarded as an infinite set of parallel planes of atoms separated by a distance d that scatter the incident radiation (Fig. 6.1). The well known criteria for constructive interference of the scattered radiation,

$$\lambda = 2d \sin\theta, \tag{6.1}$$

gives the angle θ at which the X rays are diffracted. This equation can be derived by requiring that the two reflected beams travel a distance equal to a wavelength. Referring to Fig 6.1, this means that, for constructive interference, $AB + BC - AD = n\lambda$, where n is an integer. By simple inspection from the figure, we have $AB = d/\sin\theta$, $BC = d/\sin\theta$ and $AC = 2d/\tan\theta$, while $AD = AC\cos\theta$. In terms of the angle θ the condition for constructive interference is

$$\lambda = AB + BC - AD = \frac{2d}{\sin\theta} - \frac{2d}{\tan\theta}\cos\theta = \frac{2d}{\sin\theta}\left(1 - \cos^2\theta\right), \tag{6.2}$$

which is the same as Eq. (6.1)

Bragg's law tells us in which directions the scattered radiation is diffracted, but it gives no information on the intensities of the reflection. For this, a theory that takes into account the microscopic arrangement of the scatterers in the solid is necessary.

Consider a monochromatic wave polarized along $\hat{\mathbf{x}}$ with complex electric field $\mathbf{E} = E_0\,\hat{\mathbf{x}}\exp[i(\omega_0 t - \mathbf{k}_0 \cdot \mathbf{r})]$ that is incident on an large crystal. The crystal is

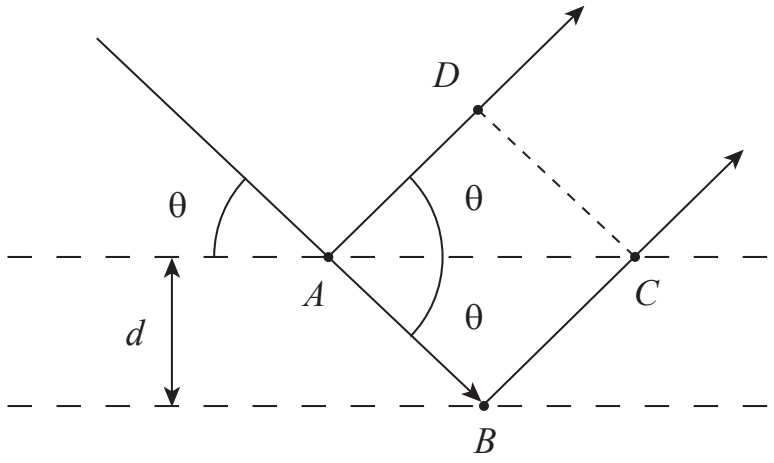

Figure 6.1: Incident radiation reflected by two parallel atomic planes separated by a distance d. Bragg's law dictates at which angle the constructive interference between the scattered waves occurs.

represented by an array of atoms at positions $\{\mathbf{r}_j\}$. Each unit cell in the Bravais lattice can contain more than one atom [25]. As the wave propagates, it is scattered by the electrons in the crystal. The amplitude of the scattered electric field at a distance R, large compared with the interatomic distance, is a superposition of partial waves scattered by each atom [51, 52]

$$E_s = \frac{e^2}{mc^2 R} E_0 e^{i\omega_0 t} \sum_j \sum_n f_n e^{-i[(\mathbf{k}_0 - \mathbf{k}_s)\cdot(\mathbf{r}_j + \mathbf{r}_n)]} \tag{6.3}$$

where $\mathbf{k}_0$ and $\mathbf{k}_s$ are the incident and scattered wavevectors, $\mathbf{r}_j$ is the position of unit cell j, $\mathbf{r}_n$ and f_n are the position and the atomic form factor of atom n in the j-th unit cell, and e^2/mc^2 is the classical electron radius. After some rearrangement, Eq. (6.3) becomes

$$E_s = \frac{e^2}{mc^2 R} E_0 e^{i\omega_0 t} \sum_n f_n e^{-i[(\mathbf{k}_0 - \mathbf{k}_s)\cdot \mathbf{r}_n]} \times \sum_j e^{-i[(\mathbf{k}_0 - \mathbf{k}_s)\cdot \mathbf{r}_j]}. \tag{6.4}$$

The averaged scattered intensity is proportional to the modulus squared of this

expression,

$$I = \frac{c}{8\pi} E_s E_s^* = \left(\frac{e^2}{mc^2 R}\right)^2 |E_0|^2 \qquad \sum_{nm} f_n e^{-i[(\mathbf{k}_0 - \mathbf{k}_s)\cdot(\mathbf{r}_n + \mathbf{r}_m)]} \times \sum_{jl} e^{-i[(\mathbf{k}_0 - \mathbf{k}_s)\cdot(\mathbf{r}_j + \mathbf{r}_l)]}, \tag{6.5}$$

which involves a double sum over the lattice sites. As the crystal contains $\sim 10^{23}$ unit cells, the double sum that comes from the second factor of Eq. (6.4) is basically zero except near

$$\mathbf{k}_0 - \mathbf{k}_s = \mathbf{G}, \tag{6.6}$$

where $\mathbf{G}$ is a wavevector of the reciprocal lattice of the crystal. When Eq (6.6) is satisfied, the intensity in Eq. (6.5) is proportional to N^2, where N is the number of unit cells in the scattering volume. The vectors $\{\mathbf{G}\}$ form a Bravais reciprocal lattice and satisfy

$$e^{i\mathbf{G}\cdot\mathbf{r}_j} = 1 \tag{6.7}$$

for all the vectors $\{\mathbf{r}_j\}$ in the real space lattice. Equation (6.6) is an alternative way to express Bragg's law which determines the direction $\mathbf{k}_s$ of the scattered radiation for a given incident wavevector $\mathbf{k}_0$ and a given set of atomic planes, represented by the vector $\mathbf{G}$. The equivalence between Eq. (6.14) and Eq. (6.6) can be shown as follows. Multiply Eq. (6.6) by $\mathbf{G}$ to obtain

$$\mathbf{k}_0 \cdot \mathbf{G} - \mathbf{k}_s \cdot \mathbf{G} = G^2. \tag{6.8}$$

The dot-product can be expressed in terms of the angle between the diffracting plane and the incident vector $\mathbf{k}_0$. From the diagram in Fig. 6.2 we have $\mathbf{k}_0 \cdot \mathbf{G} = k_0 G \sin\theta_B$ and Eq. (6.8) becomes,

$$2k_0 G \sin\theta_B = G^2,$$

which reduces to Eq. (6.1), since $k_0 = 2\pi/\lambda$, and $d = 2\pi/G = 2\pi/|\mathbf{G}|$.

The first sum in Eq. (6.4) can be identified as the structure factor of the Bragg

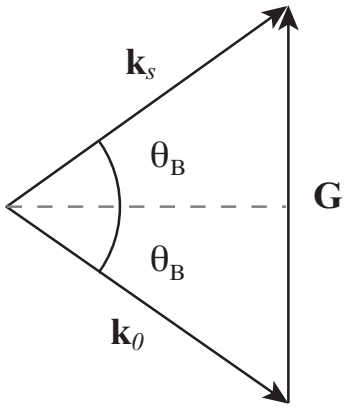

Figure 6.2: Diagram of the vectors in Eq. (6.8).

reflection with wavevector $\mathbf{G}$,

$$F_G = \sum_n f_n e^{i\mathbf{G}\cdot\mathbf{r}_n}, \tag{6.9}$$

where the sum runs over all the vectors in the basis, i.e., all the atoms in the unit cell. The structure factor has information on how the different elements within the unit cell scatter the incident radiation. The total reflected intensity is proportional to $|F_G|^2$, which can be zero in certain cases, depending on the composition and the arrangement of the different elements in the unit cell.

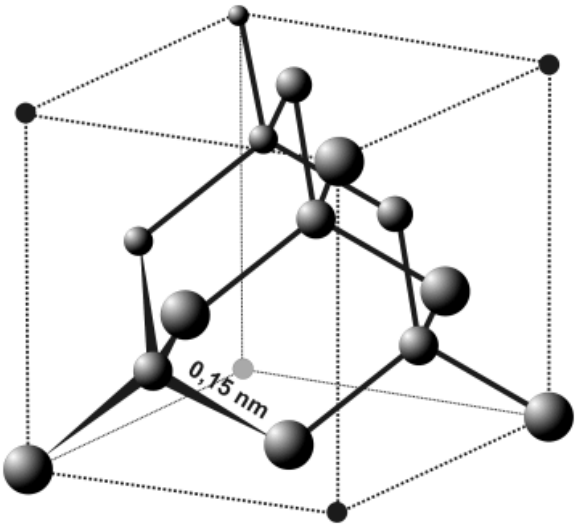

Figure 6.3: Structure of diamond, from [6]. The side of the cube is a.

The zinc-blende structure of the materials studied in this thesis is the two-

element equivalent of the diamond structure shown in Fig 6.3. This structure can be represented by a face-centered cubic (fcc) lattice with a cube of side a. In order to account for all the atoms inside the cube, we add the vectors of the basis

$$\mathbf{r}_1 = \mathbf{0}, \tag{6.10}$$

$$\mathbf{r}_2 = \frac{a}{4}(1\ 1\ 1), \tag{6.11}$$

From Eq. (6.9), the structure factor F_G, given by a sum over all the vectors in the basis is

$$F_{hkl} = f(1 + e^{-i\pi(h+k+l)/2})$$

Table 6.1 shows the first few Bragg peaks for diamond. We have included the angle of the diffracted beam for X-ray photons with energy 10.3 keV, and assuming a lattice constant $a = 5.8687$ Å [7]. Note that for the zinc-blende structure with

$h\,k\,l$	Structure factor	2θ [deg]	Q [Å^{-1}]	d[Å]
1 1 1	1	20.4637	1.8544	3.3883
2 0 0	0	23.6721	2.1413	2.9343
2 2 0	2	33.7245	3.0282	2.0749
3 1 1	1	39.7707	3.5509	1.7695
2 2 2	0	41.6193	3.7088	1.6941
4 0 0	2	48.4378	4.2825	1.4672
3 3 1	1	53.1067	4.6668	1.3464
4 2 0	0	54.5993	4.7880	1.3123
4 2 2	2	60.3204	5.2450	1.1979
3 3 3	1	64.4027	5.5631	1.1294

Table 6.1: Allowed Bragg peaks of the diamond structure. The lattice constant of the cubic unit cell is $a = 5.8687$ Å and the X-ray photon energy is 10.37 keV.

two kinds of atoms, A and B, the geometrical arrangement is the same as for diamond, however, the atomic form factors f_{A} and f_{B} are different and therefore the interference between scattered waves from A and B does not cancel completely, allowing some of the peaks in Table. 6.1.

6.1.1 Perturbation from the perfect crystal

So far, our treatment of X-ray diffraction assumes that the ions rest unperturbed at the lattice sites. However, at finite temperature, the ions undergo thermal motion around their equilibrium positions. These perturbations reduce the intensity of the reflected beam by the well known Debye-Waller factor e^{-2M}, where $M = 8\pi^2\langle u_G^2\rangle(\sin\theta)/\lambda^2$ for a crystal with one atom per unit cell [51]. Here, $\langle u_G^2\rangle = \langle(\mathbf{u}\cdot\mathbf{G})^2\rangle$ is the mean square displacement of the ions around the equilibrium positions projected onto the lattice vector. The excitation of the crystal by an ultrafast laser pulse leaves the ions in the lattice oscillating about their equilibrium positions. The coherent motion of the ions modulates the scattering atomic planes in Eq. (6.14) and, therefore, affects the time-resolved X-ray diffraction pattern.

Consider a single mode with wavevector $\mathbf{q}$ and polarization $\hat{\epsilon}_{q,j}$. For simplicity, we assume a cubic crystal with one atom per unit cell for which the structure factor is given by f. The lattice perturbation modifies the diffracted X-ray intensity, Eq. (6.5). The expression for the intensity of the perturbed diffracted beam is [51],

$$I_1 = \frac{1}{2}\left(\frac{e^2}{mc^2R}\right)^2 |E_0|^2 f^2 e^{-2M} \sum_{g\,j} G_{gj} \sum_{n\,m} \Big[e^{-i[(\mathbf{k}_0-\mathbf{k}_s+\mathbf{q})\cdot(\mathbf{r}_n+\mathbf{r}_m)]} + e^{-i[(\mathbf{k}_0-\mathbf{k}_s-\mathbf{q})\cdot(\mathbf{r}_n+\mathbf{r}_m)]}\Big], \quad (6.12)$$

with

$$G_{g\,j} = \frac{1}{2}[(\mathbf{k}_0-\mathbf{k}_s)\cdot\hat{\epsilon}_{q\,j}]^2\langle a_{q\,j}^2\rangle. \quad (6.13)$$

Here, $\langle a_{q\,j}^2\rangle$ is the mean square amplitude of the phonon mode. The scattered intensity, Eq. (6.12), is negligible except near

$$\mathbf{k}_0 - \mathbf{k}_s = \mathbf{G} + \mathbf{q}. \quad (6.14)$$

This is the same as Eq. (6.6) with the additional term $\mathbf{q}$ from the vibrational mode. This relation can be thought of as the phase matching condition for the incident and

diffracted radiation in the presence of a phonon with wavevector **q**.

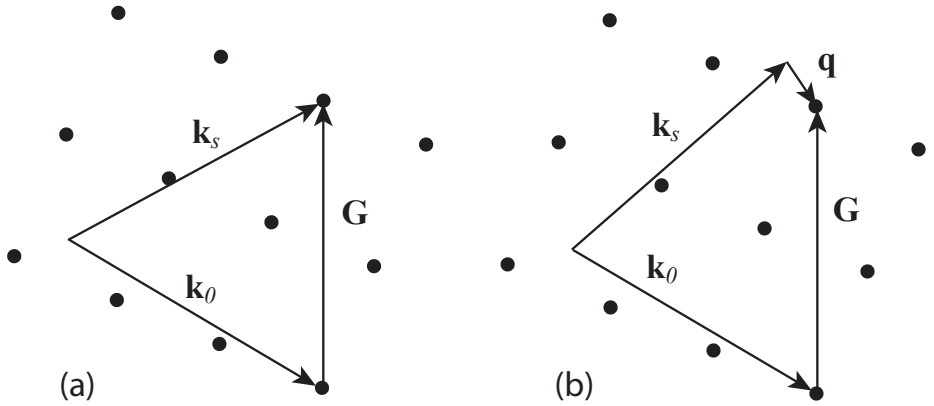

Figure 6.4: Diagram of the vectors in Eqs. (6.6) and (6.14). The dots represent point in the reciprocal lattice. (a) The usual Bragg condition for an unperturbed crystal. (b) Diffraction from a crystal under the presence of a perturbation with wavevector **q**.

The intensity of the diffracted beam perturbed by the phonon, Eq. (6.12), leads to the modified Bragg's condition given by Eq. (6.14). In addition, the superlattice one-dimensional reciprocal space contains lattice vectors that also contribute to the scattering through Eq. (6.14). Those wavevectors are given by multiples of $2\pi/D$, where D is the superlattice period. The two situations are shown schematically in Fig. 6.4. The dots represent the crystal reciprocal space; (a) is a graphical representation of Eq. (6.6): incident radiation with wavevector $\mathbf{k}_0$ is scattered into $\mathbf{k}_s$ by a reciprocal lattice vector **G**. In (b) the incident beam is scattered into $\mathbf{k}_s$ with the help of a phonon of wavevector **q**. The periodic modulation of the structure factor in the superlattice can also give rise to the situation shown in (b). In this sense, the periodic structure can be thought of as a static grating, and the wavevector **q** is provided by the superlattice reciprocal space.

6.2 Dynamical diffraction

The kinematic theory of X-ray diffraction ignores multiple scattering, and assumes that the incident X-ray beam is not depleted as it propagates. In other words, the scattering is well described by the first Born approximation, where the solution is

obtained by assuming the scattered field to be negligible compared with the incident field. However, in a strongly scattering situation where multiple scattering can take place, such as very close to a Bragg reflection or in a big crystal, the diffraction of the scattered field as well as the extinction of the incident beam cannot be neglected. For example, part of the diffracted beam can be scattered back into the incident beam. The dynamical theory of diffraction takes into account multiple scattering. The incident and diffracted beams are coherently coupled and the energy is shared by the two waves. The theory is analogous to the theory of electrons in periodic potentials that gives rise to the band structure in solids [25]. The crystal is represented by a periodic electron density, which yields a periodic dielectric function, and the solutions for the fields are obtained by Fourier analysis. The general problem of solving Maxwell's equations in a perfect crystal is treated in great detail in the paper By Batterman and Cole [53]. In what follows, we introduce the equations of the dynamical theory of diffraction by strained crystals. For simplicity we will consider the situation where the crystal properties vary only in one dimension.

6.2.1 The Takagi-Taupin equation

Takagi [54], and independently, Taupin [55], derived an approximate equation for the diffraction of X rays by strained materials. The equations are valid near the Bragg condition and when the strain is small and varies slowly (i.e. $|\mathbf{q}| \ll |\mathbf{G}|$) so that the eikonal approximation can be justified. The Takagi-Taupin equations in a centro-symmetric crystal are

$$i\tfrac{\lambda}{\pi}\beta_0 \cdot \nabla D_0(r) = \psi_0 D_0(r) + \psi_H D_H(r), \tag{6.15}$$

$$i\tfrac{\lambda}{\pi}\beta_H \cdot \nabla D_H(r) = \psi_0 D_H(r) + \psi_H D_0(r) - \alpha_H D_H(r), \tag{6.16}$$

where λ is the X-ray wavelength in vacuum, $D_{0,H}$ are the electric displacement of the incident and the diffracted fields in the crystal, $\beta_{0,H}$ are the wavevectors inside the

material, and $\alpha_H = -2(\theta - \theta_B)\sin 2\theta_B$ is the offset from the Bragg condition. The quantities $\psi_{0,H}$, are the Fourier components of the periodic electric susceptibility of the crystal which are proportional to the structure factor. Note that inversion symmetry imposes the condition $\psi_{\bar{H}} = \psi_H$, which we have used in Eq. (6.15).

When the material properties vary only in one dimension such as in a multilayer, the Takagi-Taupin equations can be approximated by a one-dimensional differential equation. Since the index of refraction for X-ray radiation is $\simeq 1$, $D \approx E$ and the quantity

$$X = \left| \frac{D_H(\mathbf{r})}{\sqrt{b} D_0(\mathbf{r})} \right|^2 \tag{6.17}$$

is a good approximation to the X-ray reflectivity I/I_0. Here, b is the ratio of the direction cosines of the incident and diffracted beam with respect to the surface normal. With these considerations, the Takagi-Taupin equation in one dimension for the Bragg geometry becomes [56]

$$i\frac{dX}{d\zeta} = (1+ik)X^2 - 2(y+ig)X + (1+ik). \tag{6.18}$$

The parameters are defined as follows: $b = \gamma_0/\gamma_H$, $\gamma_{0,H}$ = direction cosines of the incident and diffracted beam with respect to the inward normal. $\zeta = \pi|\psi'_H|\lambda\sqrt{\gamma_0\gamma_H}z$, z = depth, $\psi_{0,H} = -(e^2/mc^2)(\lambda^2/\pi)(F_{0,H}/V)$, $F_{0,H} = \psi'_{0,H} + i\psi''_{0,H}$ structure factor of the incident and diffracted wave, V volume of the unit cell, $g = (1+b)\psi''_0/2|\psi'_H|\sqrt{b}$, $k = \psi''_H/\psi'_H$, and $y = [(1+b)\psi'_0 - b\alpha_H]/2|\psi'_H|\sqrt{b}$.

The strain, η, is included in α_H,

$$\alpha_H = 2(\theta - \theta_B)\sin 2\theta_B - (c_1\eta_1 + c_2\eta_2), \tag{6.19}$$

where

$$\begin{aligned} c_1 &= 2\sin(2\theta_B)[\cos^2\phi\tan\theta_B - \sin\phi\cos\phi] \\ c_2 &= 2\sin(2\theta_B)[\sin^2\phi\tan\theta_B - \sin\phi\cos\phi], \end{aligned} \tag{6.20}$$

and we have separated the contributions to the strain into the strain parallel, η_1,

and perpendicular, η_2, to the surface normal.

Wie *et. al.* derived an analytical solution to this equation for non-uniform films [57],

$$X(\zeta) = \frac{sX_0 + i(B + CX_0)\tan[s(\zeta - \zeta_0)]}{sX_0 - i(B + CX_0)\tan[s(\zeta - \zeta_0)]}, \tag{6.21}$$

where $B = -(1 + ik)$, $C = y + ig$, $s = (C^2 - B^2)^{1/2}$ and the reflectivity of the sample is given by $X(0)$. The solution, $X(0)$, can be found if we know the reflectivity of the substrate $X_0 = X(\zeta_0)$, which is calculated by inserting $X = X(\zeta_0)$ in Eq. (6.21) and gives

$$X_0 = -\frac{B}{C - \sqrt{C^2 - B^2}}. \tag{6.22}$$

The solution, X_0 can be expressed in terms of the diffraction angle by defining the parameter

$$s = \frac{b\Delta\theta \sin 2\theta + \frac{1}{2}\Gamma F_0(1 - b)}{|P||b|^{1/2}\Gamma\sqrt{F_H F_{\bar{H}}}} \tag{6.23}$$

where $\Delta\theta = \theta - \theta_B$, and P is defined by the polarization, which for σ polarized photons, $P = 1$. The X-ray reflectivity for the symmetric Bragg reflection can be written in terms of s as

$$\frac{I}{I_0} = \left|\frac{E_H}{E_0}\right|^2 = |b|\left[s \pm \sqrt{s^2 - 1}\right]^2 \frac{F_H}{F_{\bar{H}}} \tag{6.24}$$

The two solutions correspond to the α and β branches of the dispersion curves [53]. Eq. (6.24) gives the diffraction curve of the infinite crystal in terms of the angle θ for a symmetric Bragg reflection. A plot of Eq. (6.24) is shown in Fig 6.5 (blue curve). The peak is asymmetric because the β branch suffers stronger absorption than the α branch, which correspond to the two solutions in Eq. (6.24). Also, the width of the peak is related to the Darwin width of the (hkl) reflection and is a measure of the magnitude of the Fourier component of the electron density at the wavevector $\mathbf{G} = (hkl)$.

In Fig. 6.5 we show the calculated reflectivity of the $H = (004)$ symmetric Bragg

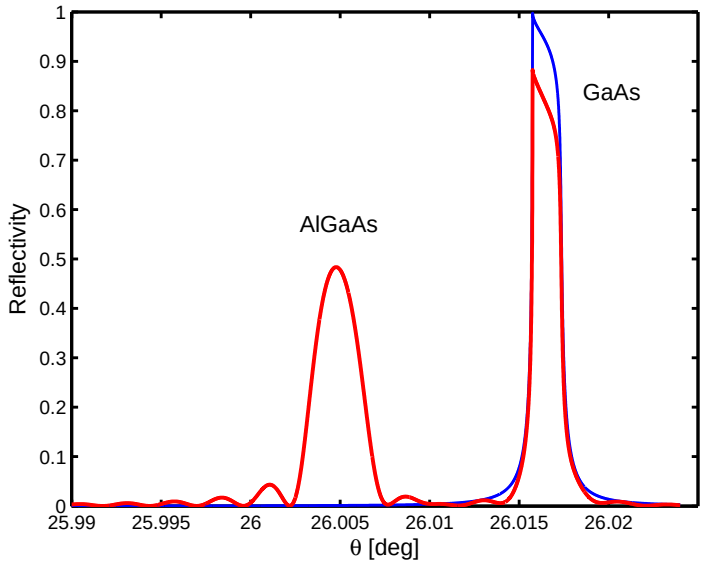

Figure 6.5: X-ray reflectivity of the $H = (004)$ Bragg reflection from a 1.5 μm thick $Al_{0.3}Ga_{0.7}As$ film on a GaAs substrate. The photon energy is 10 keV.

reflection, i.e. $b = -1$, for a 1.5 μm thick $Al_{0.3}Ga_{0.7}As$ film on a GaAs substrate. The photon energy is 10 keV and the lattice constant of the substrate is $a_0 = 5.6534$ Å. The blue curve is the solution for the substrate, X_0.

The finite size of the film produces oscillations in the reflectivity, as seen on the lower side of the AlGaAs peak. Note also that, since the lattice constant of the $Al_{0.3}Ga_{0.7}As$ film is slightly different than the substrate, it can be resolved as a splitting of the diffracted peaks.

6.2.2 X-ray diffraction by a multilayer

The calculations presented above can be easily extended to the case of an arbitrary multilayer. Starting from Eq. (6.21) for each layer in the superlattice, the total reflectivity can be constructed in an iterative manner. Using the same notation as before, Eq. (6.21) is modified to

$$X_j = X(\zeta_j) = \frac{s_j X_{j-1} + i(B_j + C_j X_{j-1}) \tan[s_j(\zeta_j - \zeta_{j-1})]}{s_j X_{j-1} - i(B_j + C_j X_{j-1}) \tan[s_j(\zeta_j - \zeta_{j-1})]}. \tag{6.25}$$

where the parameters refer to the values in each layer and ζ_j is the z-coordinate of layer j.

Most of the X-ray data in this thesis were taken at a symmetric reflection, that is, the incoming and reflected wave form the same angle with the sample normal. This is equivalent to saying that the surface normal of the crystal is parallel to the reciprocal vector $\mathbf{G}$. A *radial* scan of the wavevector $\mathbf{q}$ along the direction of $\mathbf{G}$ is achieved by varying simultaneously the sample, θ, and the detector, 2θ, angle with respect to the incident direction as shown in Fig. 6.6. The situation in the diagram in the inset gives a diffraction peak characteristic of the superlattice, as was discussed earlier in Fig. 6.4. Figure 6.6 shows the scattering geometry for a symmetric Bragg reflection on a superlattice. The vector diagram in the inset represents the Bragg condition, Eq. (6.14), when the superlattice wavevector $q = 2\pi/D$ satisfies the phase matching condition.

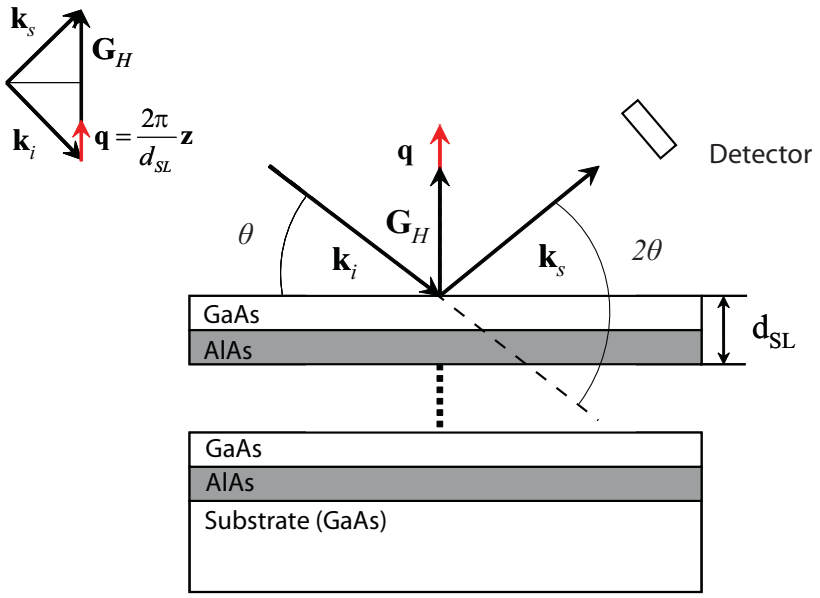

Figure 6.6: Schematic representation of the symmetric Bragg reflection from the superlattice. The inset shows the condition for which the sidebands occur.

The diffraction peaks are labeled by the Miller indices (hkl) of the corresponding diffracting planes. As we mentioned earlier in this Chapter, the structure factor, F_{hkl}, determines the strength of the (hkl) diffraction peak and it depends on the

geometrical arrangement and the type of elements in the unit cell of the Bravais lattice of the crystal. In Fig. 6.7 we show reflectivity results for the (004) Bragg reflection (top trace) for a superlattice of nominally 75 periods of $d_{\mathrm{GaAs}} = 59$ Å and $d_{\mathrm{AlAs}} = 23.5$ Å on top of a GaAs substrate oriented along (001). The X-ray energy was 8 keV. The splitting of the (004) reflection, seen at the center of the curve, is due to the difference in the lattice parameter between the GaAs substrate and the average of the AlAs/GaAs layers. The effective alloy has a slightly larger lattice constant and shows the corresponding (004) Bragg reflection at a lower angle. The sidebands (+1) and (−1) originate from the superlattice periodicity, $q = 2\pi/D$, as explained in Fig. 6.6. In addition, note that there are additional oscillations in the scan, more noticeable between the main peak and the (+1) sideband. The dynamical diffraction extended for superlattice diffraction can be used to identify the origin of these smaller features in the radial scan. Similar features can be seen in the (002) Bragg reflection, as shown in Fig. 6.8. Here we can see a higher order sideband corresponding to (±2). Reflections from (002) planes are forbidden for the diamond structure. The reason why we see the (002) is that the atomic scattering factor of gallium, f_{Ga}, and the corresponding one for arsenic, f_{As}, are very different and thus, the scattered radiation does not completely cancel, resulting in a partially allowed diffraction peak. The oscillation between the main Bragg peak and the superlattice sidebands originate from the scattering of a $\sim$ 70 nm AlGaAs layer deposited between the superlattice and the substrate that acts as an etch stop during the chemical etching process to remove the substrate. These features are well reproduced by the calculations, and the stop layer thickness is close to the nominal value. The fast overall modulation of the curve is due to interference between the radiation from the substrate and that from the superlattice.

From these curves we can extract the period D of the superlattice. From Eq. (6.1), the angle shift $\Delta\theta$ corresponding to a small change in the reciprocal lattice

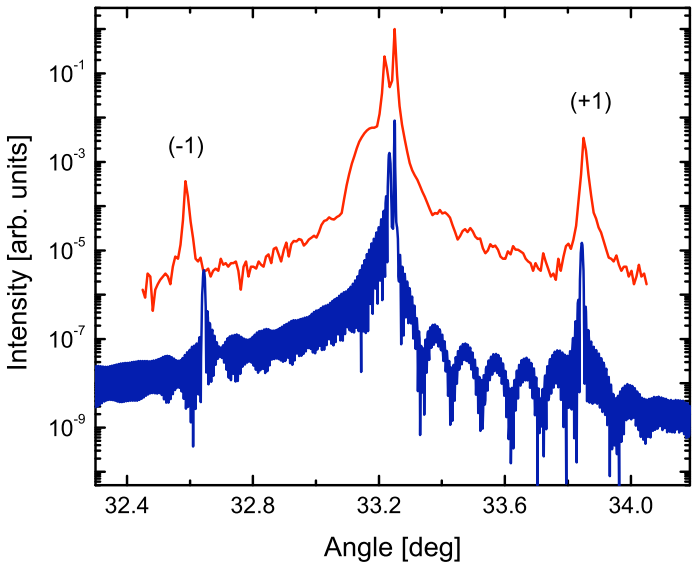

Figure 6.7: Measured (upper) and calculated (lower) rocking curve near the (004) Bragg reflection.

wavevector q is

$$2k_0 \cos\theta_B \Delta\theta = q$$

where θ_B is the Bragg angle of the unperturbed reflection with wavevector G and $q = 2\pi/D \ll G$ is the wavevector of the superlattice. Using $\Delta\theta = 0.6°$ and $\lambda = 1.5498$ Å we obtain for the superlattice period $D = 8.84$ Å, consistent with the value obtained from the optical experiments and the parameters used in the lower curves of Figs. 6.7 and 6.8.

We will next focus on the lattice dynamics studied by time-resolved X-ray diffraction.

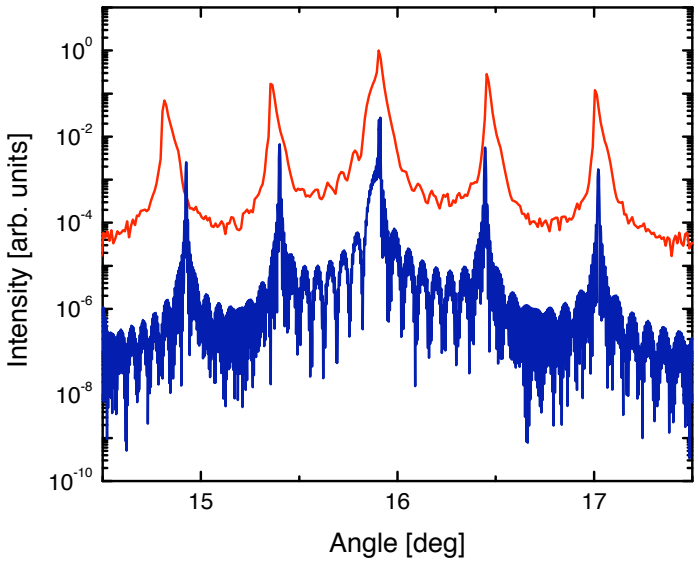

Figure 6.8: Measured (upper) and calculated (lower) rocking curve near the (002) Bragg reflection.

6.3 Time-resolved X-ray experiments

Motivated by the two-superlattice experiments of Chapter V, we devise a scheme to measure the spectrum of folded acoustic phonons excited by an ultrafast laser. A diagram is shown in Fig. 6.9; a short laser pulse excites high frequency folded acoustic phonons in the superlattice, which subsequently leak into the GaAs substrate. The X rays can be made to diffract from either the front surface or the opposite side of the substrate. The X rays probe directly the strain of the acoustic phonons in the substrate.

In the simplest picture, the folded acoustic phonon can be regarded as a moving time-varying grating with spacing equal to the superlattice period, D. Such a grating produces an X-ray diffraction pattern that varies in time and modulates the static rocking curve (Fig. 6.8). In the hypothetical case that we had very short X-ray pulses, we would see the intensity of the superlattice sidebands oscillating up and down in time with the frequency of the phonon [58]. However, our 100 ps-long X-ray pulses give us an average over many acoustic cycles, washing out any time-dependent effect in the rocking curve. In spite of this limitation, we can learn about the

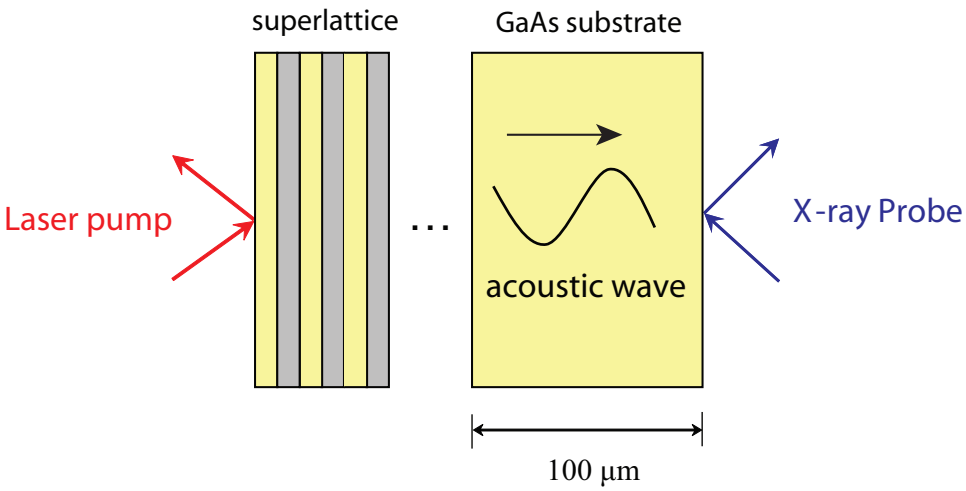

Figure 6.9: Sample and geometry for the X-ray experiment.

propagation of the folded phonons into the substrate and measure the magnitude of the different wavevector components, which is directly related to the frequency spectrum of the laser-excited wave. This is analogous to doing a frequency-domain spectroscopy experiment with the advantage that we can "watch" the coherent excitation as it moves out of the superlattice.

6.3.1 GaAs/AlAs superlattices

The static diffraction pattern for this superlattice was discussed in the previous section (see Figs. 6.7 and 6.8). Now we introduce the results of time-resolved diffraction from this superlattice. The geometry of the experiment is shown in Fig. 6.9. An ultrafast $\sim$ 50 fs laser pulse is absorbed in the superlattice. Following excitation, a 100 ps burst of s-polarized X rays with an energy of 8 keV diffracts from either the superlattice side or the opposite substrate surface. The laser central wavelength was fixed at 800 nm with an energy per pulse of $\sim$ 0.3 mJ polarized in the plane of incidence (p-polarized). We focused the laser beam to maintain an optical fluence of 2 mJ/cm^2. The laser is incident on the sample at a rate of 5 kHz at nearly Brewster's angle to minimize reflection.

Figure 6.10 shows time-resolved scans at an angle $\theta = 29.389°$ on the lower

slope of the GaAs peak (see Fig. 6.7 for reference). In (a) the X rays diffract from the superlattice side and in (b) they diffract from the substrate surface. In these plots, the vertical axis shows the diffracted intensity from the X-ray bunch at a given time after the laser arrives, I_{on}, normalized by the intensity of the same X-ray bunch one revolution around the synchrotron ring before the laser hits the sample, I_{off}. The laser excites carriers in the superlattice which subsequently relax to the bottom of the conduction band leaving behind phonons in the form of heat. This sudden heating of the lattice gradually diffuses until the superlattice reaches thermal equilibrium with the substrate [59]. This temperature diffusion of the deposited heat is the process behind the slowly decaying signal in Fig. 6.10 (a). On top of this, as we discussed in Chapters III and V, the absorption of the laser pulse generates strain in the superlattice that propagates into the substrate. The strain comprises excitations of different folded acoustic branches, in particular, on the lower side of the lowest branch. The peak right after $t = 0$, superimposed on top of the slow temperature decay, is the acoustic wave excited by the laser in the superlattice. Because our X-ray pulses are ~ 100 ps long, we can only resolve time events slower than the pulse duration. This peak is what we called the "Brillouin" component of the signal in previous chapters. After ~ 40 ns the acoustic wave reaches the superlattice again after reflecting from the substrate surface. Since the strain flips sign upon reflection from a free surface, the echo at 40 ns appears with the opposite sign, i.e., there is a decrease in the relative intensity. When the probe reflects from the substrate side we obtain the trace shown in Fig. 6.10 (b). This trace shows the strain pulse generated form the superlattice arriving at the opposite surface of the substrate after 20 ns. Note that, consistent with the argument given above, the strain appears as an increase in the recorded signal.

The diffraction data taken on the substrate surface at the wavevector $q = 2\pi/D$, (not shown) where the folded phonons are expected, shows no signature of folded

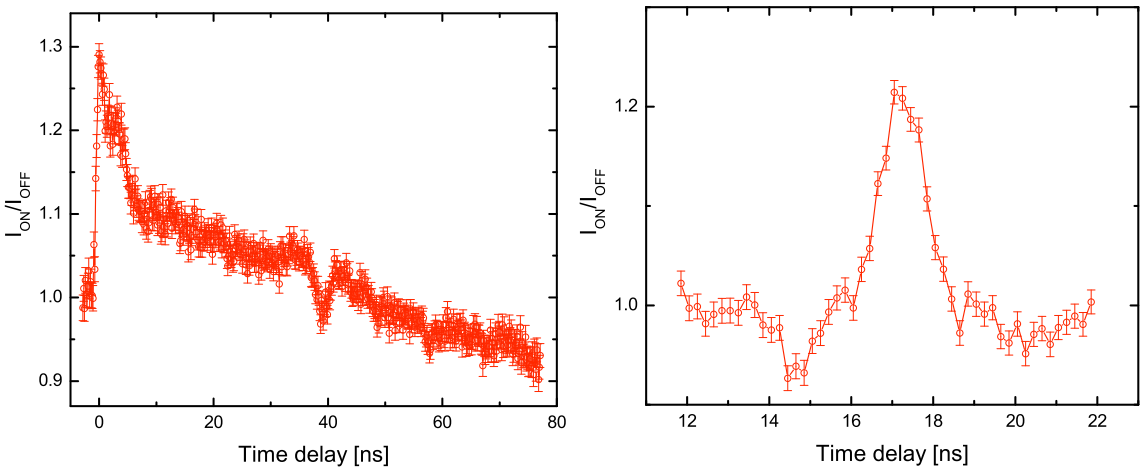

Figure 6.10: Diffraction signal from the propagating strain.

phonons, indicating that they decay too fast and do not reach the opposite surface. Anharmonic decay can be important for phonon modes of such high frequencies. The Debye temperature of GaAs at 300 K is $\Theta_D = 360$ K, which means that a significant fraction of the phonon modes are populated at room temperature leading to a high rate of decay. We will come back to the question of anharmonic decay when we discuss the results at lower temperatures in the following sub-section. The advantage of reducing the temperature is twofold: the lattice temperature is lowered, reducing the anharmonic decay, but also laser damage is avoided by cooling down.

An issue that arises when cooling down is that the band-gap of the GaAs/AlAs superlattice at 10 K is above the laser photon energy, impeding the excitation of the superlattice with 800 nm pulses. Other materials that have a lower band gap at low temperature have to be used for the superlattice compounds. This is the scope of the next section.

6.3.2 $Ga_xIn_{1-x}As/Al_xIn_{1-x}As$ superlattices

The sample studied in this section is a 60-period $Ga_{0.47}In_{0.53}As/Al_{0.48}In_{0.52}As$ superlattice grown on an InP substrate. The layer thicknesses are $d_{\mathrm{GaInAs}} = 12$ nm and $d_{\mathrm{AlInAs}} = 4.4$ nm. The InP substrate and the $Ga_{0.47}In_{0.53}As/Al_{0.48}In_{0.52}As$ alloys

crystallize in the zinc-blende structure, as most III-V compounds. In order to avoid hard X-ray fluorescence from the elements in the sample, the X-ray photon energy was restricted to energies below the Ga K absorption edge at 10.37 keV.

A static rocking curve for this superlattice is shown in Fig. 6.11. The curves resemble the results for the GaAs/AlAs superlattice discussed above, exhibiting a superlattice pattern, indicated by the zeroth order, labeled (0), and the (-1) and $(+1)$ sidebands, superimposed with the substrate reflection, InP. The reason for the observation of the substrate peak is the rather long absorption length of the X rays, ~ 6 μm, compared to the length of the structure. Note also that the splitting between the InP and the 0-order peak of the superlattice is larger than in the GaAs/AlAs case (Fig. 6.7), indicative of a greater mismatch between the lattice parameters of the $Ga_{0.47}In_{0.53}As/Al_{0.48}In_{0.52}As$ superlattice and the InP substrate. As we will show later, this can be used to our advantage to resolve the high-wavevector phonons in the substrate.

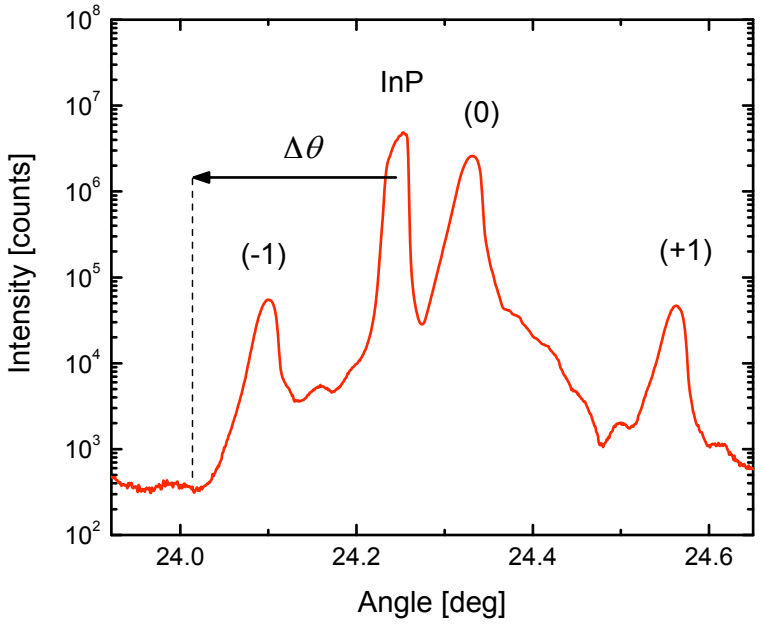

Figure 6.11: Rocking curve of the InP superlattice near the (004) symmetric Bragg reflection. Sidebands labeled (0), (± 1), (± 2) correspond to the superlattice, and the peak labeled InP is the (004) substrate reflection.

The time-resolved experiments on this sample were performed in the same

geometry as for the GaAs sample: The laser excites acoustic waves in the superlattice, and the X rays diffract from the back surface (Fig. 6.9). The data presented in the following discussion were taken at $T = 10$ K using a commercial displex system customized for optical/X-rays experiments.

Figure 6.12 shows the arrival of the acoustic pulse at the surface opposite to the superlattice (the equivalent of Fig. 6.10 (b) for the sample on InP substrate). In this figure we present three consecutive acoustic pulses, that correspond to the first arrival at the InP surface and the second and third echoes. These are shown superimposed on a common time axis in order to compare the shape of the wave-packet as the excitation bounces back and forth in the sample. We observe up to a total of four echoes reaching the substrate surface, after traversing the 300 μm InP substrate seven times.

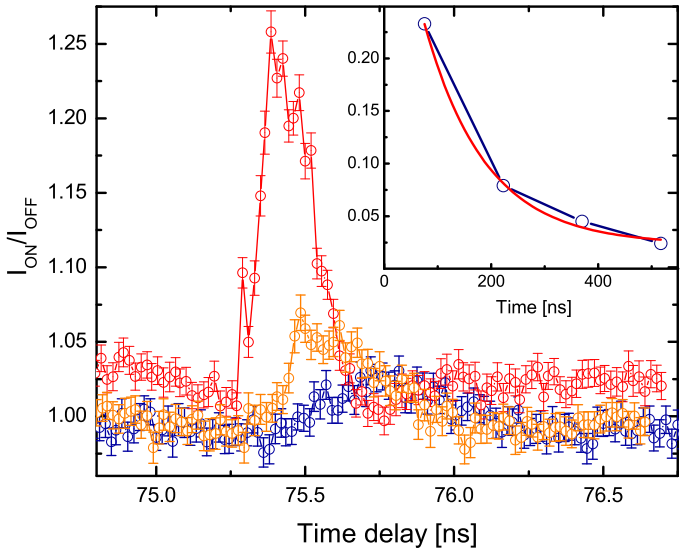

Figure 6.12: Time scans at $\theta = 24.1964°$, below the (0) peak of the GaInAs/AlInAs superlattice. The curve show the first arrival of the acoustic pulse at the substrate surface and the first and second echoes. The inset shows the amplitude of the different acoustic pulses as a function of arrival time. The solid line is an exponential fit.

The inset of Fig. 6.12 shows the amplitude of the successive acoustic pulses as a

function of the arrival time superimposed on a fit to $e^{-t/\tau}$. The decay of $\tau = 115$ ns is much faster than we expected. The relaxation rate for long wavelength acoustic phonons in a crystal with cubic symmetry scales with temperature as [60]

$$\gamma \propto T^3 \omega^2, \tag{6.26}$$

provided that the temperature is well below the Debye temperature, so that the only significant contribution from the anharmonic potential is the cubic term $\sim u^3$ [60]. To understand this point, consider the superlattice as an effective bulk material; the absorption of the laser generates a sound wave peaked at the frequency $\nu = v/\xi = 18$ GHz, where $\xi = 1/250$ nm is the absorption length of the laser in the superlattice and $v = 4580$ m/s is the speed of sound [12]. Using $\tau = 115$ ns, and assuming that the scaling (6.26) still holds at the folded phonon frequencies, we obtain for the 0.25 THz folded phonons a decay $\tau_{\mathrm{FP}} = 740$ ps or, equivalently, a mean free path $l_{\mathrm{FP}} = 3.3$ μm. This decay time is long enough for the folded phonons to leak out of the superlattice and reach the substrate, but not long enough for these modes to propagate across the ~ 300 μm-thick InP substrate.

Folded phonons have wavelengths equal to multiples of the period of the superlattice. This means that the small contribution to the X-ray diffraction from folded acoustic modes should appear superimposed on the large static superlattice sidebands, obscuring any time-dependent effects. However, the acoustic wave that leaks into the substrate has a different wavevector due to the difference in the speeds of sound. Furthermore, the diffraction angle shifts in the substrate are referenced relative to the InP peak instead of the (0) superlattice peak, as shown in Fig. 6.11. The folded phonon contribution in the substrate is expected at an angle $\theta_{\mathrm{InP}}(004) \pm \Delta\theta$, where $\theta_{\mathrm{InP}}(004)$ is the angle for the (004) reflection from the InP and $\Delta\theta$ is approximately the shift from (0) to the (-1) sideband (neglecting the small mismatch in the speed of sound). This is indicated in Fig. 6.11 by a horizontal

arrow. The splitting of the InP and the (0) peak gives us a clear way to discern the effect of the high frequency acoustic phonon leaking into the substrate from the static superlattice sidebands.

Material	v_s [m/s]	ρ [g/cm^3]	Thickness
$Al_{0.48}In_{0.52}As$	4703	4.758	12 nm
$Ga_{0.47}In_{0.53}As$	4253	5.55	4.4 nm
InP	4580	4.81	375 μm

Table 6.2: The constituents of the AlInAs/GaInAs superlattice grown on InP. The material parameters are from [7]. The thicknesses are nominal values.

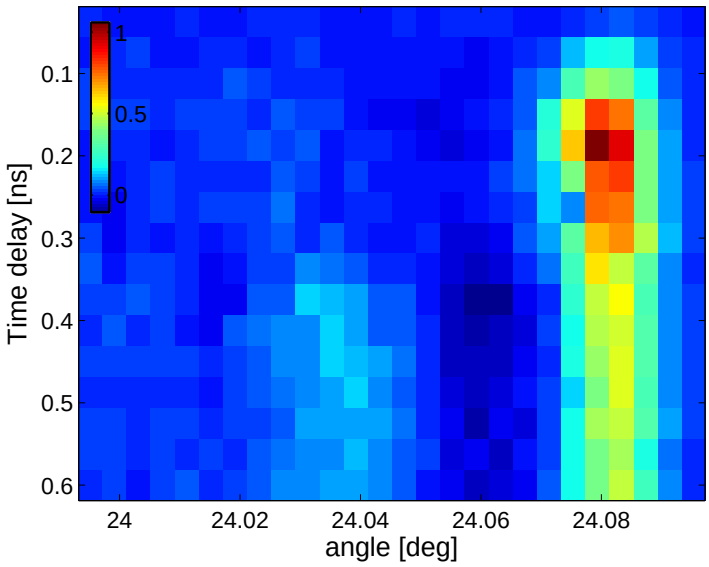

Figure 6.13: Time resolved diffraction curve near $\theta_{\mathrm{InP}} - \Delta\theta$.

Figure 6.13 shows a time-resolved rocking curve on the lower side of the (-1) sideband, around $\theta_{\mathrm{InP}} - \Delta\theta$ where the folded phonon signature is expected. The color bar is a measure of the diffracted intensity induced by the laser relative to the unperturbed signal, $I_{\mathrm{ON}}/I_{\mathrm{OFF}}$. At $t = 0.1$ ns, the laser pulse is absorbed in the superlattice. The absorption length for light of 800 nm wavelength is ~ 250 nm for a $Ga_{0.47}In_{0.53}As$ alloy [61], so that most of the laser energy is absorbed in the 1 μm-thick superlattice. On the other hand, the InP substrate is not perturbed until

the energy has had enough time to propagate into the substrate. We assume that instantaneous laser heating produces a thermal expansion that shifts the superlattice curve towards lower angles, indicating an increase in the lattice constant. The prominent feature at $\theta \simeq 24.08°$ on the right side of Fig. 6.13 is due to the shift of the (-1) sideband from the thermal expansion of the superlattice.

At a delay of $\Delta t = 200$ ps after the laser absorption, a much weaker signal appears at $\theta \simeq 24.04°$ which is the angle of the high-wavevector phonon-modes that originate from the folded phonons leaking into the substrate. Note that this time delay corresponds roughly to the transit time of an acoustic pulse through the superlattice $\Delta t = L/v_{\mathrm{SL}} = 225$ ps, with L the length and v_{SL} the speed of sound of the superlattice.

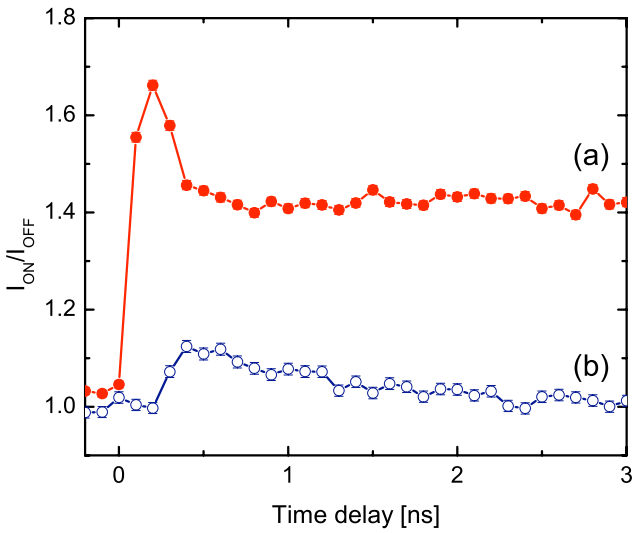

Figure 6.14: Time scans at different angles near the (-1) rocking curve, (a) $\theta = 24.084°$ below the (-1) sideband and, (b) $\theta = 24.03°$ at the folded phonon angle.

Figure 6.14 shows time scans for two fixed angles. The top curve (a) is at an angle $\theta = 24.084°$, very close to the (-1) sideband, and the lower curve (b) at $\theta = \theta_{\mathrm{InP}} - \Delta = 24.03°$. Again, there is a time-delay of ~ 200 ps between the onset of the two signals that corresponds to the transit time of the acoustic wave

through the 980 nm-thick superlattice. Note the different decay time in these two curves; trace (a) decays over tens of nanoseconds, while (b) decays in 0.9 ns. We attribute the main contribution to the signal in (a) to the thermal expansion of the superlattice upon absorption of the laser pulse. This explains the long relaxation time, since the thermalization back to equilibrium is a very slow process that takes tens of nanoseconds [59]. On top of the thermal component in (a), we observe a sharp feature at early times, $t < 0.4$ ns, due to the coherent strain generated in the superlattice. This strain wave only shifts the (-1) sideband while it remains in the superlattice. The time duration of the sharp peak in (a) is given by a convolution of our experimental resolution (the X-ray pulse duration) with the travel time of the acoustic wave through the superlattice, of the order of ~ 220 ps.

In contrast with the slow thermal diffusion of tens of nanoseconds seen in Fig. 6.14 (a), the high-frequency phonons, traveling at the speed of sound, cross the 6 μm X-ray absorption length in the InP in only 1.3 ns. This explains the decay of the signal in (b). According to this interpretation, it takes ~ 225 ps for the folded phonons to reach the substrate and this is the reason why the onset seen in (b) is delayed from the onset in (a). In addition, the decay of (b) is consistent with an acoustic wave traveling at the speed of sound in the substrate.

Figure 6.15 shows angle-resolved scans taken from Fig 6.13, for three different time delays $\Delta t = 0$, 75, 225, and 263 ps. We assume that the laser pulse arrives at $\Delta t = 0$ ps, where we observe a shift of the (-1) sideband towards lower angles, giving a prominent increase in the $I_{\rm on}/I_{\rm off}$ signal at $\theta = 24.08°$. At $\Delta t = 75$ ps, this peak reaches its maximum value $I_{\rm on}/I_{\rm off} = 2$. At a delay of 225 ps the main peak has decreased and the curve exhibits the onset of a small peak at $\theta = 24.04°$ and a dip at $\theta = 24.02°$ and $\theta = 24.06°$, which become very clear at $\Delta t = 263$ ps. These features, which are delayed from the laser arrival by ~ 220 ps, appear at the expected angle for the folded phonons propagating in the substrate.

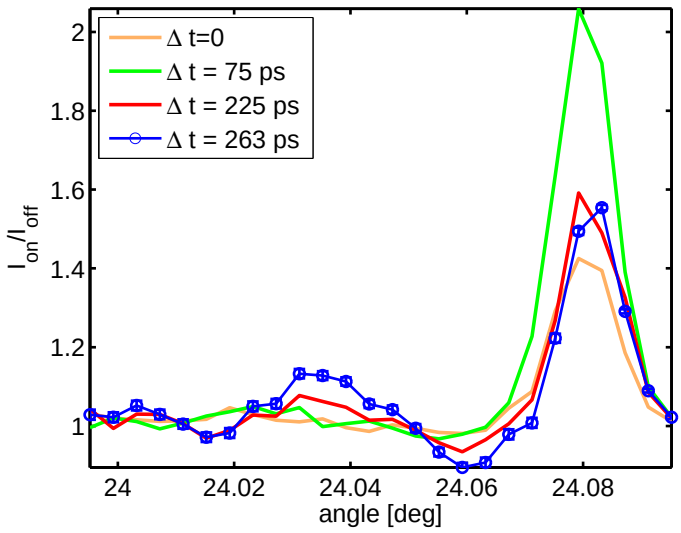

Figure 6.15: Four different time slices of the data in Fig. 6.13: $\Delta t = 0$ ps, 75 ps, 225 ps, and 263 ps. The peak that appears after ~ 220 ps at $\theta = 24.04°$.

Figure 6.16 shows the laser-induced effect on the rocking curve (red traces, top panel) at a time-delay of $\Delta t = 220$ ps, taken from Fig. 6.13. For easier comparison with the dispersion relation, we have converted the diffraction angles to the corresponding wavevector transfer, q, measured from the InP Bragg peak. The blue curve in the top panel is the static rocking curve, showing the InP, (0), ($\pm$1), and ($-$2) superlattice peaks. Note that the wavevector transfer q is measured with respect to the InP Bragg peak. The lower panel shows the dispersion relation of the acoustic phonons in the superlattice (blue) in the extended zone scheme. We have shifted the origin of the x-axis to align with the (0) superlattice peak and we have adjusted the period D to match the wavevectors $q = \pm 2\pi/D$ with the superlattice peaks in the blue trace. The red curve in the lower panel is the dispersion relation of the acoustic waves in the InP substrate, $\nu = v_{\mathrm{InP}} q$. The folded phonons from the superlattice leak into the substrate and acquire the wavevectors indicated by the circles in the lower panel. The peaks observed in the $I_{\mathrm{on}}/I_{\mathrm{off}}$ signal, indicated with vertical arrows in the top panel, align with the expected wavevectors in the substrate.

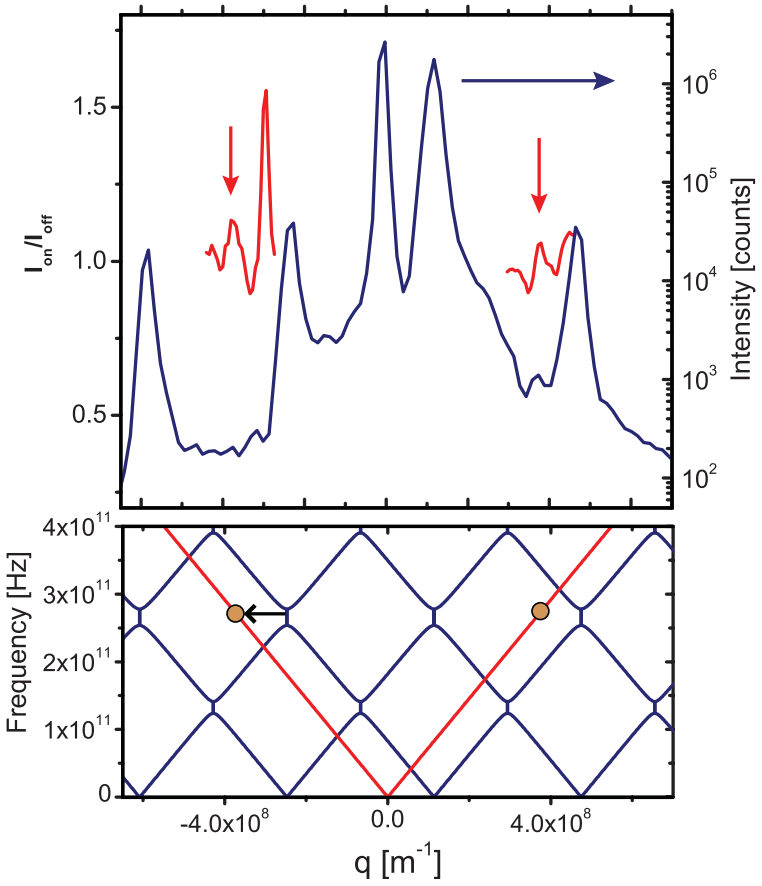

Figure 6.16: Top panel: $I_{\rm on}/I_{\rm off}$ signal near the (-1) and the $(+1)$ sideband at $\Delta t = 220$ ps after time-zero (red traces). The blue curve is the static diffraction pattern showing the InP, (0), (± 1), and (-2) peaks. Bottom panel: calculated acoustic dispersion in the superlattice (blue curve) aligned with the (0) peak, and dispersion relation of the acoustic waves in the InP substrate (red curve). The dots indicate the position of the high-wavevector phonons from the superlattice in the substrate.

We have performed dynamical diffraction calculations taking into account the time-dependent strain, $\eta(z,t)$. These calculations combine the simulations of the acoustic wave equation introduced at the end of Chapter V, with the dynamical diffraction theory presented earlier in this Chapter. The simulations require to calculate first the strain, $\eta(z,t)$, which enters in Eq. (6.19), and then iterate Eq. (6.25) to obtain the time-dependence of the diffraction pattern. As in Fig. 5.9, the initial folded phonon from the superlattice is assumed to have a gaussian profile modulated by the function $K(z)$ that gives rise to the high frequency components. Although this, again, might not seem very physical, the conclusions drawn from

these simulations do not depend on the specific shape of the initial strain as long as it is modulated by the function $K(z)$. Using a smooth envelope like a gaussian avoids numerical instabilities that occur when using finite-differences to approximate functions that have sharp edges or discontinuous derivatives [62]. The superlattice structure consists of 60 periods of $In_{0.53}Ga_{0.47}As$ and $In_{0.52}Al_{0.48}As$ with thicknesses $d_1 = 12$ nm and $d_2 = 4.4$ nm respectively, on a (001)-oriented InP substrate represented by a 2000 nm-thick layer on top of another semi-infinite InP layer.

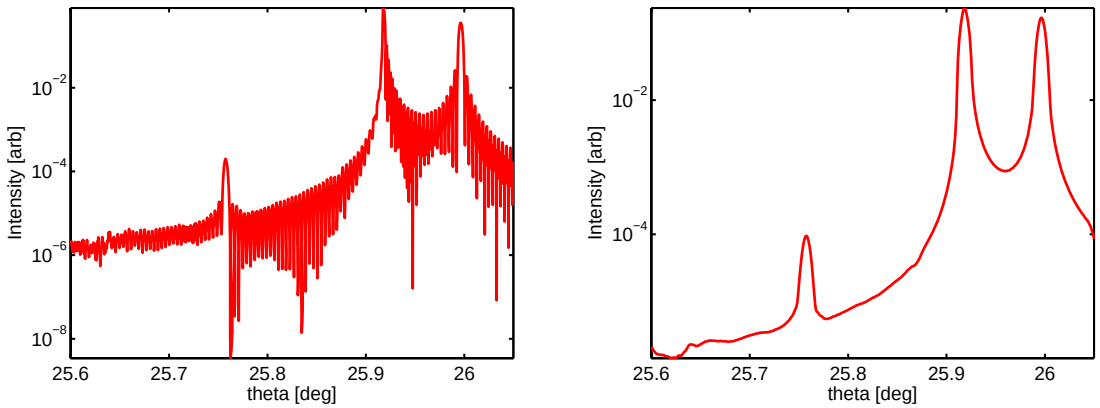

Figure 6.17: (a) Calculated diffraction curve near the (004) reflection for the GaInAs/AlInAs superlattice on an InP substrate; (b) same curve low-pass filtered to match the widths of the peaks to the experiment.

The static diffraction pattern for this structure is shown in Fig. 6.17 (a). The peaks shown correspond to the Bragg reflections from the InP, the (0) and the (-1) diffraction orders of the superlattice, as observed in the experimental data in Fig. 6.11. The lattice parameter mismatch between the substrate and the superlattice was adjusted to match the angle splitting between the InP peak and the (0) order obtained from the experiment. As expected, the simulation predicts a high-frequency modulation of the diffraction pattern due to the finite size of the superlattice, as discussed in section 6.2.2. We cannot resolve such fine structure in our experiment, however, the experimental resolution is much finer than the widths of the features in Fig. 6.11, suggesting that the peaks are broadened significantly from the calculated

values. The origin of this broadening is likely to be due to strain from the way the sample was mounted. For easier comparison with the measured curves, we low-pass filter the calculated results to eliminate the high-frequency modulation. The resulting trace is shown in Fig. 6.17 (b).

The main question we want to answer with this simulation is whether the observed features originate from the shift of the superlattice sideband (induced by the low frequency strain in the superlattice), or from the propagation of the folded phonons into the substrate. To answer this question, we calculated the diffraction curves under two different conditions: First, with the initial strain containing the factor $K(z)$ that gives the folded phonons and, second, with the initial condition given by the gaussian envelope without the factor $K(z)$. The latter gives only the slowly-varying part of the time evolution. Figure 6.18 summarizes the results. The curves are calculated near the (-1) sideband and with delays of up to 700 ps, which are long enough for the traveling waves to leave the superlattice. In Fig. 6.18 (a), we show the time resolved pattern for the gaussian envelope without the factor $K(z)$ in a broad region of angles that contains the InP, (0) and (-1) peaks. These peaks shift in time as the strain propagates into the substrate. Since a positive strain means an expansion of the crystal, the (0) peak shifts to higher angles near $\Delta t = 150$ ps, when the positive part of the strain leaves the superlattice. Similarly, a shoulder in the lower side of the InP peak appears as the tensile component of the strain reaches the substrate. The unperturbed solution of the substrate, X_0, is not affected by the propagating strain, and is superimposed on top of the shifted InP peak from the 2000 nm layer. This gives the apparent broadening of the substrate peak in (a), instead of the expected shift to lower angles induced by the tensile strain. Figure 6.18 (b) is an expanded view of the same calculation near the (-1) sideband showing the shift of the sideband due to the acoustic strain in the superlattice. Note that the (-1) peak follows the shift of the (0) sideband

shown in (a). Figure 6.18 (c) is the same as (b) except that the initial strain is composed of the gaussian envelope and folded phonons with period D (calculated including the factor $K(z)$). Since the envelope of the strain is the same as in (b), the time-evolution of the (-1) sideband resembles that of Fig. 6.18 (b), however, its intensity is modulated in time by the high frequency of the folded phonons, as shown in more detail in Fig. 6.18 (d). This oscillation of the sideband from folded phonons should in principle be observable using sub-picosecond laser-based X-ray pulses, or with a streak camera [63]. However, our current pulse duration of 100 ps at the APS is a limitation for this goal.

Figure 6.19 shows the region near the high wavevector phonons at $\theta_{\mathrm{InP}} - \Delta\theta$ in the InP substrate. The strong feature on the high angle side is the (-1) sideband of the superlattice, as in Fig. 6.13. The delayed onset of the high-frequency phonons after ~ 200 ps is evident at $\theta \approx 25.68^{\circ}$ in (a). For comparison, we shown in Fig 6.19 (b) the same region for the acoustic strain without the folded phonon function $K(z)$. Clearly in this case, the strain cannot produce a feature at $\theta_{\mathrm{InP}} - \Delta\theta$ because it has no Fourier components at the corresponding wavevector for this angle. This confirms that the features observed at $\theta_{\mathrm{InP}} - \Delta\theta$ are due to folded phonons with wavevector $q = 2\pi/D$ in the substrate.

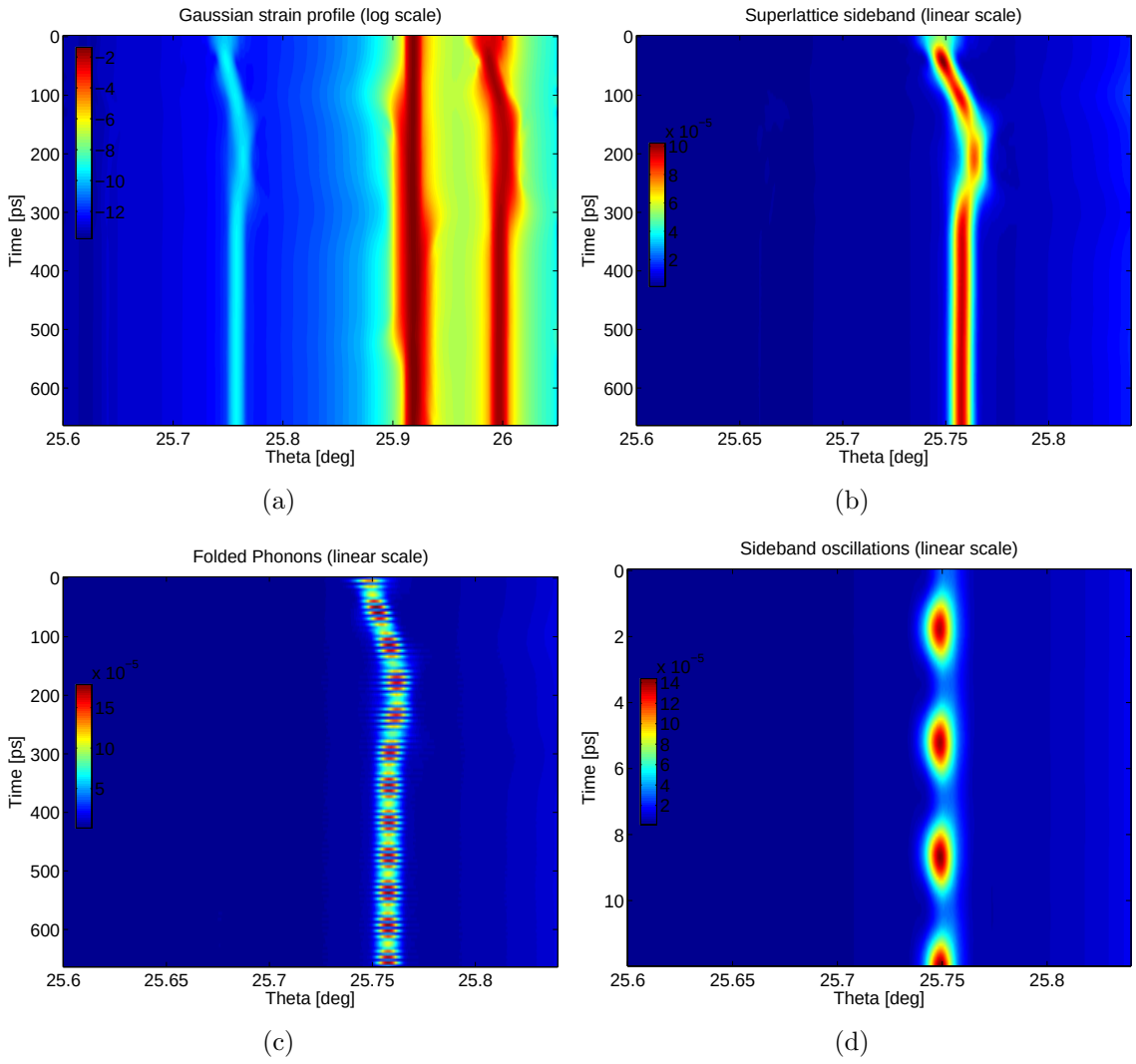

Figure 6.18: Calculated time-resolved diffraction pattern for the InGaAs/InAlAs superlattice. (a) Calculation using a gaussian-shaped initial strain (logarithmic scale). The (-1), InP and (0) peaks can be seen shifting with time; (b) view of the same results near the (-1) sideband; (c) the (-1) sideband evolution when the strain is modulated by the function $K(z)$ representing folded phonons; (d) calculations with finer time resolution of the same region that show the oscillation of the sideband induced by the folded phonons.

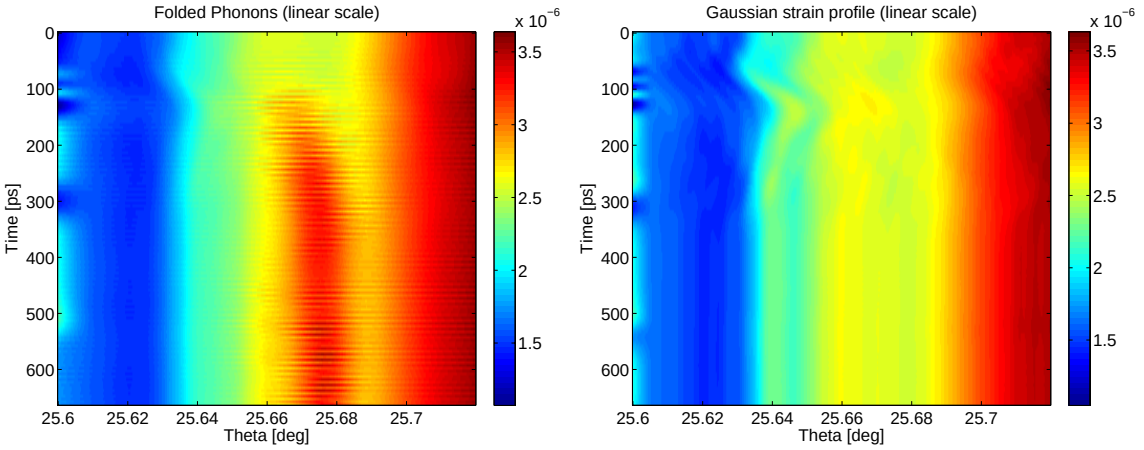

(a) (b)

Figure 6.19: Time resolved diffraction below the (-1) sideband. (a) Calculation including the folded phonons from the superlattice, and (b) the same calculation for the gaussian shaped strain pulse.

CHAPTER VII

CONCLUSIONS AND FUTURE WORK

In this thesis, I presented time-resolved studies of folded acoustic phonons generated from semiconductor superlattices. The first of the two experiments performed uses ultrashort laser pulses to study the generation mechanism and the propagation of folded phonons in the time domain. In this part of the work, I developed a novel scheme to study folded phonons that uses two superlattices as emitter and receiver that are separated by up to 1.2 μm of GaAs. By separating the generation region from the detection region, the contributions to the differential reflectivity from the acoustic excitation can be isolated from electronic and thermal effects. This approach also has the benefit of being frequency-sensitive, and allows one to estimate the bandwidth of the excitations reaching the receiver. Results show that modes that escape the superlattice propagate at the speed of sound and travel without attenuation through 1.2 μm of GaAs at 80 K. In contrast, modes with frequencies near the acoustic gaps exhibit an unusually long lifetime. These modes have the peculiar behavior of avoiding the surfaces of the periodic structure, as confirmed by calculations of the eigenmodes of a finite superlattice. These observations are also supported by a fully numerical solution of the time-dependent wave equation, which shows that at long times what remains in the superlattice is only the mode at the Brillouin zone center.

Because of the long wavelength of light, optical probes can only couple to excitations near the zone-center of the crystalline Brillouin zone. On the other hand,

the wavelength of X-ray radiation is of the order of the nearest neighbor distances in solids, and can in principle couple with excitations of any wavevector in the crystal. In the second part of this thesis, I showed time-resolved X-ray diffraction experiments to study the folded phonons from the superlattice after they have reached the substrate. The phonon dispersion relation in the substrate is that of a bulk compound and does not exhibit acoustic branch folding. Therefore, the propagation of the high-frequency folded phonons into the substrate leads to high-wavevector excitations that can be studied by X-ray diffraction. Experimental results show evidence of such high-wavevector acoustic phonons leaving the superlattice at the speed of sound. Using the strain calculations from the continuum model developed in the first part of this work, and using the theory of dynamical diffraction of X rays, it is possible to simulate the time dependence of the diffraction pattern which corroborates the experimental results.

With this experiment, I demonstrated for the first time that the technique of ultrafast X-ray diffraction is sensitive to excitations of high-wavevector in the substrate produced by the zone-folding of the acoustic branches. The sensitivity to excitations away from the Brillouin zone-center is unattainable with most scattering techniques and holds promise for studies of ultrafast processes in solids that are inaccessible with optical probes. Improvements in the time resolution will allow simultaneous frequency and wavevector measurements to better understand the lattice dynamics. In particular, this results hold promise for time-resolved studies of solids by monitoring the diffuse X-ray scattering throughout the full Brillouin zone.

APPENDIX A

FDTD METHOD FOR THE WAVE EQUATION

Here we derive a set of discrete equations for the numerical solution of Eq. (3.2) by the method of finite difference in time domain (FDTD) [62]. The homogeneous wave equation is

$$\rho(x)\frac{\partial^2 u(x,t)}{\partial t^2} = \frac{\partial}{\partial x}\left[\frac{\partial u(x,t)}{\partial x}\right], \tag{A.1}$$

where $u(x,t)$ is the atomic displacement varying in one spatial dimension and in time, and $\rho(x)$ and $C(x)$ are the position dependent density and elastic stiffness constant, respectively. We define a uniform mesh of points, $x_j = \{x_1, \ldots, x_J\}$, and $t_k = \{t_1, \ldots, t_K\}$, that span the integration domain where we want to obtain the solution. The derivatives at an arbitrary point (x_j, t_k), can be approximated by the finite differences,

$$\frac{\partial u(x_j,t_k)}{\partial x} = \frac{u(x_j+\Delta x, t_k) - u(x_j,t_k)}{\Delta x} \tag{A.2}$$

and

$$\frac{\partial u(x_j,t_k)}{\partial t} = \frac{u(x_j,t_k+\Delta t) - u(x_j,t_k)}{\Delta t}, \tag{A.3}$$

with similar expressions for the spatial derivatives of the other quantities. If we write $u_{j,k} = u(x_j,t_k) = u(j\Delta x, k\Delta t)$, $\rho_j = \rho(x_j)$, $C_j = C(x_j)$ and define the parameter $v = \Delta x/\Delta t$, using the approximations for the derivatives, Eq. (A.1) becomes

$$\begin{aligned}\rho_j v^2\left[u_{j,k+1} - 2u_{j,k} + u_{j,k-1}\right] = \left(C_{j+1} - C_j\right)\left(u_{j+1,k} - u_{j,k}\right) + \\ C_j\left[u_{j+1,k} - 2u_{j,k} + u_{j-1,k}\right],\end{aligned} \tag{A.4}$$

which yields,

$$u_{j,k+1} = \left[\frac{C_{j+1} + C_j}{\rho_j v^2} - 2\right] u_{j,k} + \frac{C_{j+1}}{\rho_j v^2} u_{j+1,k} + \frac{C_j}{\rho_j v^2} u_{j-1,k} - u_{j,k-1}. \tag{A.5}$$

This equation gives the solution at time t_{k+1} if we know the solution at times t_k and t_{k-1}. By iterating Eq. (A.5) one can construct the solution for all times if the first two values $u(x_j, t_0)$ and $u(x_j, t_1)$, are known.

The initial conditions are handled by setting the initial strain and its time derivative,

$$\eta(x, t_0) = \frac{\partial u(x, t_0)}{\partial x} = \eta_0(x) \tag{A.6}$$

and

$$\frac{\partial \eta(x, t_0)}{\partial t} = \frac{\partial^2 u(x, t_0)}{\partial x \partial t} = 0, \tag{A.7}$$

which are known functions of position.

Note that the solution, Eq. (A.5), is valid only inside the integration domain $(x_1, \ldots, x_{J-1})$. The condition at the $x = 0$ boundary is given by the free surface equation

$$\frac{\partial u(x_0, t)}{\partial x} = 0. \tag{A.8}$$

This condition can be represented numerically by extending the integration region to points beyond the domain, $u(x_0, t_k)$, such that

$$u_{0,k} = u_{1,k}, \tag{A.9}$$

which satisfies Eq. (A.8).

In order to represent a semi-infinite substrate we have to force the wave to leave the integration domain by forcing the solution at $x = L$ to be a traveling wave in the $+x$ direction. That is, in terms of the quantities defined above,

$$u_{J,l} = u_{J-1,l-1}. \tag{A.10}$$

BIBLIOGRAPHY

[1] A. Ducasse, C. Rullière, and B. Couillaud. Methods for the generation of ultrashort laser pulses: Mode-locking. In C. Rullière, editor, *Femtosecond Laser Pulses: Principles and Experiments*, chapter 3, pages 53–81. Springer-Verlag, 1998.

[2] T. B. Norris. Femtosecond pulse amplification at 250 khz with a ti:sapphire regenerative amplifier and application to continuum generation. *Optics Lett.*, 17:1009, 1992.

[3] http://en.wikipedia.org/.

[4] R. L. Fork, O. E. Martinez, and J. P. Gordon. Negative dispersion using pairs of prisms. *Optics Lett.*, 9:150, 1984.

[5] www.lightsources.org.

[6] image taken from http://en.wikipedia.org/wiki/Diamond_cubic.

[7] from http://www.ioffe.ru/SVA/NSM/Semicond/.

[8] D. G. Cahill, W. K. Ford, K E. Goodson, G. D. Mahan, A. Majumdar, H. J. Maris, R. Merlin, and S. R. Phillpot. Nanoscale thermal transport. *J. Appl. Phys.*, 93:793, 2003.

[9] C. Colvard, R. Merlin, M. V. Klein, and A. C. Gossard. Observation of folded acoustic phonons in a semiconductor superlattice. *Phys. Rev. Lett.*, 45:298, 1980.

[10] S. M. Rytov. Acoustical properties of a thinly layered medium. *Sov. Phys. Acoust*, 2:68, 1956.

[11] B. Jusserand and M. Cardona. Raman spectroscopy of vibrations in superlattices. In M. Cardona and G. Güntherodt, editors, *Light Scattering in Solids V*, page 49. Springer, Berlin, 1989.

[12] C. Thomsen, H. T. Grahn, H. J. Maris, and J. Tauc. Surface generation and detection of phonons by picosecond light pulses. *Phys. Rev. B*, 34:4129, 1986.

[13] H. T. Grahn, H. J. Maris, J. Tauc, and B. Abeles. Time-resolved study of vibrations of si/ge multilayers. *Phys. Rev. B*, 38:6066, 1988.

[14] B. C. Daly, N. C. R. Holme, T. Buma, C. Branciard, and T. B. Norris. Imaging nanostructures with coherent phonon pulses. *Appl. Phys. Lett.*, 84:5180, 2004.

[15] J. Chen, J. B. Khurgin, and R. Merlin. Stimulated-emission-induced enhancement of the decay rate of longitudinal optical phonons in iiiv semiconductors. *Appl. Phys. Lett.*, 80:2901, 2002.

[16] O. Synnergren, T. N. Hansen, S. Canton, H. Enquist, P. Sondhauss, A. Srivastava, and J. Larsson. Coherent phonon control. *Appl. Phys. Lett.*, 90:171929, 2007.

[17] K. Mizoguchi, M. Hase, S. Nakashima, and M. Nakayama. Observation of coherent folded acoustic phonons propagating in a gaas/alas superlattice by two-color pump-probe spectroscopy. *Phys. Rev. B*, 60:8262, 1999.

[18] N. M. Stanton, R. N. Kini, A. J. Kent, M. Henini, and D. Lehmann. Terahertz phonon optics in gaasalas superlattice structures. *Phys. Rev. B*, 68:113302, 2003.

[19] D. A. Reis, M. F. DeCamp, P. H. Bucksbaum, R. Clarke, E. Dufresne, M. Hertlein, R. Merlin, R. Falcone, H. Kapteyn, M. M. Murnane, J. Larsson, Th. Missalla, and J. S. Wark. Probing impulsive strain propagation with x-ray pulses. *Phys. Rev. Lett.*, 86:3072, 2001.

[20] A. H. Chin, R. W. Schoenlein, T. E. Glover, P. Balling, W. P. Leemans, and C. V. Shank. Ultrafast structural dynamics in insb probed by time-resolved x-ray diffraction. *Phys. Rev. Lett.*, 83(2):336, Jul 1999.

[21] Christoph Rose-Petruck, Ralph Jimenez, Ting Guo, Andrea Cavalleri, Craig W. Siders, Ferenc Rksi, Jeff A. Squier Barry C. Walker, Kent R. Wilson, and Christopher P. J. Barty. Picosecond milliangstrom lattice dynamics measured by ultrafast x-ray diffraction. *Nature*, 398:310, 1999.

[22] A. M. Lindenberg, I. Kang, S. L. Johnson, T. Missalla, P. A. Heimann, Z. Chang, J. Larsson, P. H. Bucksbaum, H. C. Kapteyn, H. A. Padmore, R. W. Lee, J. S. Wark, and R. W. Falcone. Time-resolved x-ray diffraction from coherent phonons during a laser-induced phase transition. *Phys. Rev. Lett.*, 84(1):111–114, Jan 2000.

[23] H. Enquist, H. Navirian, T. N. Hansen, A. M. Lindenberg, P. Sondhauss, O. Synnergren, J. S. Wark, and J. Larsson. Large acoustic transients induced by nonthermal melting of insb. *Phys. Rev. Lett.*, 98:225502, 2007.

[24] Charles Kittel. *Introduction to Solid State Physics*. Wiley, 1995.

[25] M. P. Marder. *Condensed Matter Physics*. Wiley, 2000.

[26] L. D. Landau and E. M. Lifshitz. *Quantum Mechanics: Non-Relativistic Theory*, volume 3. Elsevier, 2007.

[27] R. Merlin. Generating coherent thz phonons with light pulses. *Solid State Commun.*, 102:207, 1997.

[28] A. Yariv and P. Yeh. *Optical Waves in Crystals*. Wiley, 1984.

[29] Nen-Wen Pu. Ultrafast excitation and detection of acoustic phonon modes in superlattices. *Phys. Rev. B*, 72:115428, 2005.

[30] D. H. Hurley and O. B. Wright. Detection of ultrafast phenomena by use of a modified sagnac interferometer. *Opt. Lett.*, 24:1305, 2002.

[31] C. Colvard, T. A. Gant, M. V. Klein, R. Merlin, R. Fischer, H. Morkoc, and A. C. Gossard. Folded acoustic and quantized optic phonons in (gaal)as superlattices. *Phys. Rev. Lett.*, 31:2080, 1985.

[32] M. Trigo, T. A. Eckhause, M. Reason, and R. S. Goldmanand R. Merlin. Observation of surface-avoiding waves: A new class of extended states in periodic media. *Phys. Rev. Lett.*, 97:124301, 2006.

[33] C. Rullière, T. Amand, and X. Marie. Spectroscopic methods for analysis of sample dynamics. In C. Rullière, editor, *Femtosecond Laser Pulses: Principles and Experiments*, chapter 8, pages 203–258. Springer-Verlag, 1998.

[34] D. Strickland and G. Mourou. Compression of amplified chirped optical pulses. *Opt. Commun.*, 56:219, 1985.

[35] G. Garrett. *Femtosecond Pulsed Laser Excitation of Coherent and Squeezed Phonon Fields in Perovskites and Semimetals*. PhD thesis, University of Michigan, 2001.

[36] M. K. Reed, M. K. Steiner-Shepard, and D. K. Negus. Widely tunable femtosecond optical parametric amplifier at 250 khz with a ti:sapphire regenerative amplifier. *Optics Lett.*, 19:1855, 1994.

[37] F. Salin. How to manipulate and change the characteristics of laser pulses. In C. Rullière, editor, *Femtosecond Laser Pulses: Principles and Experiments*, chapter 6, pages 159–176. Springer-Verlag, 1998.

[38] J. K. Wahlstrand. *Impulsive generation of coherent hybrid modes by light pulses*. PhD thesis, University of Michigan, 2005.

[39] D. A. Reis and A. M. Lindenberg. Ultrafast x-ray scattering in solids. In M. Cardona and R. merlin, editors, *Light Scattering in Solids IX*, chapter 8, pages 371–422. Springer-Verlag, 2007.

[40] K. Sokolowski-Tinten and D. von der Linde. Ultrafast phase transitions and lattice dynamics probed using laser-produced x-ray pulses. *J. Phys. Condens. Matter*, 16:R1517, 2004.

[41] A. Rousse, C. Rischel, and J. Gauthier. Femtosecond x-ray crystallography. *Rev. Mod. Phys.*, 73:1731, 2001.

[42] D. Attwood. *Soft X-Rays and Extreme Ultraviolet Radiation: Principles and Applications*. Cambridge University Press, 1999.

[43] Center for X-ray Optics and Advanced Light Source, X-ray Data Booklet. available online at http://xdb.lbl.gov/.

[44] A. Authier. *Dynamical Theory of X-Ray Diffraction*. Oxford, 2001.

[45] P. Basséras, S. M. Gracewski, G. W. Wicks, and R. J. D. Miller. Optical generation of high-frequency acoustic waves in gaas/alxga1xas periodic multilayer structures. *J. Appl. Phys.*, 75:2761, 1994.

[46] Gia-Wei Chern, Kung-Hsuan Lin, Yue-Kai Huang, and Chi-Kuang Sun. Spectral analysis of high-harmonic coherent acoustic phonons in piezoelectric semiconductor multiple quantum wells. *Phys. Rev. B*, 67:121303, 2003.

[47] A. Yamamoto, T. Mishina, Y. Masumoto, and M. Nakayama. Coherent oscillation of zone-folded phonon modes in gaas-alas superlattices. *Phys. Rev. Lett.*, 73:740, 1994.

[48] A. Bartels, T. Dekorsy, H. Kurz, and K. Köhler. Coherent control of acoustic phonons in semiconductor superlattices. *Appl. Phys. Lett.*, 72:2844, 1998.

[49] Ü. Özgür, C. Lee, and H. O. Everitt. Control of coherent acoustic phonons in semiconductor quantum wells. *Phys. Rev. Lett.*, 86:5604, 2001.

[50] O. Matsuda and O. B. Wright. Reflection and transmission of light in multilayers perturbed by picosecond strain pulse propagation. *J. Opt. Soc. Am. B*, 19:3028, 2002.

[51] B. E. Warren. *X-ray diffraction*. Dover, 1990.

[52] W. H. Zachariasen. *Theory of X-Ray Diffraction in Crystals*. John Wiley and Sons, Inc., 1945.

[53] B. W. Batterman and H. Cole. Dynamical diffraction of x rays by perfect crystals. *Rev. Mod. Phys.*, 36:681, 1964.

[54] S. Takagi. Dynamical theory of diffraction applicable to crystals with any kind of small distortion. *Acta Crystallogr.*, 15:1311, 1962.

[55] D. Taupin. Dynamic theory of x-ray diffraction in crystals. *Bull. Soc. Franc. Miner. Crystallogr.*, 87:469, 1964.

[56] B. Klar and F. Rustichelli. Dynamical neutron diffraction by ideally curved crystals. *Nuovo Cim.*, 13B:249, 1973.

[57] C. R. Wie, T. A. Tombrello, and T. Vreeland, Jr. Dynamical x-ray diffraction from nonuniform crystalline films: Application to x-ray rocking curve analysis. *J. Appl. Phys.*, 59:3743, 1986.

[58] M. Bargheer, N. Zhavoronkov, Y. Gritsai, J. C. Woo, D. S. Kim, M. Woerner, and T. Elsaesser. Coherent atomic motions in a nanostructure studied by femtosecond x-ray diffraction. *Science*, 306:1771, 2004.

[59] Y. M. Sheu, S. H. Lee, J. K. Wahlstrand, D. A. Arms, E. C. Landahl, D. A. Walko, M. Reason, R. S. Goldman, and D. A. Reis. Thermal transport in a semiconductor heterostructure measured by time-resolved x-ray diffraction.

[60] C. Herring. Role of low-energy phonons in thermal conduction. *Phys. Rev.*, 95:954, 1954.

[61] S.Adachi. *Physical Properties of III-V Semiconductor compounds.* Wiley, 1992.

[62] S. A. Teukolsky, W. T. Vetterling, and B. P. Flannery. *Numerical Recipes in C.* Cambridge University Press, 2002.

[63] B. W. Adams, M. F. DeCamp, E. M. Dufresne, and D. A. Reis. Picosecond laser-pump, x-ray probe spectroscopy of gaas. *Rev. Sci. Inst.*, 73:4150, 2002.